

---

# Characterization of DNA nanostructures with small-angle X-ray scattering

Caroline Hartl

---



München 2018



---

# Characterization of DNA nanostructures with small-angle X-ray scattering

Caroline Hartl

---

Dissertation  
an der Fakultät für Physik  
der Ludwig-Maximilians-Universität  
München

vorgelegt von  
Caroline Hartl  
aus München

München, den 16.10.2018

Erstgutachter: Prof. Dr. Tim Liedl

Zweitgutachter: PD Dr. Bert Nickel

Tag der mündlichen Prüfung: 29.11.2018

# Contents

<b>1</b>	<b>Introduction to DNA nanotechnology</b>	<b>1</b>
1.1	The nanoscale . . . . .	1
1.2	Desoxyribonucleic acid . . . . .	2
1.2.1	Structure of DNA . . . . .	3
1.2.2	Base pairing and base stacking . . . . .	4
1.2.3	Properties of DNA . . . . .	6
1.3	Introduction to structural DNA nanotechnology . . . . .	9
1.3.1	DNA as a building block . . . . .	9
1.3.2	DNA nanostructures to arrange guest particles . . . . .	11
1.3.3	DNA origami . . . . .	13
<b>2</b>	<b>Materials and methods in DNA nanotechnology</b>	<b>15</b>
2.1	Gel electrophoresis . . . . .	15
2.2	Transmission electron microscopy . . . . .	16
2.3	Atomic force microscopy . . . . .	18
2.4	Small-angle X-ray scattering (SAXS) . . . . .	19
2.4.1	Basics of SAXS . . . . .	20
2.4.2	SAXS scattering profiles of basic geometries . . . . .	21
2.4.3	SAXS setup . . . . .	27
2.4.4	Sample considerations . . . . .	29
2.4.5	SAXS data interpretation . . . . .	31
<b>3</b>	<b>SAXS for characterization of DNA origami structures</b>	<b>33</b>
3.1	The shape of DNA origami . . . . .	34
3.2	SAXS for characterization of DNA origami structures . . . . .	35
3.2.1	Shape and inner structure of DNA origami . . . . .	36

---

3.2.2	Structure of DNA origami in different salt concentrations. . . . .	39
3.2.3	Annealing and melting of DNA origami structures. . . . .	40
3.2.4	Conclusion . . . . .	43
<b>4</b>	<b>SAXS on DNA mediated gold nanoparticle (AuNP) assemblies</b>	<b>45</b>
4.1	Applications of DNA origami templated AuNP architectures . . . . .	46
4.2	Distance measurements on AuNP arrangements with SAXS . . . . .	46
4.3	Attachment of AuNPs to DNA origami nanostructures . . . . .	47
4.4	Pair density distribution function of AuNP assemblies . . . . .	48
4.5	SAXS on DNA origami mediated AuNP assemblies . . . . .	49
4.5.1	SAXS pattern and design scheme . . . . .	50
4.5.2	Direct modeling and PDDF . . . . .	52
4.5.3	Influence of attachment sites and connector types . . . . .	53
4.5.4	Helical nanoparticle arrangement . . . . .	56
4.5.5	DNA origami assemblies mediating small AuNPs . . . . .	57
4.5.6	Conclusion . . . . .	59
<b>5</b>	<b>Three dimensional crystalline DNA origami lattices</b>	<b>61</b>
5.1	Programmable materials . . . . .	61
5.2	Three dimensional crystalline DNA origami lattices . . . . .	64
5.2.1	Triangular DNA origami building block . . . . .	66
5.2.2	Lattice assembly . . . . .	67
5.2.3	DNA origami lattices hosting guest particles . . . . .	69
5.2.4	Small angle X-ray scattering pattern of DNA origami lattices . . . . .	70
5.2.5	Melting of lattices at high temperatures . . . . .	72
5.2.6	Polymerization process of DNA origami building blocks . . . . .	74
5.2.7	Building blocks with multiple guest particles . . . . .	76
5.2.8	Conclusion . . . . .	77
<b>A</b>	<b>Appendix</b>	<b>79</b>
<b>B</b>	<b>Appendix</b>	<b>93</b>
<b>C</b>	<b>Appendix</b>	<b>109</b>
	<b>Acknowledgements</b>	<b>132</b>

# List of Figures

1.1	Made with atoms . . . . .	2
1.2	Desoxyribonucleic acid . . . . .	5
1.3	Sticky ends . . . . .	10
1.4	DNA nano cube . . . . .	11
1.5	DNA origami . . . . .	12
1.6	3D DNA origami . . . . .	13
2.1	TEM images . . . . .	17
2.2	Atomic force microscope scheme . . . . .	18
2.3	"Photo 51" . . . . .	19
2.4	Scattering vector . . . . .	21
2.5	SAXS intensities of spheres of different sizes . . . . .	22
2.6	SAXS intensities for different polydispersities . . . . .	23
2.7	SAXS intensities of dimers . . . . .	25
2.8	SAXS setup . . . . .	28
2.9	Synchrotron . . . . .	30
3.1	Representations of a DNA origami structure . . . . .	34
3.2	Calculated scattering intensities of basic shapes . . . . .	35
3.3	SAXS intensities of three different DNA origami structures . . . . .	37
3.4	SAXS of 24-helix bundle origami exposed to buffers of low MgCl <sub>2</sub> concentration	39
3.5	SAXS intensities of the 24-helix bundle origami exposed to increasing tem- peratures . . . . .	41
3.6	SAXS intensities of a 24-helix bundle DNA origami during its assembly in situ . . . . .	42
4.1	Attachment of gold nanoparticles to DNA origami . . . . .	48

4.2	Pair density distribution functions of spheres and dimers . . . . .	49
4.3	Schemes and SAXS pattern of AuNP assemblies and its components . . . . .	51
4.4	Sketch of the trimeric AuNP arrangement on a DNA origami block . . . . .	52
4.5	PDDF of DNA origami block with AuNPs at different attachment sites . . . . .	54
4.6	PDDF of DNA origami block with AuNPs attached with different connector types . . . . .	55
4.7	PDDF of a helical arrangement of AuNPs . . . . .	57
4.8	Scheme and PDDF of dimer of small AuNPs . . . . .	58
5.1	Three dimensional lattices based on DNA and AuNPs as building blocks . . . . .	62
5.2	DNA based lattices . . . . .	63
5.3	Three dimensional DNA crystal and DNA origami lattice . . . . .	65
5.4	Workflow of crystal assembly . . . . .	66
5.5	Three dimensional DNA origami crystals . . . . .	68
5.6	Three dimensional gold nanoparticle DNA origami crystals . . . . .	69
5.7	SAXS pattern of 3D DNA origami lattices . . . . .	71
5.8	DNA origami lattices exposed to increasing temperatures . . . . .	73
5.9	Monitoring of the polymerization of DNA origami building blocks . . . . .	75
5.10	Building block units with multiple guest particles . . . . .	76
A.1	DNA origami folding process intermediates . . . . .	81
A.2	Temperature dependent scattering intensity of DNA origami block and cylinder . . . . .	82
A.3	Crysol simulation based on caDNAno files . . . . .	85
A.4	Lattice constant and radius of the cylindric DNA origami structure . . . . .	88
A.5	caDNAno design of the 24-helix bundle structure . . . . .	89
A.6	caDNAno design of the brick structure . . . . .	90
A.7	caDNAno design of the one-layer-sheet . . . . .	91
B.1	Agarose gel for purification of the DNA mediated AuNP assemblies . . . . .	95
B.2	PDDF of a dimer of spheres . . . . .	100
B.3	Attachment sites of the block . . . . .	103
B.4	Attachment sites of the helix . . . . .	104
B.5	caDNAno design of the gold nanoparticle block . . . . .	105

# List of Tables

4.1	Determined center-to-center distance of AuNP dimers . . . . .	53
A.1	CanDo parameter . . . . .	84
A.2	Fit parameter of geometric model . . . . .	85
A.3	Fit parameter of geometric model and Lorentzian peak for 24HB . . . . .	86
A.4	Fit parameter of two Debye model for 24HB at low $MgCl_2$ concentration .	86
A.5	Parameter of small rigid cylinder model for 24HB . . . . .	86
A.6	Fit parameter of geometric model and Lorentzian peak for brick and sheet	87
A.7	Parameter of small rigid cylinder model for brick and sheet . . . . .	87
A.8	Designed origami dimensions in number of basepairs . . . . .	88
A.9	Designed origami dimensions . . . . .	88
A.10	Inter-helical distance from peak fit . . . . .	88
B.1	Fit parameters of core-shell-model of thiol-DNA functionalized AuNPs . .	101
B.2	Connector length in AuNP dimers . . . . .	101



# Zusammenfassung

Desoxyribonukleinsäure (DNA), die Trägerin der Erbinformation, kann auf Grund ihrer Programmierbarkeit verwendet werden, um Strukturen auf der Nanoskala zu erschaffen. Im vielseitigen Gebiet der DNA-Nanotechnologie hat sich die DNA-Origami-Methode bewährt: Ein circa 8 Kilobasen langer, zirkulärer DNA-Strang - der "scaffold" - wird mit Hilfe von kurzen DNA-Oligonukleotiden - den "staples" - in eine gewünschte dreidimensionale Form, bestehend aus miteinander verbundenen parallelen DNA-Doppelhelizes, gefaltet. Diese Arbeit beschreibt die Herstellung von verschiedenen, DNA-Origami basierten Nanostrukturen und ihre Charakterisierung in Lösung unter Verwendung der Röntgenkleinwinkelstreuungstechnik (SAXS). SAXS wurde verwendet, um die Geometrie, die räumliche Ausdehnung, den interhelikalen Abstand, die Deformation und die Stabilität von unterschiedlichen DNA-Origami-Nanostrukturen mit verschiedenen Formen und Gitterquerschnitten zu bestimmen. Der Zerfall der Nanostrukturen bei niedrigen Salzkonzentrationen und hohen Temperaturen wurde untersucht. Die Messungen zeigten eine Vergrößerung des Querschnitts und des interhelikalen Abstands um bis zu 10 % bei niedrigen Salzkonzentrationen. Ein abruptes Schmelzen bei Temperaturen über 50 °C wurde beobachtet. Des Weiteren wurde gezeigt, dass der Zusammenbauprozess der DNA-Origami-Strukturen mit SAXS beobachtet werden kann. Es wurde evaluiert, wie SAXS verwendet werden kann, um die Abstände zwischen Gold-Nanopartikeln, die an DNA-Origami Strukturen angebracht sind, zu bestimmen. Der Einfluss der Position der Bindestellen an den DNA-Origami-Strukturen und der Konnektortypen, die zur Anbindung verwendet werden, wurde bestimmt. Komplexe Anordnungen mit mehreren Gold-Nanopartikeln an DNA-Origami-Strukturen wurden untersucht. Außerdem wurde der Zusammenbau von dreidimensionalen DNA-Origami-Gittern, die Nanopartikel mit bis zu 20 nm Durchmesser beherbergen können, bewerkstelligt. Darüber hinaus wurden Abmessungen und Stabilität der Gitter mit SAXS bestimmt. Diese Ergebnisse zeigen, wie die SAXS-Technik als Kontroll- und Optimierungswerkzeug für DNA-Origami-Strukturen dienen kann.



# Abstract

Deoxyribonucleic acid (DNA), the carrier of genetic information, can be used to create structures on the nanoscale due to its programmability. In the versatile area of DNA nanotechnology, the method of DNA origami has proven its usefulness: A circular strand of DNA with a size of about 8 kilobases - the "scaffold" - is folded via short DNA oligonucleotides - the "staples" - into a desired three dimensional shape in the form of interconnected parallel DNA double helices. This work describes the assembly of various DNA origami based nanostructures and their characterization in solution conditions using the technique of small-angle X-ray scattering (SAXS). The SAXS technique was applied to verify the geometry and to determine the spatial dimensions, the interhelical spacing, the deformation and the stability of various DNA origami nanostructures of different shapes and lattice cross sections. The disassembly of the nanostructures was monitored upon exposure to low salt concentrations and increased temperatures. The measurements revealed an increase of cross section and interhelical distance of up to 10 % in low salt concentrations. An abrupt melting of the DNA nanostructures at temperatures of above 50 °C was found. Additionally, it was shown that the assembly process of the DNA origami structures can be observed with SAXS. Furthermore, it was investigated how SAXS can be used to determine the distances between gold nanoparticles (AuNP) attached to structures. The influence of two factors on the AuNP distances was investigated: the position of the binding sites on the DNA origami structures and the type of connector that attaches the AuNPs to the DNA origami structures. Complex arrangements of multiple AuNPs on DNA origami structures were examined using SAXS. Moreover, the assembly of three dimensional DNA origami lattices that can host guest nanoparticles of diameters of up to 20 nm was achieved. Furthermore, their dimension and stability was determined using SAXS. These findings show how the SAXS technique can serve as a tool to control and optimize DNA origami nanostructures.



# Chapter 1

## Introduction to DNA nanotechnology

### 1.1 The nanoscale

The nanoscale - from the Greek word "nanos" meaning "dwarf" - includes the molecular and supramolecular level and houses objects such as proteins and viruses. As the subject is defined by the size of at least one dimension of the objects in the nanometer range it is an interdisciplinary field concerning researchers from disciplines such as biology, chemistry, physics, material science and engineering [1]. The goal of nanotechnology is to develop new materials, find size induced functionalities and take control of the nanoworld.

Some effects based on nano objects have been used in history without consciousness about the role of the nanoscale: optical effects based on gold and silver nanoparticles are the basis of colorful glasswindows in churches and the famous Lycurgus cup that looks red in transmitted light and green in reflected light [2, 3]. Carbon nanotubes and cementite nanowires were found in Damascus sabre steel that was said to have extraordinary mechanical properties [4]. Norio Taniguchi - who coined the term "Nanotechnology" -, Eric Drexler and Richard Feynman have dreamed about creating tiny machines and manipulating the world on the level of single atoms [5, 6, 7]. With the development of scanning tunneling microscope in 1981 it became possible to see individual atoms [8, 9] and control them. The creation of the IBM logo out of atoms with a scanning tunneling microscope is an astonishing example of extreme control over the atomic world [10], see Figure 1.1. Binnig and Rohrer received the Nobel Prize in Physics in 1986 for "*their design of the scanning tunneling microscope*" [11] together with Ernst Ruska. The fascination that comes with the control at the small scale can be grasped in a nice way by watching the movie: "*A boy and his atom*" by IBM that holds the Guinness World Record for the World's smallest

stop motion film. ” *To explore the limits of filmmaking [they] created the world’s smallest movie. It was made by moving actual atoms, frame by frame.*” [12]. Examples of art on the nanoscale that rise a sense of awe can be found in ref. [13].

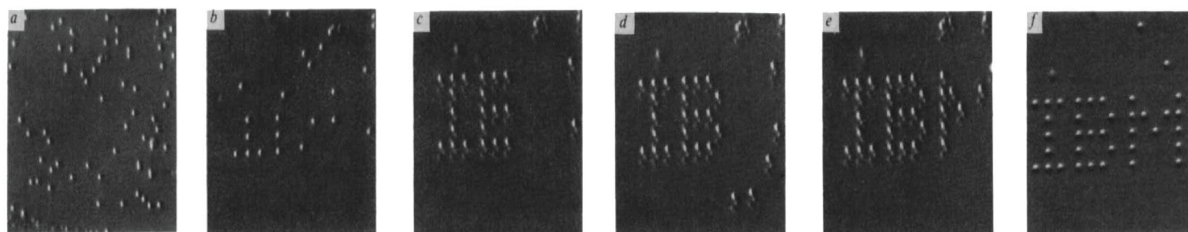


Figure 1.1: Creation of the IBM logo out of xenon atoms with a letter size of 50 Å. Reprinted by permission from Springer Nature Customer Service Centre GmbH: Springer Nature, Nature, from ref. [10], copyright (1990).

With the aim to fabricate functional material at the nanoscale, two main approaches are followed: Top down approaches and bottom up approaches. In top down approaches shaping of nanoscale objects is performed by removing matter from a bulk material or by rearrangement of matter such as with the creation of the IBM logo shown before.

An alternative approach is to create things from the bottom up. Structure on the nanoscale can be created by relying on self-assembly. Here the key role is programmability. This property can be found in the coding nature of DNA [14]. With the rise of awareness of DNA as carrier of genetic information synthetization and sequencing techniques became widely available. This established DNA as an ideal building block on the basis of its availability, addressability and natural structure.

## 1.2 Desoxyribonucleic acid

The DNA molecule builds the basis of life. As carrier of genetic information it provides robust information storage and is self-replicating. It is comprised of two robust polymer strands winding around each other in a helical manner and held together by complementary bases. Both strands contain the same information. This structure of two base-complementary strands is the basis for its replication mechanism and therefore for the reproduction mechanism of all living organisms. Here I give a short introduction to its history, structure and properties [15, 16].

In the year 1869 Friedrich Miescher extracted a substance from the cell nucleus of Leukocytes. He gave the substance the name "*nuclein*" and already guessed its importance for heredity [17]. Avery [18] and Hershey Case [19] first demonstrated that DNA is the carrier of genetic information. Based on the X-ray diffraction data from Gosling, Franklin and Wilkins [20, 21] and the biochemical evidence for nucleotide base pairing rules formulated by Chargaff [22], Watson and Crick proposed the first correct double helix model of DNA in 1953 [23]. Watson, Crick and Wilkins were awarded the Nobel Prize in Physiology or Medicine in 1962 "*for their discoveries concerning the molecular structure of nucleic acids and its significance for information transfer in living material*" [24]. The structure suggested the replication mechanism of hereditary material of unwinding and synthesis of a complementary strand for each of the single strands. This semiconservative replication mechanism was verified by Meselson Stahl 1957 [25]. Nowadays a plethora of methods are available for gene sequencing and synthesis and for the synthesis of oligonucleotides with functional molecules attached. The rapid development of DNA nanotechnology begun with the pioneering work of Nadrian Seeman in 1982 [14].

### 1.2.1 Structure of DNA

The structure and properties of DNA and its implications for the use of DNA as a building block will now be depicted: DNA is a polymer with up to 100 millions of units. Its monomer unit the nucleotide consists of one out of four nitrogen containing nucleobases - guanine (G), adenine (A), thymine (T) or cytosine (C) - connected to the 1'-carbon atom of a 2-deoxyribose sugar which is connected to a phosphate group at its 5'-carbon atom. Chains of nucleotides are formed by connection of the phosphate group of the 5'-carbon to the 3'-carbon of the pentose sugar of the adjacent nucleotide by formation of a covalent phosphodiester bond. This yields a robust backbone of alternating phosphate and sugar residues carrying the nucleobases. The robust nature of the phosphate sugar backbone is key to its function as carrier of genetic information encoded in the sequence of the four nucleobases. Due to the asymmetry, the polynucleotide has a directionality: A DNA single strand has a so called 5'-end usually with a terminal phosphate group and a 3'-end with a terminal hydroxyl group. Enzymes usually process DNA from the 5'- to the 3'-end. In the double helix structure the two strands are antiparallel to each other to allow pairing of their bases. Due to the asymmetry of the glycosidic bonds between sugar and base the two strands winding around each other possess a so called major and a minor groove. The minor groove appears at the side of the base with the glycosidic bonds. The large major

groove which makes the bases accessible for proteins is formed at the other side.

Different double helical forms of DNA can be found in physiological conditions. The most common double helical form is B-DNA (Figure 1.2): B-form DNA is right-handed. The spacing between its nucleotides is 0.34 nm. The double helix has a diameter of 2 nm and the helical pitch is 10.5 base pairs. The bases are almost perpendicular to the DNA axis. In addition to this most common form there are other forms of double helical DNA of slightly different appearance and dimensions regarding e.g. handedness, length of the helix turn and diameter, number of bases per turn and size of the major and minor groove. A-form DNA is observed in dehydration conditions. It is right-handed too, but shorter with a slightly larger diameter. A-form helices are also found in RNA and DNA-RNA hybrid complexes [26]. At certain environmental conditions and sequences (with alternating purines and pyrimidines), left-handed Z-DNA can form. It is longer than B-form DNA and has a slightly lower diameter. It is characterized by a zigzagging backbone. By changing the environmental conditions a transition between B- and Z-DNA can be induced for certain sequences [27, 28]. This can be used to build switchable nanostructures sensitive to environmental changes [29].

### 1.2.2 Base pairing and base stacking

The nucleobases of the two strands comprising the double helix prefer under regular conditions a specific pairing - the Watson-Crick base pairing or canonical base pairing. Here adenin binds to thymine and guanine binds to cytosine. The G-C connection occurs via three and the A-T connection via two hydrogen bonds, see Figure 1.2. Adenine and guanine are purin based with a six membered ring fused to a five membered ring and thymine and cytosine are pyrimidin based with a six membered ring. A base pair with Watson-Crick base pairing is always formed by one purin base and one pyrimidine base and therefore the different basepairs have essentially the same dimension. With the same distance between the 1'-carbon atoms of sugars on opposite strands, a helical structure that is independent of the sequence can arise. Following the base paring rules, a DNA strand can hybridize to another strand with a reverse complementary sequence in an antiparallel manner to form a double helix with the bases pointing to the inside of the helix complementing each other. The specificity due to the base pairing rules makes each part of a DNA single strand easily addressable via its complementary sequence.

While in chlorophorm - a non-aqueous solvent - single bases form hydrogen bond based base pairs, in an aqueous environment where hydrogen bonds with water molecules are

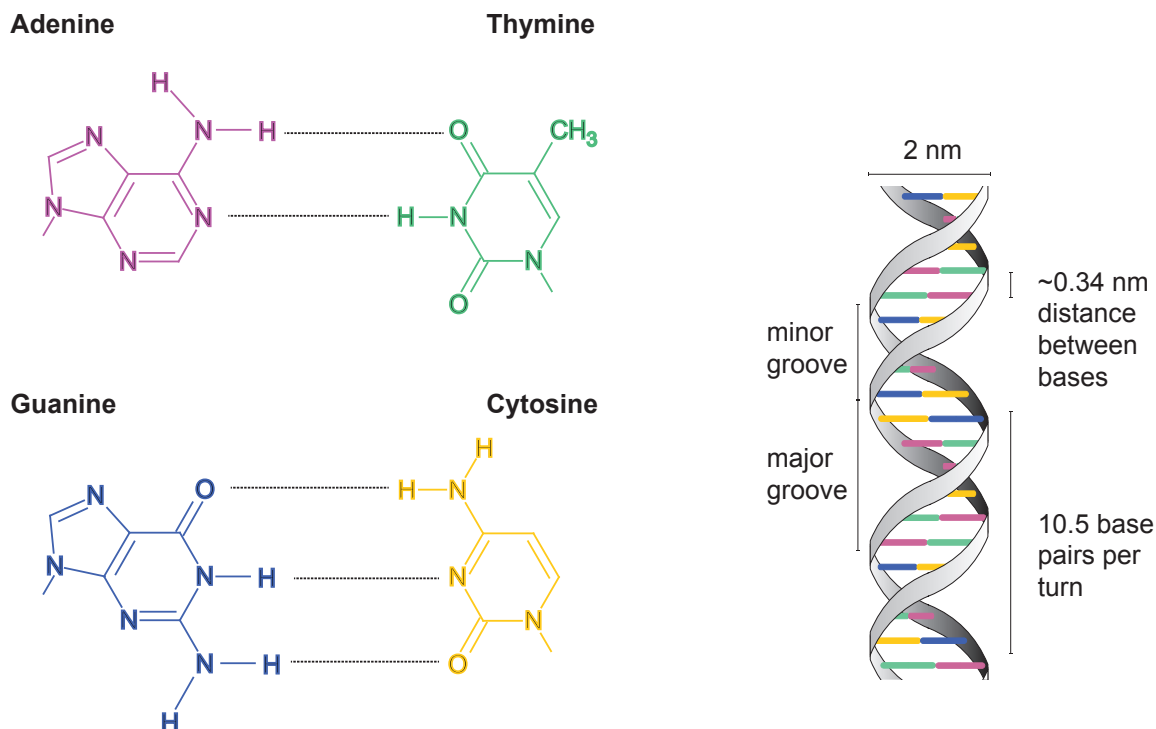


Figure 1.2: Watson-Crick base pairing of adenine with thymine and cytosine with guanine with two and three hydrogen bonds (dotted lines), respectively b) The double helical structure of B-form DNA shows a major and minor groove and has a diameter of 2 nm. Here white ribbons represent the phosphate-sugar-backbone and the colored rods indicate the base pairs.

formed, the planar bases pile on top of each other due to attractive interactions caused by the overlap of the delocalized pi electron systems of the neighbouring aromatic rings in the pyrimidin and purin based nucleobases. These interactions are called base stacking. The stacking interaction energies of two adjacent base pairs depend on the type of base pairs, on salt concentration and on temperature.

Both base stacking and base pairing are important for the formation of the double helical structure. Stacking is the main factor for stability of the double stranded DNA molecule [30]. In a long DNA molecule the two strands are held together more strongly than in short ones.

### 1.2.3 Properties of DNA

#### Polyelectrolyte properties

DNA is a strong polyelectrolyte. The phosphate groups in the DNA backbone become deprotonated at pH values above 1. Therefore, the phosphodiester backbone in a polynucleotide in an aqueous environment in physiological conditions is highly charged.

The important concept of screening of interaction between charges in the presence of counter ions and coions was described by Debye and Hückel. In the presence of ions the negative charges on the backbone of DNA lead to the formation of a so called ion atmosphere around the DNA. The charges on the backbone attract ions of the opposite charge and repel ions of the same charge which leads to an accumulation of counterions and a depletion of coions. The formation of the ion atmosphere leads to a screening of the highly charged backbone i.e. to a reduction of long range electrostatic interactions. Screening effects can be described by the Debye length in an electrolyte solution. The Debye-length is the characteristic length scale on which the electric potential of a local excess charge decays to  $1/e$ . In an electrolyte it is given by

$$\lambda_D = \sqrt{\frac{\epsilon_r \epsilon_0 k_B T}{2 N_A e^2 I}} \quad (1.1)$$

with the permittivity  $\epsilon_r$  the Avogadro constant  $N_A$ , the ionic strength of the electrolyte  $I$ . A detailed review about the interactions of nucleic acids and ions is given by ref. [31]. This screening allows the two highly charged single stranded DNA molecules to come together for double strand formation. Addition of  $Mg^{2+}$  is commonly used to induce folding of nucleic acids. For folding of nanostructures from DNA, ion concentrations have to be adjusted to allow screening for the DNA strands to come close together but at the same time to not lead to aggregation [32].

#### Optical properties of DNA

With the knowledge of the optical properties of DNA its concentration can be determined and the hybridization and denaturation processes of the DNA strands can be monitored spectroscopically.

The intensity decrease of light passing through an absorbing solution is described by the Beer-Lambert law  $I = I_0 \cdot 10^{-\epsilon c l}$  where  $I_0$  is the intensity of the incoming light and  $I$  is the intensity of the transmitted light,  $l$  is the path length,  $c$  is the concentration and

$\epsilon$  is the extinction coefficient. The absorbance  $A = \log(I_0/I) = \epsilon lc$  is also called optical density (OD). Absorbance measurements are used to determine DNA concentration. For the determination of the absorbance of a specific polynucleotide the absorbance of its nucleotides as well as the interactions among them have to be taken into account. The bases of DNA in their native state absorb light at a wavelength of around 260 nm. The wavelength of maximum absorption remains the same for polynucleotide strands and double stranded DNA, but a double stranded DNA molecule absorbs less than the sum of its single strands and a single strand absorbs less than the sum of its bases. This effect is called hypochromicity and can be used to measure dissociation and hybridization processes of nucleic acids.

Furthermore, circular dichroism measurements - i.e. measurements of the difference of absorption of lefthanded and righthanded circularly polarized light - can determine the chirality of the nucleic acid and therefore distinguish B- and Z-DNA.

### Thermal stability of DNA

For the role of DNA as carrier of genetic information and its replication it is of particular importance that the backbone is strong, held together by covalent bonds as it carries in its base sequence the genetic information and that the connection of one DNA strand to its complementary DNA strand by hydrogen bonds is weaker so DNA can be unzipped for its multiplication. With increasing temperature the DNA double strand (dsDNA) first denaturates into two single DNA strands (ssDNA). Due to the effect of hyperchromicity this effect can be monitored by absorption measurements. The midpoint of the s-shaped melting curve is the melting temperature i.e. the temperature at which 50 % of DNA is present in the solution in a denaturated state. The melting point is a measure for the DNA duplex stability.

A first estimate of the melting temperature  $T_m$  of a sequence is given via its GC content [33]. Considering nearest neighbour interactions the melting temperature  $T_m$  in  $^{\circ}C$  for nonself-complementary oligonucleotide duplex of known sequence can be estimated via [34, 35, 36, 37, 38]

$$T_m = \frac{\Delta H}{A + \Delta S + R \cdot \ln(\frac{C}{4})} - 273.15 + 16.6 \log[Na^+] \quad (1.2)$$

with enthalpy change  $\Delta H$  in kcal/mol, entropy change  $\Delta S$  in kcal K<sup>-1</sup> · mol<sup>-1</sup>,  $A = -0.0108$  kcal K<sup>-1</sup> · mol<sup>-1</sup> accounting for helix initiation, gas constant  $R = 0.00199$  kcal K<sup>-1</sup> · mol<sup>-1</sup>,

total oligonucleotide strand concentration in mol/liter, sodium ion concentration  $[Na^+]$  in mol/liter, using tabulated nearest-neighbour values for  $\Delta H$  and  $\Delta S$  assuming a two-state transition. As screening effects play an important role, ion concentration influences the melting temperature. Furthermore, the melting point depends on DNA concentration, length and sequence.

Single DNA strands survive high temperatures since the backbone is held together by covalent bonds. The described melting behavior has implications for the annealing process used for the assembly of nanostructures from DNA and for their stability.

### Mechanical properties

To describe size, shape and properties of polynucleotides in solution DNA can be depicted using different structural models from polymer theory. A short description is given here following ref. [39, 15, 40]. A distinction is made between models for ideal chains and real chains. An ideal chain model does not consider interactions of monomers that are far apart along the chain as opposed to real chains that interact with the solvent and interact with themselves. Here I depict two models of ideal chains that are used to describe single stranded DNA and double stranded DNA, respectively, considering its differing rigidity.

At high ion concentrations DNA charges are fully screened. The simplest model for polymers - the freely jointed chain (FJC) - can be used to approximate fully screened single stranded DNA. In the FJC it is assumed that there are no interactions of the monomers. The segments of the polymer are modeled as rigid rods with a fixed length  $l$ . They are freely jointed so that a random walk can be assumed. This means the monomers can occupy the same space and their orientation is completely independent of the neighboring monomers. The mean square end-to-end distance of a polymer of  $N$  segments of length  $l$  in the FJC model calculates as  $\langle R^2 \rangle = Nl^2$ . It is proportional to the number of segments  $N$ .

To depict the properties of the stiffer double stranded DNA the wormlike chain (WLC) model for semi-flexible polymers is used. As in the FJC model an ideal chain is assumed. The WLC is a special case of the freely rotating chain model (FRC) at very small values of the bond angle. In the FRC the bond lengths and bond angles  $\theta$  are constant and the torsion angles are independent of each other and equally likely. The maximal extension of the chain - the contour length  $R_{max}$  - is given by  $R_{max} = Nl \cos(\frac{\theta}{2})$ . For a stiff polymer like dsDNA the bond angle is small and  $R_{max} \approx Nl$ . The mean square end to end distance is  $\langle R^2 \rangle = 2 \cdot l_p R_{max} - 2l_p^2(1 - \exp(-\frac{R_{max}}{l_p}))$  with the persistence length  $l_p$ . The persis-

tence length is given via the exponential decay of the tangent vector correlation function  $\langle t(0) \cdot t(L) \rangle = e^{-\frac{R_{max}}{l_p}}$  with the tangent to the polymer at position 0 and the tangent at a distance  $L$  away from this position along the contour of the chain.  $l_p$  is proportional to the bending stiffness of the chain.

For a chain much longer than the persistence length  $R_{max} \gg l_p$  the behavior of the mean square end to end distance approximates the freely jointed chain  $\langle R^2 \rangle = 2 \cdot l_p R_{max}$ . The so called Kuhn length that describes the effective bond-length of an equivalent freely jointed chain of the same contour length  $R_{max}$  in the (WLC) model is  $l_K = 2 \cdot l_p$ . A chain that is much shorter than the persistence length  $R_{max} \ll l_p$  can be considered fully extended  $\langle R^2 \rangle = R_{max}^2$  adopting its contour length. The persistence length of DNA in 0.1 M NaCl is about 50 nm or 150 bp [15].

Short pieces of ds DNA such as  $\sim 10$ -20 bp - for linker lengths of the assemblies investigated here and double helix segments of typically 21 bp between connections - are considered to be stiff and straight. Rigid nanostructures can be built by joining DNA double strands with connections placed at distances that are much lower than the persistence length of DNA.

For the design, assembly, purification and characterization of nanostructures the base pairing principle, the geometry of DNA of double helical antiparallel strands, its stiffness, its base pairing and stacking interaction, its stability dependence on salt and temperature and its polyelectrolyte properties and optical properties are exploited.

## 1.3 Introduction to structural DNA nanotechnology

### 1.3.1 DNA as a building block

In 1982 the father of DNA nanotechnology, Ned Seeman, realized that "*[...] biology is no longer the only branch of science where DNA is finding a significant role: It is now possible to exploit DNA complementarity to control the structure of matter*" [41]. He brought DNA into the "*material world*" [42]. In the following a short introduction to DNA nanotechnology is given [42]. The properties of the DNA molecule - size, stiffness, geometry, base pairing and the available infrastructure - make it an ideal building block on the nanoscale. Connections of DNA based molecules can be achieved via hybridization of so called "sticky ends" (Figure 1.3). Sticky ends are single stranded DNA overhangs from a DNA double strand. They are designed to allow for hybridization of the sticky end of one DNA building block to its Watson-Crick complementary sequence sticky end of another building block.

Sticky ends provide a selective connection of the building blocks with an overhang of  $N$  bases allowing for  $4^N$  possibilities for the sequence. In addition to the advantage of high specificity, the geometry of such a connection is the well predictable double helix.

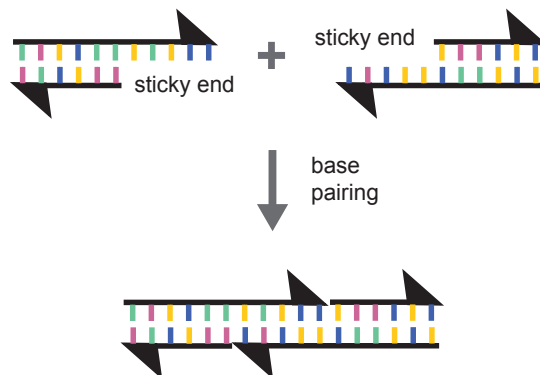


Figure 1.3: Sticky ends. Complementary overhangs of single DNA strands from double helices can hybridize and "stick" two pieces together. The connectivity is specific due to the Watson-Crick base pairing rules.

The extension of an assembly from one dimension to two or three dimensions requires branched structures of DNA. One branched DNA structure occurring in nature is the Holliday junction. It occurs during meiosis where two homologous chromosomes exchange strands and therefore genetic information, allowing for genetic diversity. The Holliday junction is a four armed junction of DNA double helices consisting of four DNA single strands. Due to sequence symmetry however branch migration is allowed in these Holliday junctions. For the use as a building block an asymmetry of the sequences is introduced and with this a stable building block is formed, that now allows a programmed self-assembly in two dimensions.

To achieve a two and three dimensional assembly of lattices however sufficient rigidity of the building blocks is required. For the assembly of two dimensional lattices double crossover tiles (DX) that are two connected antiparallel dsDNA strands were used as motives which are essentially more rigid than a dsDNA strand [43, 44]. Adding of protrusions to specific DNA tiles allowed a patterning of two dimensional DNA assemblies that can be visualized with an AFM [32, 44]. The use of a tensegrity triangle [45] allowed the assembly of 3D crystals to a macroscopic size [46] (Figure 5.3).

The first confined DNA nanostructure was built by Ned Seeman in 1991 [47]: a DNA

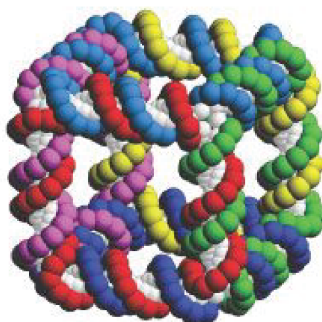


Figure 1.4: A DNA cube with double helical edges was built by Ned Seeman in 1991 [47]. Reprinted by permission from Springer Nature Customer Service Centre GmbH: Springer Nature, Nature, from ref. [42], copyright (2003).

cube with double stranded DNA as edges that consists of six single DNA strands, see Figure 1.4.

The concepts were extended from simply building objects and lattices to DNA nano "machines" that impart functionalities. The first nano mechanical machine was a rotating device based on the B-Z transition of DNA responding to the addition of a small molecule [29]. The toehold technique introduces a programmable and specific control mechanism[48]: A single DNA strand with a base complementary and a non-complementary part is incorporated into a DNA structure. By addition of a fully complementary sequence the partially complementary sequence is stripped of the device. In a DNA construct in the form of a pair of tweezers addition of the specific DNA strands induced opening and closing. Dynamic DNA assemblies have been built that rely on stacking interactions of shape complementary components [49]. Salt concentration and temperature induce opening and closing of the constructs. Other examples include a walker constructed from DNA [50] and a nanoscale robotic arm controlled by electric fields that could be used to transport fluorophores and inorganic nanoparticles [51].

### 1.3.2 DNA nanostructures to arrange guest particles

Attachment of functional nano objects open new possibilities for applications of DNA structures. Any molecule that can be attached to a DNA strand can in principle be arranged on DNA nanostructures. Examples are fluorophores, proteins, gold- or silver-nanoparticles and nano diamonds [52, 53, 54, 55, 56, 57]. DNA constructs allow a positioning of guest molecules on the basis of the DNA's geometry and dimensions - a distance between bases of

about 0.34 nm and a diameter of about 2 nm. DNA nanostructures are extremely versatile. They offer the possibility for placement of different species of guest objects, for example gold nanoparticles and fluorophores, simultaneously. Furthermore, DNA nanostructures can be designed to be reconfigurable, e.g. by strand displacement. Therefore they can also be used for structurally reconfigurable guest particle systems. A plethora of nano devices have been made by the precise arrangement of guest particles of different types on DNA nanostructures. As an example precisely arranged fluorophores to serve as molecular rulers [52] and for potential light harvesting applications [58] have been investigated. Synthetic lipid membrane channels have been constructed in form of a DNA nanopore with cholesterol moieties [59] and many constructs involving gold nanoparticles [60], which will be described in more detail in chapter 4.3.

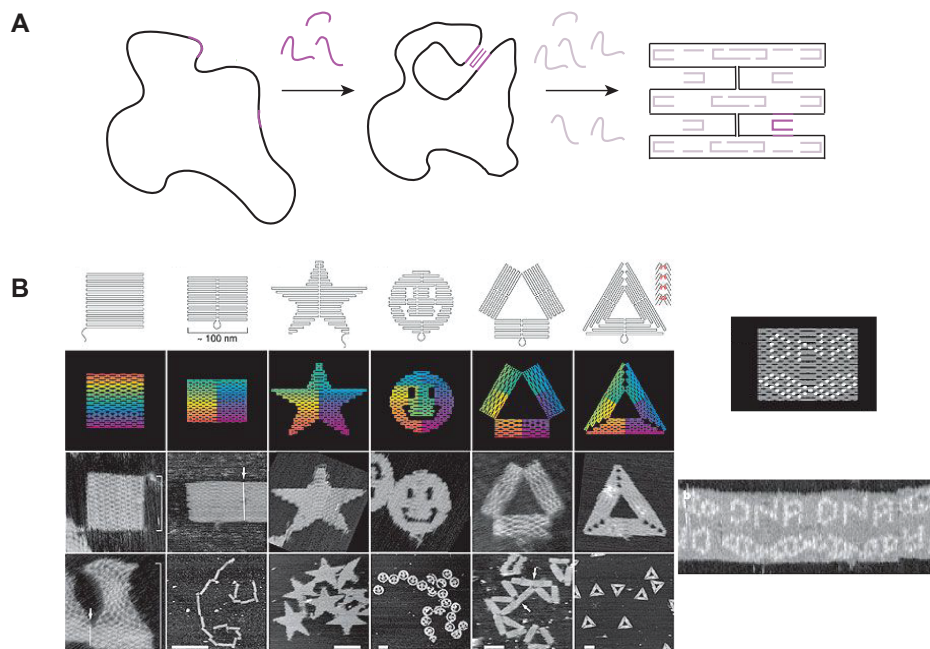


Figure 1.5: (A) The DNA origami technique: a single stranded circular scaffold strand is folded into a desired shape by short staple oligonucleotides. (B) Various shapes can be built by the DNA origami technique [32]. Among others the smiley shape is shown. Reprinted by permission from Springer Nature Customer Service Centre GmbH: Springer Nature, Nature, from ref. [32], copyright (2006).

### 1.3.3 DNA origami

One important development in DNA nanotechnology was the introduction of the DNA origami method by Paul Rothemund [32, 61]. Here a long single stranded DNA strand of around 7-8 kilo bases - the "scaffold" - is folded into a desired shape by short single stranded oligonucleotides, so called "staples", see Figure 1.5A. A structure is created in the form of parallel, interconnected DNA double helices. For the assembly the scaffold is mixed with carefully selected staples in a buffer of the appropriate salt concentration and subjected to an annealing process. The DNA origami structures can be imaged with AFM or TEM [32, 62]. The technique was first demonstrated by the creation of several two dimensional shapes - among others the smiley shown in Figure 1.5B [32].

The DNA origami concept has been extended from flat structures of one layer of connected double helices to three dimensional constructs [62]. Two design strategies for 3D arrangements have been developed that are often applied [62, 63], see Figure 1.6. In these designs the parallel DNA double helices are arranged in a honeycomb or square lattice. The design strategy can be explained in the following way: The natural repeat sequence of about 10.5 base pairs per turn for DNA free in solution gives a recurrence of the orientational position within the DNA helix at the 21st base. A connection of one DNA double strand to neighbouring antiparallel double strands can occur at every 7th base giving a connection to a neighbouring helix at an angle of  $120^\circ$  and therefore to three neighbours. This leads to a honeycomb arrangement of the DNA helices [62] (Figure 1.6A). A square

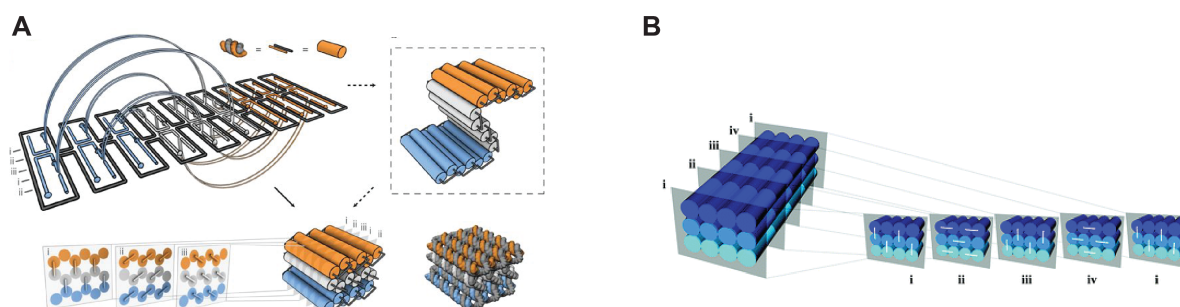


Figure 1.6: 3D DNA origami lattice types: For a three dimensional structure the DNA double helices can be arranged in a honeycomb lattice [62] (A) or in a square lattice [63] (B). (A) Reprinted by permission from Springer Nature Customer Service Centre GmbH: Springer Nature, Nature, from ref. [62], copyright (2009). (B) Reprinted with permission from ref [63]. Copyright (2009) American Chemical Society.

lattice of parallel double helices can be achieved by connecting DNA helices to four neighbouring helices [63], (Figure 1.6B). As the natural repeat of 21 bases does not comply with four neighbours to form straight structures, over and underwinding of the DNA must be accounted for in this case.

Furthermore, curvature and twist can be induced purposefully e.g. via addition and removal of single base pairs [64, 65]. The software caDNAno [66] aids the design process of DNA origami nanostructures. Predictions about three dimensional solution shape and flexibility of the designs can be obtained with the software CanDo [67, 68].

# Chapter 2

## Materials and methods in DNA nanotechnology

After the process of design and assembly the DNA nanostructures are purified using for example gel electrophoresis and imaged using an atomic force microscope (AFM) or transmission electron microscope (TEM). The techniques are described in the following [69, 70, 71, 16, 72]

### 2.1 Gel electrophoresis

Gel Electrophoresis is a technique used to separate charged macromolecules such as DNA or proteins by size and shape based on differences in migration speed through a porous gel matrix in the presence of an electric field. These differences in speed can originate, for example, from size or charge. Shorter or more compact structures have a higher migration speed through the pores of the matrix material than longer or extended ones. This means DNA of different lengths or conformations can be separated. The pore size of the matrix material has to be chosen according to the sizes of the structures to be separated. Common matrix materials are agarose and polyacrylamide. The pore sizes depend on the material and its concentration. The sample is filled into wells in the gel and placed in an electrophoresis chamber with a running buffer. A voltage is applied and due to its negatively charged backbone, the DNA migrates to the anode. After sufficient time for the separation of the structures has passed the gel can be imaged. To make the DNA visible the gel is stained with intercalating fluorescent dyes such as ethidium bromide and exposed to UV light. The different structures form distinct bands. The structures are usually ex-

tracted by band excision and purification from the gel matrix material. Gel electrophoresis is commonly used for purification of the folded DNA origami structures from the excess staples using the fact that the short staples migrate faster than the larger Origami structure. From the comparison of the folded structures to the scaffold strand migration speed an indication of the success of the folding can be gained. The compact folded structure usually moves faster than the scaffold. Furthermore, dimerization or aggregation of the structures become visible.

## 2.2 Transmission electron microscopy

For the imaging beyond the possibilities of the human eye optical microscopes serve well on the microscale. Abbes limit gives the smallest possible resolution  $d$  - the smallest distance at which two points can still be distinguished - as

$$d = \frac{\lambda}{2NA} \quad (2.1)$$

with the numerical aperture of the objective  $NA$ . The limit is reached when structures of the size of the wave length of light are to be imaged. For visible light the limit is around 200 nm. Lower wavelengths are required to image smaller structures. Electrons can reach low wavelengths when accelerated, following De Broglie  $\lambda = \frac{h}{p}$ . They can be guided using electro-magnetic lense systems. ”*[F]or his fundamental work in electron optics, and for the design of the first electron microscope*” Ernst Ruska received the Nobel Prize in Physics in 1986 together with Binning and Rohrer [11]. They enabled the imaging of matter on the nanoscale and beyond. In the imaging of DNA nanostructures the transmission electron microscope (TEM) plays an important role. In a TEM free electrons are usually generated based on thermionic emission from a filament and are accelerated. Typical acceleration voltages here are 80-400 kV with the lower range more suitable for biological samples. An electro-magnetic lense system is used to direct and focus the beam. The electron beam is kept in vacuum to prevent scattering by air molecules. The beam is sent through the sample that has to be sufficiently thin to allow for transmission of the electrons. The electrons which are not scattered or absorbed by the sample are detected for example on a fluorescent screen or a charge-coupled device (CCD) camera. Therefore objects with a material of high atomic number such as gold or silver nanoparticles appear clearly in

the images, while biological samples like DNA only show a low contrast. For solely DNA based nanostructures therefore a staining with heavy atoms is usually necessary. As a staining material we use Uranyl formate or acetate. Figure 2.1 shows examples of DNA

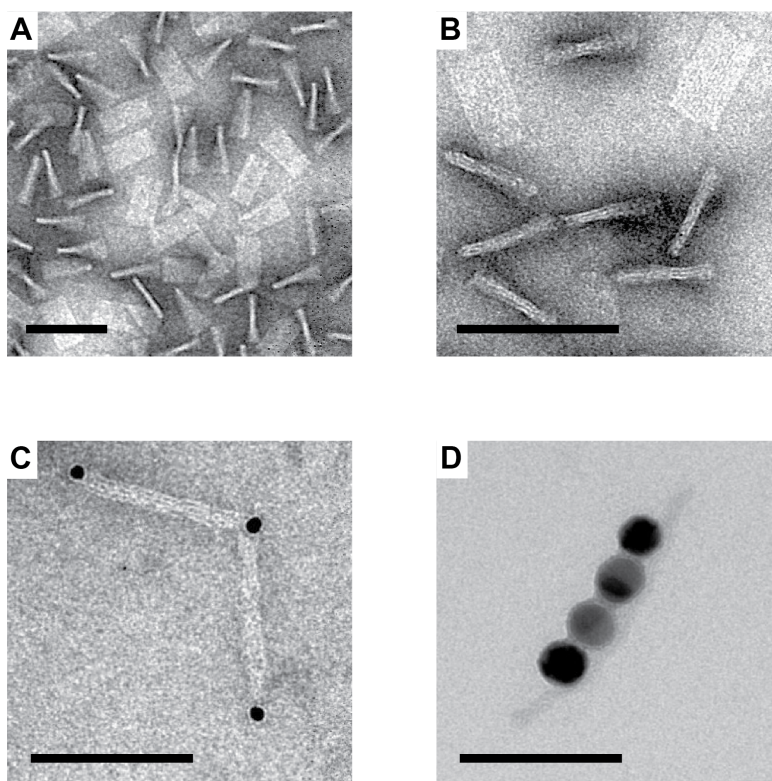


Figure 2.1: TEM images of DNA origami nanostructures. (A and B) Block shaped DNA origami structures are shown. Parallel double helices of the structures are visible. (C) Gold nanoparticles on DNA origami structures appear as dark dots. (D) Two silver nanoparticles in between two gold nanoparticles arranged on a DNA origami structure.

origami nanostructures imaged with TEM. Pure DNA origami structures (Figure 2.1A and 2.1B) have to be stained before imaging. The parallel double helices are visible. Gold nanoparticles on DNA origami structures appear as dark circles (2.1C). Two silver nanoparticles in between two gold nanoparticles arranged on a DNA origami structure are shown 2.1D. The different materials gold, silver and DNA can be distinguished. As the liquid samples of DNA nanostructures are dried in the preparation for TEM imaging, it has to be kept in mind that only a dried state of the structure is imaged.

## 2.3 Atomic force microscopy

The atomic force microscope is a scanning probe microscope with subnanometer resolution. In an AFM a cantilever with a sharp tip scans the surface of a sample while the deflection of the cantilever is measured, see Figure 2.2. It is deflected due to forces between the tip and the sample surface, thus probing the surface. The deflection of the cantilever can be detected by measuring the displacement of a laser beam reflected from the top of the cantilever with a photodiode. In the so called "contact mode" the deflection is used in a feedback loop to maintain a constant distance from the surface. For soft samples and imaging in liquid an intermittent contact or "tapping mode" is more suitable. In tapping mode the cantilever is driven to oscillate near its resonance frequency with an amplitude of nanometers. Interaction forces change the oscillation amplitude when the tip approaches the surface. The deflection amplitude serves as a feedback parameter. The AFM images in this thesis were taken in tapping mode in fluid.

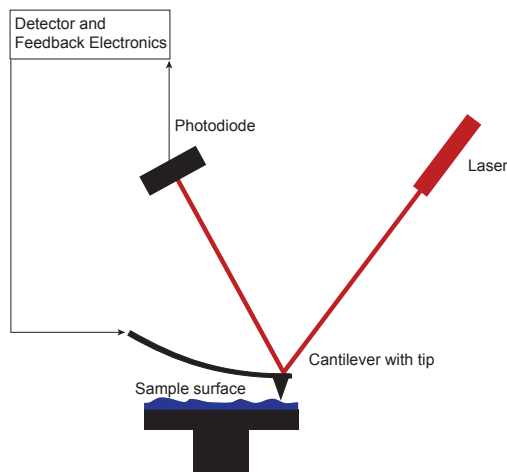


Figure 2.2: Scheme of an atomic force microscope. A tip on a cantilever scans the height profile of a sample. The deflection of the cantilever can be measured with a laser beam that is reflected from the top of the cantilever and detected with a photodiode.

## 2.4 Small-angle X-ray scattering (SAXS)

"*Photo 51*" which built the basis for the discovery of the double helical structure of DNA is the most famous example for the use of X-rays for elucidation of the structure of nucleic acids (Figure 2.3). Here I want to introduce the method of measurements of the small-angle X-ray scattering (SAXS) pattern that we use for characterization of DNA nanostructures in solution following ref. [73, 74, 75].

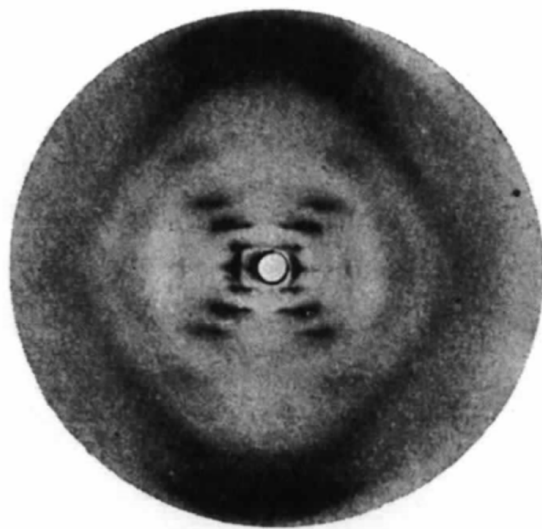


Figure 2.3: "*Photo 51*": X-ray fiber diffraction pattern of B-form DNA . Reprinted by permission from Springer Nature Customer Service Centre GmbH: Springer Nature, Nature, from ref. [20], copyright (1953).

SAXS can probe biological macromolecules in solution to determine their structure, conformations and interactions [76, 77, 78]. It can be used to probe structure in the range of 1-100 nm in a typical setup and has applications for example for biological materials, chemicals, polymers, pharmaceuticals and nanotechnology. In the relevant context it has been widely used for the characterization of proteins and nano objects such as AuNPs, AuNP assemblies and DNA assemblies [76, 79, 80, 81, 82]. Microscopy methods such as AFM, TEM and cryo-TEM which involve the presence of a surface, drying and staining or freezing can be complemented by SAXS. It can yield complementary information as it allows to probe assemblies directly in their native environment and therefore can also detect the environments influence on the structure.

In this chapter the basic principles of SAXS will be depicted following ref. [83, 73, 84, 74, 85]. First we will describe how the X-rays interact with the sample causing an

intensity pattern characteristic for its structure at small angles from the direct beam that is recorded in a SAXS experiment. Then the experimental setup will be described to explain how instrumental parameters influence the interpretation of the recorded data. Furthermore, we explain how the intensity curves can be interpreted by direct modeling and fitting or by transformation to real space.

### 2.4.1 Basics of SAXS

This chapter is following ref. [83, 73, 74, 75]. When X-rays are sent through the sample and interact, some are absorbed and some are scattered. Scattering can occur elastically or inelastically. If the scattered X-rays are coherent, they can interfere. For structure determination we here make use of coherent elastic scattering. Scattering arises from the electron density experienced by the propagating X-rays. As the wavelength of X-rays is in the nanometer range, electron density inhomogeneities at this length scale lead to interference phenomena. The contrast in the scattering pattern is related to the difference in electron density of the objects and the matrix material, in our case gold or DNA and an aqueous buffer, respectively. Furthermore, as all electrons within the illuminated sample volume can interact with the beam the scattering reflects the average over all objects and orientations. A detector records the 2D scattering intensity distribution with the interference pattern characteristic for the sample. For randomly oriented objects the scattering pattern is concentric around the beam. Radial integration reduces the pattern to a one dimensional scattering curve  $I(q)$ . Smaller structures scatter to wider angles and larger structures scatter to smaller angles. The challenge in SAXS is to prevent the scattering intensity that appears at small angles - typically about  $0.1-10^\circ$  - from being overshadowed by the direct beam.

The elastic scattering process can be described by the interaction of an incoming wave  $\vec{k}$  with the electrons of an object resulting in an outgoing wave  $\vec{k}'$  with the same magnitude of the wavevector  $|\vec{k}| = |\vec{k}'| = \frac{2\pi}{\lambda}$  but a different direction, see Figure 2.4. For a setup independent description equations are expressed in terms of  $q = |\vec{q}| = |\vec{k} - \vec{k}'|$  instead of scattering angle  $2\theta$  and the wavelength  $\lambda$ .

The change of the scattering vector is

$$q = |\vec{q}| = |\vec{k} - \vec{k}'| = \frac{4\pi}{\lambda} \sin \theta. \quad (2.2)$$

The scattering amplitude caused by an electron cloud can be described as follows: each

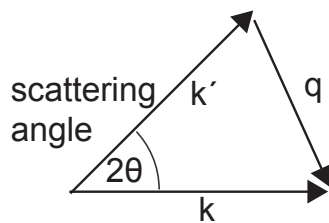


Figure 2.4: Geometrical relationship between the scattering vector and the scattering angle. Absolute value of incident wave vector and outgoing wave vector are identical in an elastic scattering event. The scattering vector  $q$  is given by their difference.

volume element  $d\vec{r}$  of the electron cloud at  $\vec{r}$  contributes with scattering length density contrast  $\Delta\rho(\vec{r})$  and phase difference  $e^{i\vec{q}\vec{r}}$ . The form factor characteristic for the shape of the scattering object is

$$F(\vec{q}) = \int_V d\vec{r} \Delta\rho(\vec{r}) e^{i\vec{q}\vec{r}} \quad (2.3)$$

i.e. given by the Fourier transform of the scattering length density contrast  $\Delta\rho(\vec{r})$ . The intensity is proportional to the squared absolute of the form factor.

$$I(q) \sim |F(\vec{q})|^2 \quad (2.4)$$

For non-centrosymmetric objects the random orientation of the objects in solution has to be taken into account. The average intensity for different orientations is denoted as

$$\langle I(q) \rangle_{orient.aver.} \sim \langle |F(\vec{q})|^2 \rangle_{orient.aver.} := P(q) \quad (2.5)$$

For some cases the form factor can be calculated analytically. Others have to be calculated numerically.

### 2.4.2 SAXS scattering profiles of basic geometries

The form factors of basic geometries used in this study will be given here [85, 86]. Intensity plots are prepared with SasView.

#### Form factor of a sphere

For spherical objects  $P(q) = |F(\vec{q})|^2$  where  $F(q)$  is the amplitude form factor. The form factor of a homogeneous sphere of radius  $R$  is calculated in a straightforward way from

the scattering length density contrast  $\Delta\rho = \rho_{sphere} - \rho_{buffer}$ , for  $r < R$  and 0 elsewhere: [85, 87, 86]

$$F_{sphere}(q) = \Delta\rho V_{sphere} \frac{3[\sin(qR) - qR \cos(qR)]}{(qR)^3} \quad (2.6)$$

The minima of the intensity of a sphere are given by  $\tan(qR) = qR$  and therefore occur for  $qR \approx 4.49, 7.73, 10.90$ . The minima of larger spheres occur at lower values of  $q$ . In Figure 2.5 intensity curves of spheres of typical radii of  $R=20, 10, 5$  and  $2.5$  nm are shown.

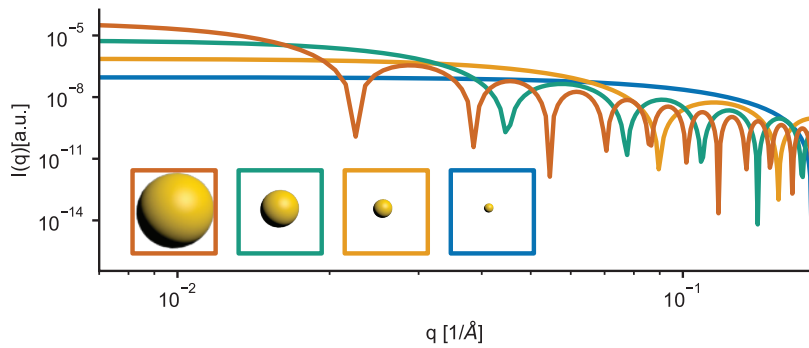


Figure 2.5: Influence of size on the scattering profile of a sphere. Radii of 20, 10, 5 and 2.5 nm are shown.

In the long wavelength limit  $qR \ll 1$  - the Guinier regime - the small-angle scattering of a sphere can be approximated by an expansion of the trigonometric functions. The intensity can be approximated by a Gaussian and can be used to determine the radius  $R$  of a spherical particle or the Radius of Gyration  $R_G$  for a non-spherical particle:

$$I_{sphere}(q \rightarrow 0) \sim e^{-\frac{(qR)^2}{5}} \quad (2.7)$$

In a Guinier plot the logarithm of the intensity is plotted versus  $q^2$  so that the radius can be extracted from the slope. In the short wavelength limit  $qR \gg 1$  - the Porod regime - the SAXS intensity  $I_{sphere}(q \rightarrow \infty)$  is proportional to the surface area and follows a powerlaw characteristic for its dimensionality. For a sphere it falls off as  $\sim q^{-4}$  for an infinitely thin disc as  $\sim q^{-2}$  and an infinitely thin rod as  $\sim q^{-1}$ .

### Polydispersity

For polydisperse solutions the scattering curves can be regarded as being composed of the form factors and therefore weighted by the respective contrast and volume. With a

distribution of particle size  $D(R)$  normalized to  $\int_0^\infty D(R)dR = 1$  the intensity given by

$$I_{polydisp}(q) = \int_0^\infty D(R) |(F(q, R))|^2 dR. \quad (2.8)$$

As the scattering intensity scales with the volume of the particles, larger particles in an ensemble dominate the signal. The scattering pattern of spheres of differing degrees of polydispersity are shown in Figure 2.6. For a higher polydispersity the minima become washed out.

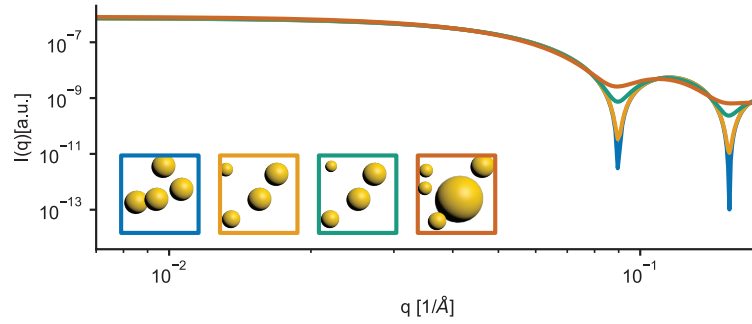


Figure 2.6: Influence of size polydispersity on the scattering profile of a sphere.

### Form factor of a sphere with a shell

The form factor of a sphere with a shell of differing density is calculated from its scattering length density contrast  $\Delta\rho = \rho_{sphere} - \rho_{buffer}$ , with  $\rho_c$  for  $0 < r < R_c$ ,  $\rho_s$  for  $R_c < r < R_s$  and  $\rho_0 = \rho_{solv}$  for  $r > R_s$  [87, 86] as

$$F_{coreshellsphere}(q) = \frac{1}{V_s} \left[ (\rho_c - \rho_s) V_c \frac{3 \sin(qR_c) - qR_c \cos(qR_c)}{(qR_c)^3} + (\rho_s - \rho_{solv}) V_s \frac{3 \sin(qR_s) - qR_s \cos(qR_s)}{(qR_s)^3} \right]$$

with  $V_c = \frac{4}{3}\pi R_c^3$  and  $V_s = \frac{4}{3}\pi R_s^3$ .

### Form factor of a cylinder

The form factor of a homogeneous cylinder is [85, 86]

$$F_{cyl}(q, \alpha) = \Delta\rho V_{cyl} 2 \frac{\sin(\frac{L}{2}q \cos \alpha)}{\frac{L}{2}q \cos \alpha} \frac{J_1(qR_{cyl} \sin \alpha)}{qR_{cyl} \sin \alpha} \quad (2.9)$$

with  $\alpha$  being the angle between the axis of the cylinder and  $\vec{q}$ ,  $\Delta\rho$  the scattering length density contrast,  $V_{cyl}$  the volume of the cylinder,  $L$  the length of the cylinder,  $R_{cyl}$  the radius of the cylinder,  $J_1$  the Bessel function of the first order. For randomly oriented cylinders the scattering intensity function is given by

$$I_{cyl,orient.aver.}(q) = \int_0^{\frac{\pi}{2}} |F_{cyl}(q, \alpha)|^2 \sin \alpha d\alpha \quad (2.10)$$

### Form factor of a block

The scattering intensity of a homogeneous block shaped object [88, 89, 86] with the side lengths A, B, C of the object fulfilling  $A \leq B \leq C$  and an orientation to scattering vector given by  $\alpha, \beta$  with  $\alpha$  being the angle between z-axis and the longest axis C of the parallelepiped,  $\beta$  the angle between the scattering vector in the xy-plane and the y-axis

$$F_{block}(q, \alpha, \beta) = \Delta\rho V_{block} \frac{\sin(\frac{A}{2}q \sin \alpha \sin \beta)}{\frac{A}{2}q \sin \alpha \sin \beta} \frac{\sin(\frac{B}{2}q \sin \alpha \cos \beta)}{\frac{B}{2}q \sin \alpha \cos \beta} \frac{\sin(\frac{C}{2}q \cos \alpha)}{\frac{C}{2}q \cos \alpha} \quad (2.11)$$

with  $V_{block} = ABC$ .

With an averaging over orientations the intensity is

$$I_{block,orient.aver.}(q) = \frac{2}{\pi} \int_0^{\frac{\pi}{2}} \int_0^{\frac{\pi}{2}} F_{block}^2(q, \alpha, \beta) \sin \alpha d\alpha d\beta \quad (2.12)$$

In Figure 3.2 in chapter 3.1 the scattering pattern of a cylinder and two block shaped structures similar to the overall-shape and dimension of the DNA nanostructures investigated are shown.

### Form factor of a dimer

For the scattering intensity of an aggregate of N spherically symmetric particles with form factor  $F_j(q)$  of the individual particles the amplitude is composed of the contributions of

the individual particles  $F(\vec{q}) = \sum_{j=1}^N F_j(q)e^{i\vec{q}\vec{r}_j}$  and therefore [74]

$$\begin{aligned}
 \langle I_{N\text{spheres}}(\vec{q}) \rangle_{\text{orient.aver.}} &= \langle |A(\vec{q})|^2 \rangle_{\text{orient.aver.}} \\
 &= \langle \left| \sum_j F_j(q)e^{i\vec{q}\vec{r}_j} \right|^2 \rangle_{\text{orient.aver.}} \\
 &= \sum_{j=1}^N F_j^2(q) + 2 \sum_{j=1}^{N-1} \sum_{k=j+1}^N F_j(q)F_k(q) \frac{\sin(d_{jk}q)}{d_{jk}q}
 \end{aligned} \tag{2.13}$$

with distance  $d_{jk}$  between the particle  $j$  and  $k$

We now consider a dimer of two particles. For two identical spheres  $F_j = F_{\text{sphere}}$  of fixed center-to-center distance  $D$  we get  $I_{\text{dimer}}(q) = F_{\text{sphere}}(q)^2 \cdot 2 \cdot (1 + \frac{\sin(Dq)}{Dq}) := P_{\text{sphere}}(q)S(q)$ . The structure factor  $S(q) := 2(1 + \frac{\sin(Dq)}{Dq})$  gives an oscillation around the monomeric intensity that changes with distance  $D$ . This behaviour is shown in Figure 2.7 on a log and linear scale. With the knowledge of the intensity of the monomeric particles the structure factor  $S$  can be extracted.

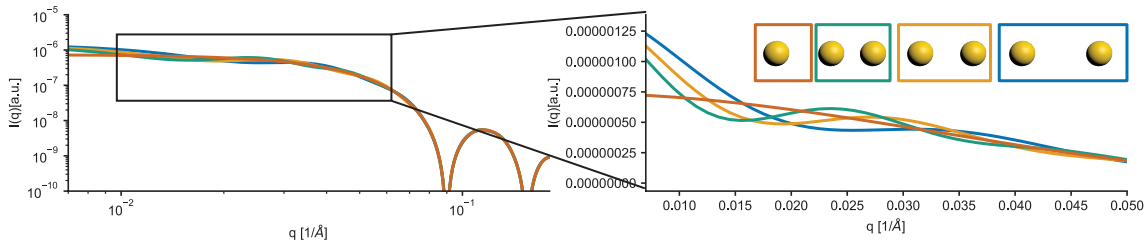


Figure 2.7: Influence of the distance of a dimer of spheres on the scattering profile on a loglog and linear scale. Center-to-center distances of 20, 25 and 30 nm with spheres of radius 5 nm and the scattering profile of a single sphere are shown.

### Scattering of crystalline materials

A short overview of scattering of crystalline materials is depicted following ref. [73, 74]. Crystalline materials are defined by their periodicity in space with unit cells placed with a regular repeat through a lattice specified by a set of vectors  $\vec{R}_n = n_1\vec{a}_1 + n_2\vec{a}_2 + n_3\vec{a}_3$  with  $n_1, n_2, n_3 \in \mathbb{N}$ , lattice vectors  $\vec{a}_1, \vec{a}_2, \vec{a}_3$  with its position within the unit cell  $\vec{r}_j$  and therefore scattering objects at position  $= \vec{R}_n + \vec{r}_j$ .  $d_{hkl}$  is the spacing of the lattice planes with Miller indices  $h, k, l$ .

Braggs law  $n\lambda = 2d \sin \theta$  describes the condition for constructive interference for scattering from crystal planes of distance  $d$  at scattering angle  $2\theta$  for wavelength  $\lambda$  and  $n \in \mathbb{N}$ . It is equivalent to the Laue condition: the wavevector change has to be equal to a reciprocal lattice vector  $\vec{q} = \vec{G}$ . From the description of the lattice, the peak positions can be calculated. For a 2D square lattice:

$$q_{hk}^{SQ} = \frac{2\pi}{d_{hk}^{SQ}} = \frac{2\pi}{a} \sqrt{h^2 + k^2} \quad (2.14)$$

i.e. diffraction peak ratios are  $1, \sqrt{2}, 2, \sqrt{5}$  and for a hexagonal lattice

$$q_{hk}^{HX} = \frac{2\pi}{d_{hk}^{HC}} = \frac{2\pi}{a} \sqrt{\frac{4}{3} \sqrt{h^2 + hk + k^2}} \quad (2.15)$$

i.e. diffraction peak ratios are  $1, \sqrt{3}, 2, \sqrt{7}, 3$  for a rhombohedral lattice

$$q_{hkl}^{RH} = \frac{2\pi}{a} \frac{\sqrt{\{(h^2 + k^2 + l^2) \sin^2(\alpha) + (hk + kl + hl)(\cos^2(\alpha) - \cos(\alpha))\}}}{1 - 3\cos^2\alpha + 2\cos^3\alpha}. \quad (2.16)$$

### SAXS profiles of lattices of arbitrary nano objects

Nanoscale lattice-arrangements can be studied in solution using SAXS. While in principle the assignment of the peaks due to periodic order on the nanoscale is straightforward, for quantitative data analysis it is required to account for certain factors and imperfections that are common in periodic nano arrangements compared to atomic crystals e.g. accounting for anisotropic constituents, multiple nanoobjects per unit cell, polydispersity and polymorphicity of the assembled nanoobjects and lattice defects [90]. Yager et al [90] describe a scattering formalism to predict and quantitatively fit such periodic lattices of arbitrary nano-objects. Starting point is a description of the lattice in terms of nano-object arrangements making up the unit cell making up the lattice described by the position vector  $\vec{r}_{njp} = \vec{r}_n + \vec{r}_j + \vec{r}_p$  with  $\vec{r}_n$  pointing to the origin of the unit cell,  $\vec{r}_j$  pointing from the origin of the unit cell to the center-of-mass of the particle  $j$  and the component  $\vec{r}_p$  that points from the center-of-mass of the particle to its final position in the lattice. The scattering intensity is modeled using [90]:

$$I(q) = P(q)S(q) = P(q) \left[ \frac{cZ_0(q)}{P(q)} G(q) + 1 - \beta(q)G(q) \right] \quad (2.17)$$

with a structure factor  $S(q)$  accounting for disorder from polydispersity and positional fluctuations.  $c$  is a scaling constant,  $P(q)$  is the average form factor intensity

$$P(q) = \left\langle \left| \sum_j^{N_j} F_j(\vec{q}) e^{i\vec{q}\vec{r}_j} \right|^2 \right\rangle_{eod} \quad (2.18)$$

with number of nano objects  $N_j$  in the unit-cell and the form factors  $F_j(\vec{q})$  for the objects in the unit cell. The subscript e, d, o denote averaging to account for the ensemble, the particle distributions and the orientation.

$[1 - \beta(q)G(q)]$  is the diffuse scattering with  $\beta(q)$  the effect of particle polydispersity

$$\beta(q) = \frac{\left| \left\langle \sum_j^{N_j} F_j(\vec{q}) \right\rangle_{eod} \right|^2}{\left\langle \left| \sum_j^{N_j} F_j(\vec{q}) e^{i\vec{q}\vec{r}_j} \right|^2 \right\rangle_{eod}} \quad (2.19)$$

approximating the non-oscillating part scaling as  $\beta(q) \approx \exp(-\sigma_R^2 R^2 q^2)$  for particles of radius  $R$  and a particle size distribution of finite width  $\sigma_R$ .  $G(q)$  is an exponential Debye-Waller factor  $G(q) = \exp(-\sigma_D^2 a^2 q^2)$  with relative root mean square particle displacement  $\sigma_D$  for a lattice of size  $a$  and the structural scattering

$$Z_0 = \frac{1}{q^{d-1}} \sum_{\{hkl\}}^{m_{hkl}} \left| \sum_j^{N_j} F_j(M_j \vec{q}_{hkl}) e^{[2\pi i(x_j h + y_j k + z_j l)]} \right|^2 \cdot L(q - q_{hkl}) \quad (2.20)$$

With the peak shape function  $L(q - q_{hkl})$  and  $q_{hkl}$  of reflection  $hkl$ , and its multiplicity  $m_{hkl}$ , the rotation matrix  $M_j$  accounting for the relative orientation of the particle  $j$  within the unit cell and  $x_j, y_j, z_j$  the fractional coordinates within the unit cell.

### 2.4.3 SAXS setup

The considerations relevant for the interpretation of the data include geometric information such as sample to detector distance, wavelength and its uncertainty, beam position and a possible tilt, detector information such as pixel size and other measured quantities such as transmission and background and are used for reduction of the 2D detector image to a one dimensional intensity curve  $I(q)$  with uncertainty  $\Delta q$  and  $\Delta I$ . A comprehensive discussion for SAXS pattern collection and correction is given by [91]. Here I shortly present the

instrumentation used for collection of the SAXS pattern. Data for the projects shown in this thesis were recorded at an inhouse setup [92] and at various synchrotron facilities: DESY, ELETTRA and ESRF.

A scheme of a SAXS setup can be found in Figure 2.8. The X-ray beam travels from the X-ray source via the collimation path to the sample mounted at the sample stage. The scattered X-rays as well as the direct beam travel through a vacuum tube that prevents air scattering. The beamstop blocks out the direct beam. The detector records the scattering pattern.

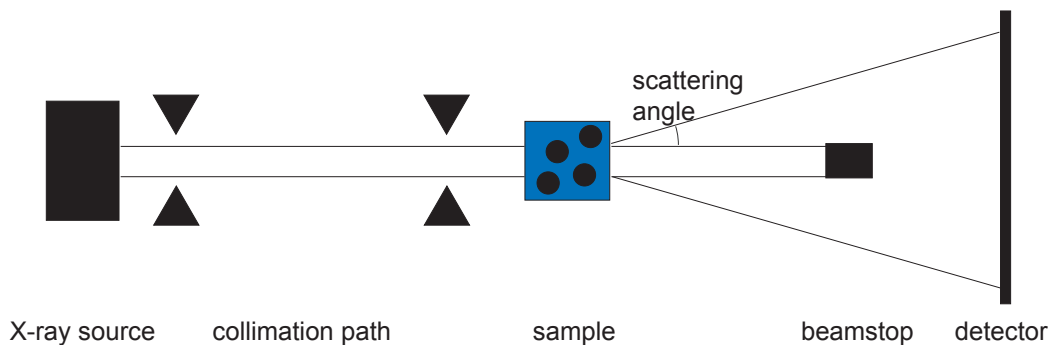


Figure 2.8: Scheme of a SAXS setup.

### In-house setup

The in-house setup will shortly be described here [92, 93]. As a source serves a mikrofocus X-ray tube with a molybdenum anode. With the  $K_{\alpha} = 17.4$  keV of molybdenum we have a wavelength of  $\lambda = 0.71$  Å. Collimation is achieved with two scatterless slits in this setup. The beam size is about  $1.2 \times 1.2$  mm<sup>2</sup> and the maximum beam divergence is 0.16 mrad. The flux is about  $2.5 \cdot 10^6$  photons/s. The Sample stage is connected to a heating/cooling system to allow the observation of the sample in differing ambient temperatures. Sample chambers are made from aluminum or polyvinyl chloride (PVC) and have a thickness of 1cm. PVC sample chambers are used for samples containing gold nanoparticles. Two vacuum tubes of different lengths are available for the two sample to detector distances of 1100 mm or 2500 mm with q-ranges from  $0.009$  Å<sup>-1</sup> to  $0.15$  Å<sup>-1</sup> to  $0.014$  Å<sup>-1</sup> to  $0.38$  Å<sup>-1</sup>, respectively. The semi-transparent beamstop consists of lead tape glued to the Kapton foil sealing the vacuum tubes. A Pilatus 100K (Dectris Ltd, Switzerland) with a pixel size of  $0.172$  mm  $\times$   $0.172$  mm and a total area of  $83.8 \times 33.5$  mm<sup>2</sup> serves as a detector. Motors

are used to position slits, sample stage and the vacuum tube with the beamstop via the spec software. Here usually multiple exposures with a duration of one hour were taken. The sample to detector distance and beam center is calibrated using the characteristic 2D scattering pattern of concentric rings of silver behenate (AgBe) as a standard.

#### 2.4.4 Sample considerations

The optimal thickness of the sample depends on material and the wavelength of the X-rays. Absorption has to be kept small while the sample volume has to be large enough for sufficient scattering to occur. As the scattering intensity is proportional to the illuminated sample volume as well as the transmission given by  $T = I(z)/I_0 = e^{-\mu z}$  for a sample of thickness  $z$  with the linear absorption coefficient  $\mu$ , the optimum sample thickness is given by  $z_0 = \frac{1}{\mu}$ . For X-rays using the  $K_\alpha$  of a molybdenum anode with  $\lambda = 0.071$  nm measuring a sample of water the optimum sample thickness is about 1 cm. To tell apart the scattering pattern of the object of interest from the background of the matrix the scattering length density contrast between the sample material and the matrix material has to be high enough. As the contrast increases with electron density difference, higher concentrations are needed for samples of lower atomic numbers in water.

#### Synchrotron facilities

Measurements at synchrotron facilities have the advantage of high flux and short exposure times. A short introduction is given following ref. [74]. Synchrotron radiation is the electromagnetic radiation produced by accelerated charged particles. In the 1970s the idea emerged that the synchrotron radiation stemming from the charged particles circulating in the storage rings of particle accelerators built for high energy nuclear physics experiments can serve as X-ray sources with high intensity and versatility. Since then many storage rings dedicated to the delivery of X-rays have been constructed. Main components that are found in typical experimental beamlines at third generation synchrotron sources are shown in the scheme in Figure 2.9. The charged particles - usually electrons - are kept circulating in the storage ring at constant energy at relativistic speed. They are kept on a circular path by bending magnets. An efficient production of X-rays is achieved using insertion devices: wigglers or undulators. In these devices the electrons are forced by arrays of magnets of alternating field direction on an oscillatory path. An undulator is constructed to cause small oscillations where different contributions of the oscillation of a single electron add

coherently and yield X-ray beams of high brilliance. With the use of a monochromator a particular wavelength band can be selected from the incident beam. On the basis of Bragg's law robust perfect crystals that can withstand the heat produced by the incident beam serve for this purpose. Silicon is the main material used for monochromators at synchrotron facilities, due to its availability, versatility and thermal expansion properties. X-ray mirrors or compound refractive lenses can serve as a focusing device for the beam.

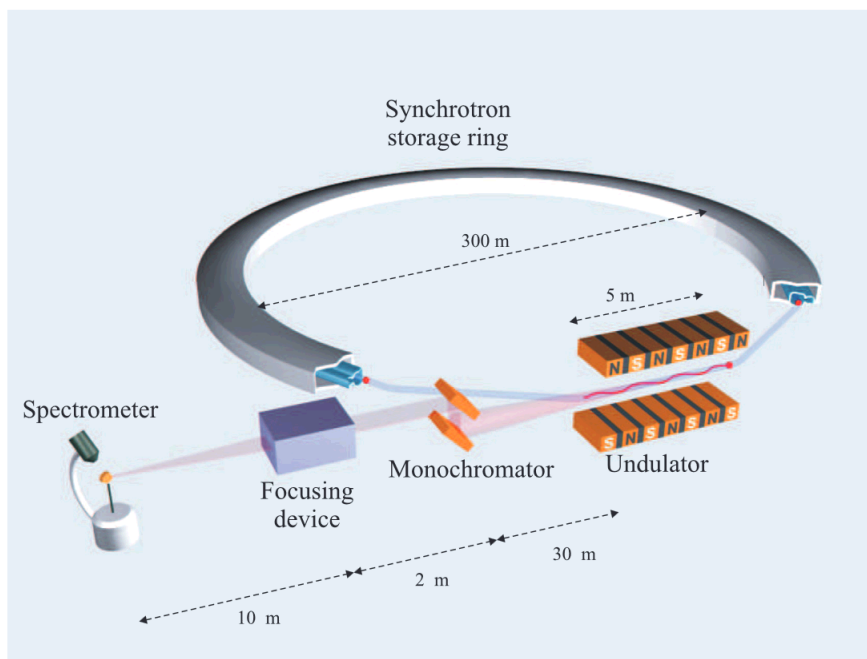


Figure 2.9: Scheme of a typical X-ray beamline at a third generation X-ray source. The charged particles circulating in the storage ring are forced on to execute small oscillations by alternating magnets when passing insertion devices in the straight sections. This produces intense beams of radiation. A number of optical elements gives the beam the required properties [74]. From ref. [74] Copyright (2011) by John Wiley & Sons, Ltd. Reprinted by permission of John Wiley & Sons, Ltd.

The data used for the three projects that are part of this thesis was recorded at three synchrotron facilities: "Deutsches Elektronen Synchrotron" (DESY) in Hamburg, Germany; "European Synchrotron Research Facility" (ESRF) in Grenoble, France, and the ELETTRA Synchrotron in Trieste, Italy.

The measurements at the DESY P08 beamline and at ESRF ID01 were performed by Stefan Fischer, Kilian Frank and Bert Nickel. The ELETTRA SAXS beamline uses a 57-pole wiggler, a double-crystal monochromator, collimation is achieved by a slit system. [94] The X-ray energy was 8 keV with  $\lambda = 1.54 \text{ \AA}$ . At the ESRF ID02 beamline [95] one of

three undulators can be selected as X-ray source. Components are a liquid nitrogen cooled channel-cut Si-111 monochromator and a toroidal mirror for collimation. The beamline was used with a wavelength of  $\lambda = 0.995 \text{ \AA}$  corresponding to 12.46 keV. Detectors can be moved in a vacuum tube to sample to detector distances from 1-31 m.

### 2.4.5 SAXS data interpretation

#### SAXS data treatment

The recorded scattering intensity pattern is transformed with the instrument parameters to a 1D scattering curve  $I(q)$  in terms of  $q$  that shows the characteristics of the sample. IgorPro plugin NIKA [96] was used for the reduction of the recorded 2D scattering pattern via circular averaging to a 1D scattering intensity for the inhouse setup. The median of multiple recordings is taken to remove outliers. The characteristic 2D scattering pattern of concentric rings of silver behenate is used for calibration of the sample-to-detector distance. Then typically the scattering intensity of the buffer is subtracted as a background. The scattering curve  $I(q)$  obtained this way is characteristic for the measured sample and in the following, the data can be analysed by fitting of a model to  $I(q)$  or by transformation to real space.

#### The pair density distribution function

The scattering data can be interpreted by transformation to real space [85, 77]. The Pair density distribution function (PDDF)  $P(r)$  is obtained by Fourier transformation of the experimental scattering curve via

$$I(q) = 4\pi \int_0^{\infty} \gamma(r)r^2 \sin(qr)/qr dr. \quad (2.21)$$

Its relation to the electron density is  $P(r) = r^2\gamma(r)$  with  $\gamma(r) = \langle \rho(\vec{r}) * \rho(-\vec{r}) \rangle$ . The PDDF provides direct information about the distances between electrons in the scattering object. The Fourier transformation is usually performed making use of the indirect Fourier transformation methods [97]. The PDDF equation analogous to the Debye formula in real space for  $N$  spheres is [98]

$$\langle P_{Nspheres}(\vec{r}) \rangle_{orient.aver.} = \sum_{j=1}^N \rho_j^2 p_0(r, R_j) + 2 \sum_{j=1}^{N-1} \sum_{k=j+1}^N \rho_j \rho_k \tilde{p}(r, d_{jk}, R_j, R_k) \quad (2.22)$$

with the distance distribution function  $p_0(r, R_j) = \frac{4\pi}{3} R_j^3 r^2 - \pi R_j^2 r^3 + \frac{\pi}{12} r^5$  of a sphere of radius  $R_j$  and electron density equal to unity and the cross term distance distribution  $\tilde{p}(r, d_{jk}, R_j, R_k)$  of sphere  $j$  and  $k$  with radius  $R_j$  and  $R_k$  at a distance  $d_{jk}$  as in [98].

The PDDF of spherical particles of different sizes and of dimers of spherical particles are shown in Figure 4.2. Transformation to real space is performed with the software GNOM [99, 100] from the ATSAS package or the proprietary software GIFT [101] via indirect Fourier transform. In the indirect Fourier transform, trial  $P(r)$  functions are Fourier transformed and compared to the experimental data.

### Model fitting and software

Model fitting is performed with the software *SasView* [102]. Different form factors and structure factors are contained in the library. Parameters can be fitted to obtain size, polydispersities etc.

For quantification of the difference of the observed data set  $Y_i$  from the expected dataset  $Y_{theory,i}$   $\chi^2$  is used.

$$\frac{\chi^2}{N_{pts}} = \sum \frac{(Y_i - Y_{theory,i})^2}{Y_{error,i}^2} / N_{pts} \quad (2.23)$$

with the number of data points  $N_{pts}$  [86]. As optimizer for example the gradient descent Levenberg-Marquardt algorithm can be used which is fast but will find local minima only or the population based more robust but slower DREAM optimizer [86].

Furthermore, the ATSAS data analysis software is a program suite for SAXS analysis for biological macromolecules [103]. The software CRY SOL [104] from the ATSAS package can determine solution scattering intensities from PDB files of objects of known atomic structure. PDB files can be obtained from CanDo [67] from a nanostructure design file from caDNAno [66]. The software tools GNOM [99, 100] from the ATASAS package and software GIFT [101] can be used for the transformation of the data to real space.

# Chapter 3

## SAXS for characterization of DNA origami structures<sup>1</sup>

Design and assembly of DNA origami nanostructures are well established. However, design details such as crossover density, position of staple strand breaks, sequence selection, etc. can influence the structural properties [106, 107]. Furthermore, environmental conditions such as changes of the salt concentration can induce structural changes that have to be accounted for in applications where precision in placing nano objects is a key element.

Established methods to prove successful assembly and determine structural features of DNA nanostructures are AFM and electron microscopy. However, drying, staining, freezing or the presence of a surface required for the imaging of the sample can influence the native environment and therefore induce structural changes during the imaging process. On the other hand, SAXS measurements of the sample can be performed in solution, and thus enable the determination of structural properties of DNA origami objects in their native, hydrated state. SAXS can therefore serve as a complementary method for characterization of DNA nanostructures in solution [108, 79]. In this chapter I will discuss how structure

---

<sup>1</sup>This chapter is based on the publication "*Shape and Interhelical Spacing of DNA Origami Nanostructures Studied by Small-Angle X-ray Scattering*", Stefan Fischer, Caroline Hartl, Kilian Frank, Joachim O. Rädler, Tim Liedl, and Bert Nickel, *Nano Letters*, 16 (2016), 4282-87. doi: 10.1021/acs.nanolett.6b01335. Adapted with permission from [105]. Copyright (2016), American Chemical Society. (Sections: 3.2.1-first part of 3.2.4 and corresponding Supplementary Information.)

Author contributions:

S.F. and C.H. contributed equally to this work, T.L., B.N., C.H., S.F. designed the research, C.H. prepared the assemblies, S.F. and K.F. performed the SAXS measurements and the fitting of the data, S.F. prepared the Figures and C.H. wrote the first draft of the manuscript. All authors interpreted the results and modified the manuscript.

and structural changes in pure DNA origami can be probed with SAXS.

### 3.1 The shape of DNA origami

DNA origami structure can be modeled using different levels of detail, see Figure 3.1A. The

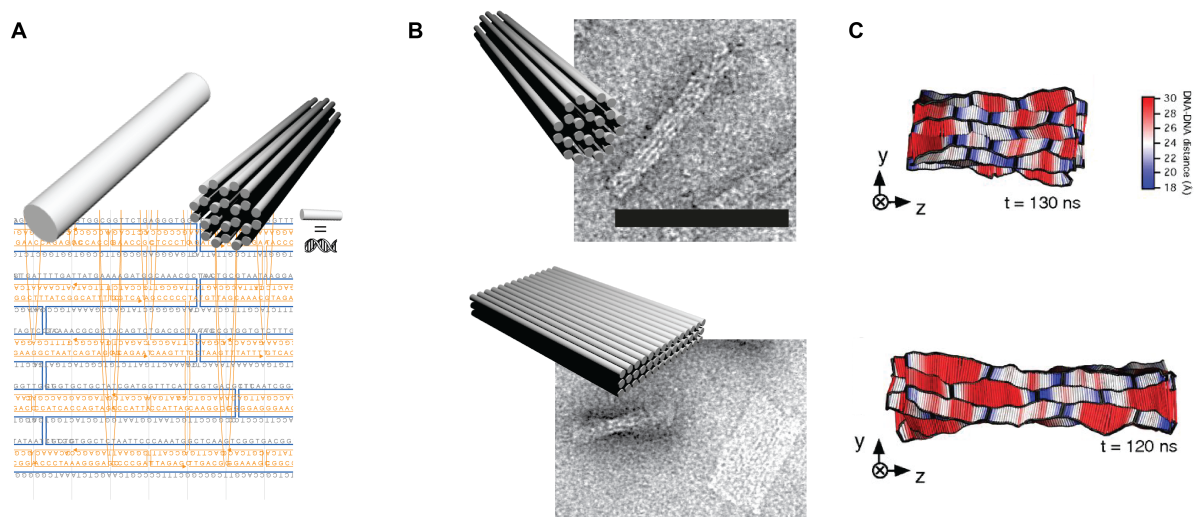


Figure 3.1: Representations of the DNA origami structure: (A) Target shape of the DNA object, representation by cylinders corresponding to the DNA double helices, and part of caDNAno design with specific sequences. (B) Models with cylinders representing double helices and TEM images of two 3D structures probed in this study with square lattice and honeycomb lattice cross section (C) Molecular dynamics simulation of two DNA origami structures of a honeycomb (upper image) and square lattice type (lower image) [109]. Wire frame (black lines) connects the centers of mass of the DNA base pairs that form continuous double-stranded DNA cylinders or crossovers of the original DNA origami designs. The lines between the centers of mass of the same index base pairs connect the wire frame and length of the lines indicates the local inter-DNA distance, which is color-coded from 18 Å (blue) to 30 Å (red). (Relaxation time is 130 and 120 ns, respectively.) . Reprinted from ref. [109], copyright (2013) National Academy of Sciences.

first level of detail is equivalent to the overall target-shape of the structure. The second level corresponds to the second step in the design process of DNA origami where the desired shape is represented as a composition of perfectly straight parallel cylinders representing the double helices (Figure 3.1B). A third level of detail follows from the fact that the helices are connected by staple and scaffold crossovers and from the atomic composition of the double helices. At the connection points of the double helices - the corresponding holliday

junctions - the DNA helices are held together closely [32, 109]. A chicken-wire structure arises, that can readily be seen in AFM images [32], see Figure 1.5 and 3.1C.

## 3.2 SAXS for characterization of DNA origami structures

Here I shortly describe the results of the SAXS measurements on pure DNA origami nanostructures and then a detailed discussion is given. In the project described in this chapter the scattering profiles of three different structures - a block, a sheet and a cylinder - with three different types of cross-sections (3.1) were investigated. Three dimensional cross sections of the honeycomb and the square lattice and a one layered structure are chosen. The theoretical scattering pattern of the basic shapes have been discussed in the introduction in chapter 2.4.2. Figure 3.2 shows the calculated scattering pattern of approximate overall shapes represented by a cylinder of radius 8 nm and length 100 nm, a block of size 57 nm  $\times$  36 nm  $\times$  7 nm and a sheet of size 76 nm  $\times$  62 nm  $\times$  2 nm.

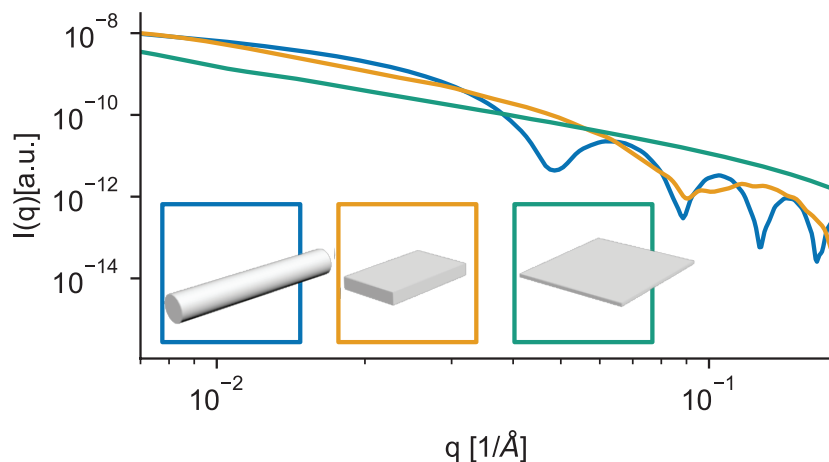


Figure 3.2: Calculated scattering intensities of the shapes of the DNA origami objects investigated here: cylinder of radius 8 nm and length 100 nm, a block of size 57 nm  $\times$  36 nm  $\times$  7 nm and a sheet of size 76 nm  $\times$  62 nm  $\times$  2 nm.

We will see, that the calculated scattering intensities agree well with the experimental values in the lower  $q$  range. An additional peak is found at higher  $q$  values. This peak is also found for a model that uses a representation of the DNA origami structure as an arrangement of parallel cylinders representing the double helices. The position of the peak is influenced by the interhelical distance in the arrangements. This means that the

overall shape of the objects as well as the average interhelical distance can be obtained from SAXS. As a next step the possibility for revelation of overall shape and interhelical distance is used to identify structural changes induced by environmental influences such as salt concentration and temperature.

To assess structural changes of DNA origami with changes in ionic strength, the structure of the cylindrical DNA origami under exposure to buffers of  $\text{Mg}^{2+}$  concentrations between 0 and 11 mM was probed. A disappearance of the structural features in the scattering pattern at  $\text{Mg}^{2+}$  concentrations below 2 mM Mg and a Debye like swelling of DNA nanostructures exposed to lowering  $\text{Mg}^{2+}$  concentrations was found. While a swelling is observed for DNA nanostructures exposed to lowering salt concentrations above its disassembly threshold, no indication of swelling is found for the disassembly at increasing temperatures. Additionally, it was found, that the assembly process could be performed in situ and monitored. The findings show that in principle SAXS measurements can be used to identify and possibly tune the structural properties and behavior of DNA origami to changing environmental conditions.

### 3.2.1 Shape and inner structure of DNA origami

Three DNA origami structures were assembled, concentrated, and analyzed via SAXS. As a first structure, we selected a twist-corrected variant of the canonical one-layer sheet of parallel DNA helices (Figure 3.3a) [32]. Second, we investigated a brick-like object built of three layers of parallel helices arranged on a square lattice (three-layer block) [52, 63]. In this design, all inner helices are connected to four neighboring helices (Figure 3.3b). Third, we used a cylinderlike structure [110] of the honeycomb-lattice type [62], where each of the inner helices is connected to three neighboring helices (24-helix bundle, Figure 3.3c).

Imaging with TEM or liquid tapping mode AFM confirmed successful and high-yield assembly of all three objects. The concentration of each structure was estimated by absorption spectroscopy. For SAXS measurements we worked with concentrations of  $\sim 250$  nM, which corresponds to 1.25 mg/ mL of DNA (molecular weight of all structures  $\sim 5$  MDa). Concentrated DNA origami samples were initially probed with our in-house SAXS setup [92] and experimental data with superior statistics in the low intensity region were obtained at synchrotron sources (P08 at DESY and ID1 at ESRF). The SAXS data for our three model systems (sheet, brick, cylinder) together with design schemes and TEM and AFM micrographs are summarized in Figure 3.3. The SAXS intensity distributions for the three model structures show very distinct and characteristic curves in log-log rep-

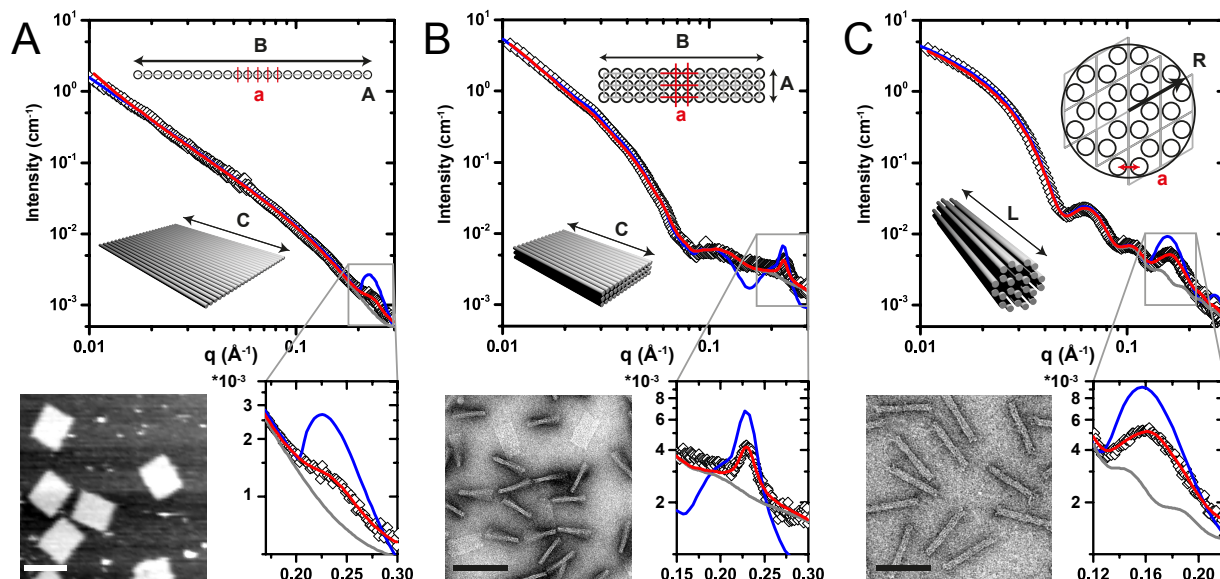


Figure 3.3: Small angle X-ray scattering intensity of three different types of DNA origami structures in solution with corresponding model, lattice structure (with unit cell) and AFM or TEM image: (A) one-layer sheet, (B) three-layer block with square lattice design, and (C) 24-helix bundle with honeycomb lattice design. Three different model fits are shown for each intensity plot. The geometric model takes only the overall shape - that is, sheet, block, or cylinder - into account (gray lines). A model treating the double helices as rigid cylinders predicts the existence and position of a peak corresponding to interhelical distance but overestimates the peaks intensity (blue lines). The combination of the geometric model with a Lorentzian peak attributed to the interhelical arrangement reproduces the scattering intensity with high accuracy (red lines). Scale bars: 100 nm.

resentation of scattered intensity ( $I$ ) versus the scattering vector ( $q$ ). In our experiments, the  $q$  values cover the range from  $0.01 \text{ \AA}^{-1}$  to  $0.3 \text{ \AA}^{-1}$ . This interval corresponds to real space distances of 2 nm up to about 60 nm, that is, the X-ray data contains information on the overall origami shapes and their inner structure.

On first sight, the intensity of the monolayer sheet exhibits a  $q^{-2}$  behavior for small  $q$  values as predicted from Porods law for two-dimensional objects [83]. The scattering signal of the brick shows different slopes in the log-log plot owing to its three different lateral dimensions and a dip at  $0.08 \text{ \AA}^{-1}$  due to its thickness. The cylindrical 24-helix bundle has the most pronounced scattering features due to its rotational symmetry. The minima and maxima of the scattered intensity stem from the radius of the helix bundle. For the detailed form factor, we refer to the Supporting Information (eq A.3).

We analyzed our data by geometric models, which approximate the origami structures

by homogeneous geometric bodies. We here use the analytical Fourier transform of a sheet, brick, or cylinder, respectively, and we account for free oligonucleotides in solution by adding a Debye background with a radius of gyration  $R_g$  representing a Gaussian chain [79, 111]. As the objects are oriented randomly in solution, we integrated numerically over all possible angles between the axis of the objects and their  $q$  vector. For small  $q$  values up to  $0.15 \text{ \AA}^{-1}$ , this model matches the intensity for all three objects (gray lines in Figure 3.3).

Overall the dimensions obtained from the geometric model analysis agree very well with the design parameters. The sheet has a thickness  $A = 21.5 \pm 0.3 \text{ \AA}$ , a width  $B = 610 \pm 60 \text{ \AA}$ , whereas the length  $C$  was fixed to  $960 \text{ \AA}$ . The brick has a length  $C = 627 \pm 5 \text{ \AA}$ , a width  $B = 379 \pm 2 \text{ \AA}$ , and thickness  $A = 76.6 \pm 0.2 \text{ \AA}$ . The 24-helix bundle modeled as a cylinder has a radius of  $78.7 \pm 0.2 \text{ \AA}$ . Note that the uncertainties diverge when the characteristic dimensions approach the resolution limit. Dimensions that are too large to be resolved by the SAXS experiments, such as the cylinder length of  $L = 100 \text{ nm}$ , do not influence our analysis. Exact fit parameter values for all dimensions can be found in the Supporting Information Table A.2.

In all cases, the geometric model is not able to describe the scattered intensities in the region of high  $q$  values ( $0.15\text{-}0.3 \text{ \AA}^{-1}$ ). This  $q$  region corresponds to real space distances of  $2.1 \text{ nm} - 4.2 \text{ nm}$ ; that is, here, the inner structure of the DNA origami is probed. In order to refine our model in this region, we represented each DNA double helix by a straight cylinder with diameters of  $2.0$  and  $2.2 \text{ nm}$ . The distance between the cylinders is varied until this model reproduced the observed peak positions in the high  $q$  region (blue curves in Figure 3.3 shows solution for  $2.2 \text{ nm}$  diameter). These peaks represent the Bragg condition of the inner arrangements of the DNA double helices that arise from the different lattice design principles (linear, square, and hexagonal; unit cells are shown in Figure 3.3).

This model, however, consistently overestimates the interhelical peak intensities. Because we idealize the electron distribution of a DNA double helix by a full cylinder, we neglect atomistic structure. Using more realistic but still analytical helix models including a continuous single helix [112] and a continuous double helix improved the quality of the fits only slightly. Simulations of scattering intensities calculated from (quasi)atomistic models obtained from computational tools [68, 67, 113, 104], on the other hand, resulted in good intensity matching for the 24-helix bundle. Unfortunately, this procedure did not improve the fits for the other two structures suggesting that these models require refinement. A problem here may be the wellknown chicken-wire-like structure of the DNA helices in

DNA origami [32, 63, 114], which is not taken care of in the above models. Therefore, we combine the geometric model with a Lorentzian peak centered at  $q_0 = 2\pi/d$ , probing the helical lattice planes  $d$  (cf. Supporting Information eq A.7-A.10). This model yields nearly perfect description of all the experimental intensity data (red line in Figure 3.3). In detail, for the one layer sheet, we obtain an interhelical distance of  $26.9 \pm 0.2 \text{ \AA}$ , similar to the cubic lattice spacing of the brick, which is  $27.32 \pm 0.02 \text{ \AA}$ . The interhelical distance measured for the honeycomb lattice of the 24-helix bundle is  $25.36 \pm 0.03 \text{ \AA}$ . These values agree well with lattice parameters obtained from CryoEM, where an effective helix diameter of 2.6 nm was observed [114] and from molecular dynamic simulations [115, 109]. Note that all these literature values have been obtained under buffer conditions that favor DNA origami stability, that is, 10 mM or more of  $\text{Mg}^{2+}$  and temperatures below  $30 \text{ }^\circ\text{C}$ . We will now address the question to which extend origami structure and shape change with temperature and ionic strength.

### 3.2.2 Structure of DNA origami in different salt concentrations.

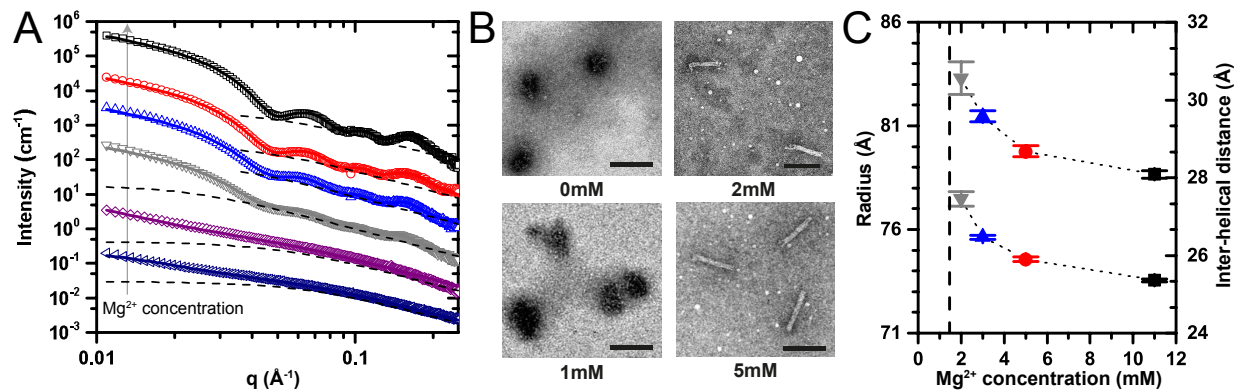


Figure 3.4: (A) Scattering curves of 24-helix bundles at varying  $\text{MgCl}_2$  concentrations (11 mM, 5 mM, 3 mM, 2 mM, 1 mM, and 0 mM from top to bottom) with Debye background (dashed lines). (B) TEM images of DNA structures exposed to 0 mM, 1 mM, 2 mM, and 5 mM  $\text{MgCl}_2$ . Scalebars: 100 nm. (C) Radii of the overall cylinder-shaped structure and interhelical distances extracted from (A) and Debye length for the corresponding  $\text{MgCl}_2$  concentrations.

We expose the 24-helix bundle to different  $\text{Mg}^{2+}$  concentrations at room temperature. The scattering of the samples in buffer of 0, 1, 2, 3, 5, and 11 mM  $\text{MgCl}_2$  is summarized in Figure 3.4A. The typical oscillations of the scattering intensity are recognizable for all samples down to 2 mM  $\text{MgCl}_2$ . However, with decreasing  $\text{Mg}^{2+}$  concentration, characteristic

features are less pronounced and the scattering at low  $q$  drops significantly. Ultimately, for a  $\text{MgCl}_2$  content of 1 mM and 0 mM, the origami scattering features vanish completely. The remaining scattering intensity is a combination of the general Debye background (cf. eq A.5) and a second Debye term with a radius of gyration of about 20 nm, which can be considered as a contribution from the dismantled DNA origami structure. Complementary TEM micrographs support this scenario qualitatively, that is, we still find predominantly intact structures for 2 mM  $\text{MgCl}_2$  and only dismantled objects at 1 mM and 0 mM  $\text{MgCl}_2$  (Figure 3.4B).

In order to quantify the structural changes in response to the  $\text{MgCl}_2$  concentration, we evaluated both the interhelical distance and the diameter of the whole origami cylinder (Figure 3.4C). With decreasing  $\text{MgCl}_2$  content both values increase up to 10% in a strongly correlated manner before the structures fully dismantle (cf. Supporting Information Figure A.4).

The expansion as a function of decreasing salt reflects the interplay of the electrostatic repulsion between the negatively charged DNA phosphate backbone and the elastic restoring forces of the internal DNA origami crossovers within the origami framework. The electrostatic Coulomb potential is well known to be screened by salt [116, 115] and increases at reduced ionic strengths. Interestingly, the relative change of the interhelical distance mirrors the behavior of the calculated Debye length of the  $\text{Mg}^{2+}$  ions (Figure 3.4C) suggesting that the main role of the  $\text{Mg}^{2+}$  ions is Debye screening rather than specific effects such as ion bridging [117]. This observation is in line with molecular dynamics simulations, which have already shown that the origami framework prevents the proper relative orientation of the DNA double helix needed to form ion bridges in the first place [115, 118]. Note that the observed origami lattice expansion prior to disassembly of up to 10% is rather characteristic for classical solids, whereas hydrogels show orders of magnitude larger swelling capability. Reducing the number of crossovers might allow to tune the origami mesh swelling, for example, for the fabrication of molecular sieves.

### 3.2.3 Annealing and melting of DNA origami structures.

Next, we study the annealing and melting of a 24-helix bundle origami by ramping the temperature while recording X-ray data. We focus on two parameters, which highlight different structural aspects of folded DNA origami architectures; first, the scattered intensity in the limit of small  $q$ , which is a measure for the fraction of folded structures (Figure 3.5A), and second, the intensity of the interhelical peak (Figure 3.5B). Upon heating, both

parameters initially show little temperature dependence suggesting most structures stay intact. Rising the temperature to 50 °C and beyond, results in a drastic drop of the concentration of folded structures. At the same time the interhelical peak vanishes completely, which suggests abrupt melting. In order to quantify this melting process, we plot the normalized intensities versus temperature (Figure 3.5C). Both parameters exhibit the typical shape of a melting transition at 53.5 °C.

Interestingly, we do not observe significant thermal expansion prior to melting, that is, the interhelical peak at  $q \sim 0.17 \text{ \AA}^{-1}$  and the dip at  $q \sim 0.05 \text{ \AA}^{-1}$ , which are sensitive to the interhelical distance and origami cylinder radius, respectively, remain at a fixed  $q$  position until the whole structure melts and the intensities vanish. This indicates that thermal fluctuations, for example, Helfrich undulation forces do not play a major role in the force balance. In contrast, the electrostatically induced disassembly exhibited a continuous

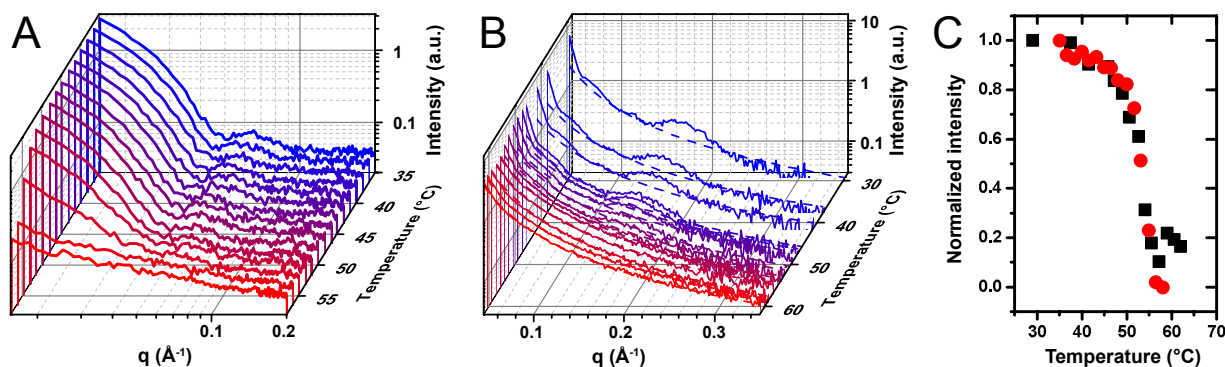


Figure 3.5: In-situ SAXS measurements during melting of 24-helix bundles. (A) Scattering intensities for increasing temperatures (35 to 58 °C) recorded in-house. (B) Background-corrected intensities recorded between 29 and 62 °C at a synchrotron source (ID1@ESRF) to access higher  $q$  values. (C) Normalized intensities at small  $q$  extracted from A (red circles) and helix peak intensities extracted from (B) (black squares) plotted as a function of temperature. Melting occurs at higher temperatures than folding (extracted from Supporting Information Figure 3.6, blue triangles).

lattice expansion at low ionic strengths, indicating that the microscopic mechanism for thermal melting is fundamentally different from electrostatically driven disassembly. These results suggest that the 24-helix bundle should be able to act as rigid framework in the whole physiologically relevant temperature range of up to 50 °C. Both distinct structural transitions provide a critical test for thermodynamic models of DNA origami constructs that take ionic and temperature effects into account.

Along these lines it is remarkable that the melting behavior of the three-layered brick

shows subtle differences when compared to that of the 24-helix bundle. The dip in the sheet scattering curve, which is sensitive to the sheet thickness, vanishes well below the overall melting transition (cf. Supporting Information Figure A.2). This premelting phenomenon could result either from the difference between square (three-layered brick) and hexagonal (24-helix bundle) lattice arrangements or from the different geometries, that is, brick vs rod.

Optimization of the reverse process of melting, that is, folding of DNA into origami structures, is essential for high yield assembly of high quality DNA structures. It has been shown that for certain designs, a specific folding temperature can be determined in fluorescence-based DNA melting assays [119, 120]. Generally, folding is a slow process occurring at lower temperature than melting. Thus, we followed the folding kinetics by cooling the sample down from a molten state and simultaneously monitoring the evolution of the SAXS signal at selected temperatures until the origami folding is completed (also confirmed by TEM imaging and agarose gel analysis, see Supporting Information Figure A.1 and Figure 3.6). Our experiments confirm a clear temperature hysteresis between melting and folding (at 45 °C) for the 24-helix bundle as shown in Figure 3.5C (blue triangles). Note that this type of data acquisition was possible at our in-house source as the underlying processes occur on time scales of hours and information can readily be obtained from the rather high scattering intensities at low  $q$ .

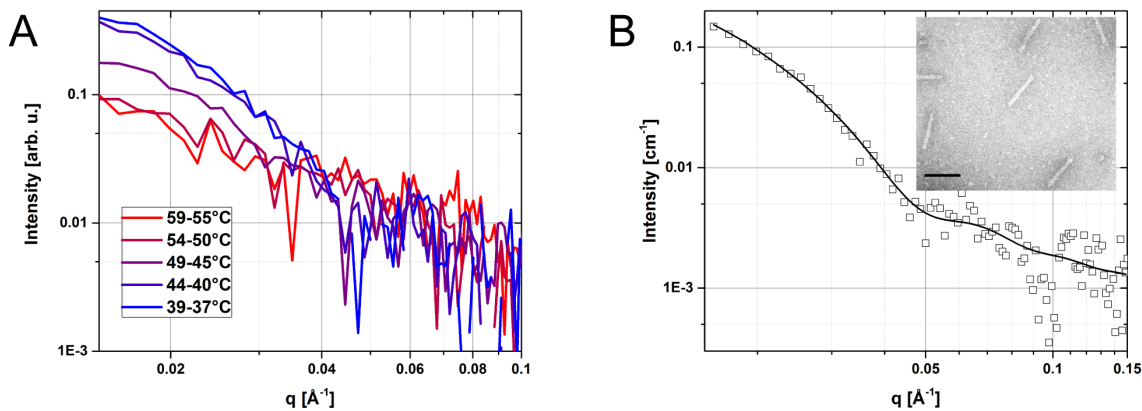


Figure 3.6: (A) Median scattering intensity (30 min integration per degree) without background subtraction for different temperatures during cooling of scaffold and staples of 24HB (B) Five times 2 h measurement of same sample after folding at room temperature with background subtraction, solid line is cylinder plus Debye background fit (inset) TEM image after folding, scale bar is 100 nm.

### 3.2.4 Conclusion

With the field of DNA nanotechnology advancing toward biotechnological, biomedical, and materials applications, accurate structure determination of DNA constructs in varying environments and physiological conditions is essential. Moreover, assembly and disassembly as a function of temperature and ionic strength are at the heart of precise and high yield production of DNA origami. We found that SAXS is a versatile tool to access structural details at the angstrom level surpassing imaging and fluorescence read-out approaches. Importantly, SAXS is an in situ method that provides reliable data without the necessity for labeling or immobilization. We observed swelling of the interhelical distance of up to 10% in response to Mg<sup>2+</sup> depletion, which could in principle be used to transduce ionic strength or pH changes into conformational transitions. Tunable porosity or pH dependent structures may have potential applications for retention and release of drug cargo by DNA-based agents. From a theoretical viewpoint, the finite ionic and zero thermal expansion revealed by SAXS scattering are remarkable and leave room for refined 3D origami models that include thermal melting and electrostatic interactions in various ionic conditions. A better understanding of temperature and ionic effects on DNA origami will help to improve stability issues in complex fluids and potentially allow for purposeful structural switching mechanisms. Recent studies also showed how SAXS measurements can monitor conformational changes of DNA origami switches and obtain timescales on which these processes occur [121, 122]. Furthermore, SAXS was used recently to identify global twist in DNA origami structures [123].



# Chapter 4

## SAXS on DNA mediated gold nanoparticle (AuNP) assemblies<sup>1</sup>

In this chapter I discuss how the arrangement of gold nanoparticles (AuNP) on DNA origami nanostructures can be investigated and tested by SAXS. SAXS as an established tool for characterization of biomacromolecules in solution has also been used in several studies for AuNP constructs [125]. It can be used to determine the distance of AuNP pairs itself or to use the AuNPs as labels for characterization of intramolecular properties and interactions [126, 127, 78]. Both of these applications of SAXS can in principle be useful for AuNP nanoarchitectures mediated by DNA origami: to measure the distance of AuNPs yielding it accessible for optimization and to gather information about linker properties.

---

<sup>1</sup>This chapter is partly based on the publication "*Position Accuracy of Gold Nanoparticles on DNA Origami Structures Studied with Small-angle X-ray Scattering*", Caroline Hartl, Kilian Frank, Heinz Amenitsch, Stefan Fischer, Tim Liedl, Bert Nickel, *Nano Letters*, 18 (2018), 2609-15. doi: 10.1021/acs.nanolett.8b00412. Adapted with permission from [124]. Copyright (2018), American Chemical Society.

(Sections: 4.5-4.5.4, 4.5.6 and corresponding Supplementary Information.)

Author contributions:

C.H., S.F., T.L. and B.N. designed the research. C.H. prepared the assemblies. C.H., K.F., S.F., and B.N. performed the SAXS measurements and analyzed the data. K.F. programmed the models. K.F. and C.H. fitted the data. H.A. obtained the PDDF with the program GIFT. C.H. and K.F. prepared the figures. C.H. wrote the manuscript. All authors edited the manuscript.

## 4.1 Applications of DNA origami templated AuNP architectures

A short overview of DNA origami as promising candidates to serve as templates to arrange metallic nanoparticles into plasmonic devices is given here following the description of ref. [60]. Collective oscillations of conducting electrons in metal nanoparticles upon interaction with light result in particle plasmon resonances. Those plasmon resonances depend on shape, local environment, composition and arrangement of the metal nanoparticles. The coupling of plasmons of metal nanoparticles close to each other is among other things influenced by relative spatial placement of the individual nanoparticles. The DNA origami technique offers the possibility for a precise arrangement of metal nanoparticles and with this provides a path for the creation of plasmonic structures with tailored optical properties and new functionalities. For example, in dimers of metal nanoparticles in close proximity to each other upon incidence of light a hot-spot of strongly enhanced electromagnetic fields is localized in the gap between them. Such constructs can serve as optical antennas. Light sources such as fluorophores can be coupled to the antennas by placement in their hot-spot [128]. The antennas serve for signal enhancement and single-molecule detection [128, 129, 130]. Furthermore, it was shown that a helical arrangement of nanoparticles can create a strong and switchable plasmonic circular dichroism in the visible spectral range [110, 131, 132]. Roller et al. [133] demonstrated DNA origami assembled nanoparticle rings exhibiting electric and magnetic resonances at visible frequencies. DNA origami templated assembly has promoted the fabrication of plasmonic waveguides for energy transfer based on arrays of metal nanoparticles [134, 135, 136].

All these applications require a precise positioning of guest molecules. Thorough characterization of the DNA origami based systems can facilitate modeling and simulations. To verify and optimize the properties of the DNA mediated assemblies, configuration determination by SAXS can be useful.

## 4.2 Distance measurements on AuNP arrangements with SAXS

Distance measurements of gold labels as rulers on macromolecules of interest in solution conditions have been suggested [126]. Gold labels have been used for characterization of molecules, their conformations and interactions [126, 125, 78]. The scattering measure-

ments determine the interference term of the gold labels to obtain the distance [125]. The technique was used to investigate the mechanical properties of DNA [80, 127, 137]. The distance measurements of gold labels were also applied to study the deformation of DNA induced by the MutS protein, which is involved in mismatch repair, in the presence and absence of mismatches in the DNA double strand [138]. Furthermore, it was studied how the number of bridging DNA strands in a DNA linked nanoparticle dimer influences the interparticle separation [139]. It was shown that SAXS measurements can in principle be used to characterize biomolecular interactions [78]. SAXS measurements can provide information not only on nanoparticle distances in DNA origami assemblies but also on the influences of linker properties. This information can be used to tune the structural properties.

### 4.3 Attachment of AuNPs to DNA origami nanostructures

DNA has a long history of being exploited for the creation of metal nanoparticle assemblies [140, 141]. AuNPs and other species of guest particles can be attached via single stranded DNA protruding from the surface of origami nanostructures [142, 55]. AuNPs can be covered with DNA using thiolated single strands. Those DNA strands that can bind to the corresponding complementary sequences on the DNA nanostructure. The DNA coverage is influenced by nanoparticle size and spacer composition and the salt concentration during the coverage procedure [143]. The curvature of its surface and therefore the nanoparticle size can play a role for the maximum amount of DNA that can be attached on the surface [144]. The DNA shell has an influence on the properties of the connection to the Origami structure.

In Figure 4.1 a scheme of the attachment of AuNPs to DNA origami structures is shown. DNA covered AuNPs are mixed in excess with the DNA origami nanostructures that here contain three protrusions as docking strands. The docking strands are selected in a way that they point outward from the surface of the structure. After incubation, the assembled structures are purified via agarose gel electrophoresis (Figure 4.1A). Successful assembly is verified using TEM (Figure 4.1B). Here the final geometry of the nanostructures with SAXS measurements is probed to access the distances of the nanoparticles in the assemblies and to obtain the influence of attachment sites and linker properties.

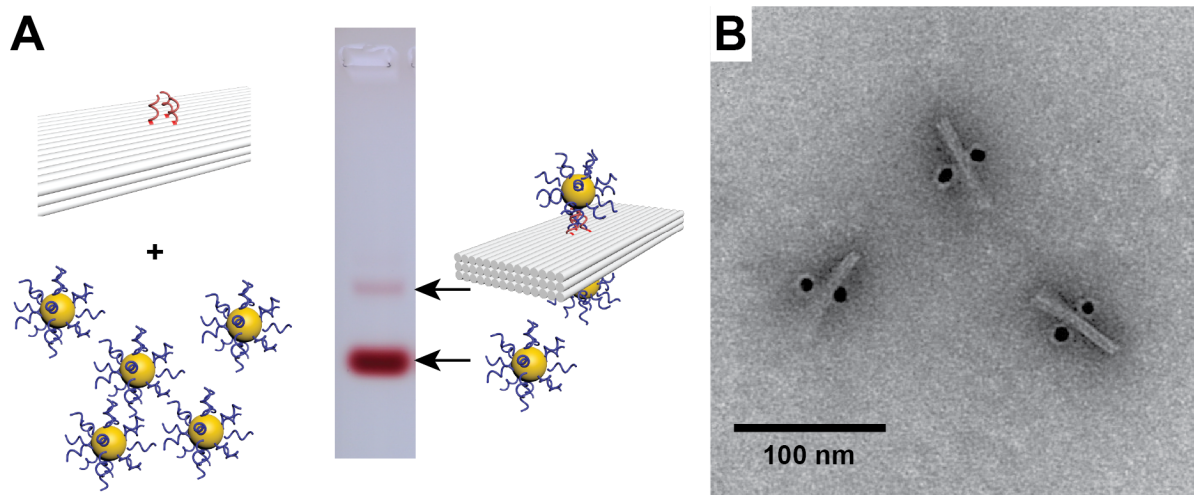


Figure 4.1: Attachment of gold nanoparticles to DNA origami structures. Gold nanoparticles are coated with DNA. Those are mixed with DNA origami that have single strands of a complementary sequence protruding from the surface. The gold is mixed in a five fold excess with the DNA origami nanostructures. After incubation the assembled structures are purified with gel electrophoresis from excess gold nanoparticles. Success of assembly is assessed with TEM.

#### 4.4 Pair density distribution function of AuNP assemblies

The characteristic distances of an assembly are reflected in its pair density distribution function (PDDF). The PDDFs of a given system can be computed or can be simulated by a Monte Carlo approach [98, 145, 146, 147]. Here, I will shortly describe how geometrical parameters of the nanoparticle configurations probed in this study are reflected in its PDDF.

For a sphere of radius  $R=2.5, 5, 10$  nm and dimers of spheres with radius  $R=5$  of distance  $d=20,25,30$  nm the PDDF is shown in Figure 4.2. The PDDF of the spheres shows one maximum (Figure 4.2A). The position of the maximum is related to the size of the spheres. The dimer configurations show two maxima (Figure 4.2B). Differences in the center-to-center distance of the dimers are reflected in the PDDF in differences in the position of the second maximum. It can be seen that with these parameters the second maxima of the PDDF occur in close proximity to the center-to-center distances of the AuNP dimers.

As an example for an assembly with more than two gold nanoparticles here a helix

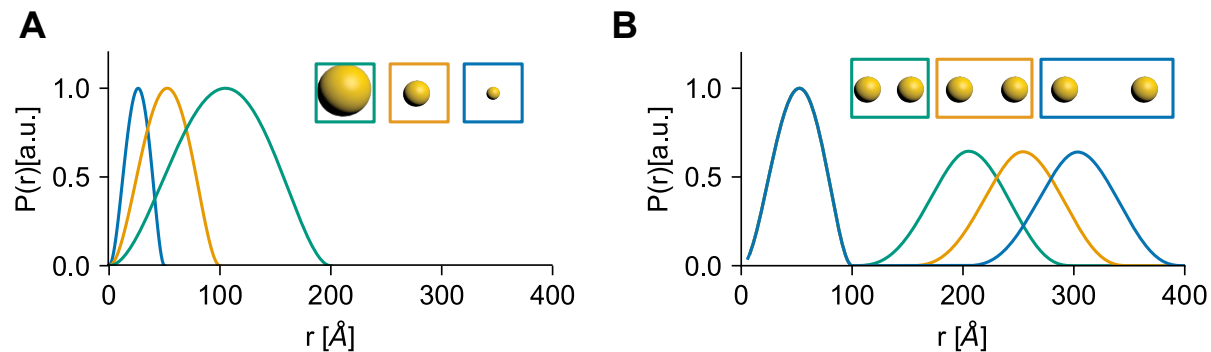


Figure 4.2: Pair density distribution functions (PDDF) of spheres (A) and dimers (B). PDDF of spheres of radius  $R=2.5, 5, 10$  nm and a dimers of spheres of distance  $d=20, 25, 30$  nm for  $R=10$  nm are shown.

formed by AuNPs is considered. A discrete helix has characteristic pair distances. For example, a discrete helix of pitch  $p$  and radius  $R_{helix}$  with nanoparticles at multiples of  $30^\circ$  has characteristic pair distances  $d_n$  calculated by

$$d_n = \sqrt{2 \cdot R_{helix} \cdot \sin 30^\circ \cdot n^2 + \left(\frac{p}{6} \cdot n\right)^2} \quad (4.1)$$

A change in helical pitch would result in shifts of all  $d_n$  to larger values, while a change in radius would leave those  $d_n$  corresponding to particles on the same side of the helix unaffected while increasing those corresponding to opposing parts of the helix the most. Thus, structural changes in radius and pitch are accessible and distinguishable via the pair distances.

## 4.5 SAXS on DNA origami mediated AuNP assemblies

In the project described in this chapter we apply SAXS for structure determination of three prototypical gold decorated DNA origami nanostructures with increasing complexity: a dimer, a trimer, and a helix. AuNP pair distances of dimers and trimers in solution extracted with pair density distribution function (PDDF) analysis are in good agreement with the design estimates. The distances obtained from the PDDF agree with the values extracted from direct modeling of AuNP arrangements within 1.2 nm. We then use the PDDF to analyze design details of positioning of nanoparticles on DNA origami. We find

that the attachment point position on the origami, the choice of the orientation of the DNA connector and the DNA length all influence the positioning. We see indications of repulsion between AuNP placed laterally next to each other, presumably due to their large DNA shell and their flexible connectors to the origami. Furthermore, the radius of a helical arrangement of nine nanoparticles can be obtained from the AuNP pair distances.

#### 4.5.1 SAXS pattern and design scheme

The synchrotron SAXS intensities of the components used in the assembly, namely the origami block and the AuNPs, and their assemblies are shown in Figure 4.3. They are plotted as functions of the magnitude of the scattering vector  $q = 4\pi/\lambda \sin(\theta)$  with wavelength  $\lambda$  and scattering angle  $2\theta$ . The scattering intensities from the bare DNA origami structures, a block and a cylinder shape, are well known from previous measurements [105] (i&ii). The AuNPs show the characteristic oscillations of spherical particles (iii), which allow us to measure their radius from model-based analysis of the scattering curve. At first glance, the scattering intensities from the AuNP dimers largely resemble the scattering of the single unbound AuNPs, since they are the dominating scattering objects in these assemblies due to their high electron density. A closer look, however, reveals characteristic interference effects at small  $q$  (iv), i.e. in the  $q$  range which probes the AuNP nearest pair distances  $d_{NB}$  via  $q = 2\pi/d_{NB}$ . Similarly, the helical AuNP arrangement mediated by the origami cylinder modulates the intensities at small  $q$  (v) (data shifted for clarity).

Before we analyze the SAXS data quantitatively we describe the design scheme in detail in order to define the estimated distance values for the AuNPs in the different constructs. To assemble the dimer, we attached DNA-functionalized gold nanoparticles of nominally 10 nm diameter to three different binding sites on block-shaped, three-layered DNA origami nanostructures [52] (Figure 4.4a). The defined binding sites consist each of three single-stranded DNA extensions, which are protruding from the upper or lower surface of the block (marked red) in a triangular geometry. All protrusions have a length of 15 A-bases while the gold nanoparticles are functionalized with thiol-modified-oligonucleotides of 19 T-bases, which gives a single-stranded spacer of 4 nucleotides (nt), adding a certain degree of flexibility. Two binding sites are located on one side of the block, one at the center (A) and one at the edge (B), and one binding site at the middle of the other side of the block (C), enabling the formation of three different dimer pairs (AB, AC, BC). Attachment sites A and B are laterally displaced by a small and a large shift compared to C, respectively. For clarity, we call these arrangements lateral (AB), vertical (AC), and diagonal (BC).

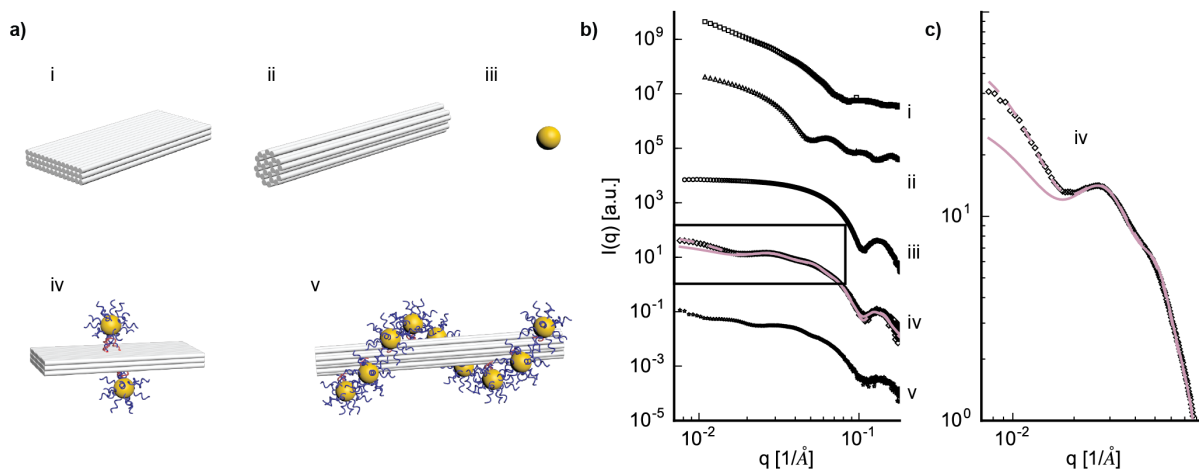


Figure 4.3: Sketches (a) and measured SAXS pattern (b) of the components: i) a three-layered origami block, ii) an origami cylinder of 24 helices, iii) gold nanoparticles of approximately 10 nm diameter, iv) a gold nanoparticle dimer mediated by the DNA origami block, v) and a helical arrangement of nanoparticles mediated by the origami cylinder. Fits are shown for a dimer model considering only the scattering of the gold nanoparticles (solid line) and of a model taking into account the origami block and DNA shells around the particles (iv dashed line) in a zoom-in (c).

The distance between the A and B attachment points of the lateral arrangement corresponds to 63 basepairs (bp), i.e. we expect a AuNP distance of 21.4 nm for the AB dimer, accounting for 0.34 nm per bp [23]. In dimer AC and BC, the attachment sites are on opposing sides of the origami block, and laterally displaced by 4.8 nm and 16.7 nm for AC and BC, respectively (Figure 4.4b). The thickness of the three layer DNA origami block is 7.7 nm [105], while the radius of the AuNPs has been determined from the SAXS data to be 4.2 nm. As a simple estimate we here calculate the connector length of the oligonucleotides binding the AuNP as 5.1 nm accounting for a distance equivalent to 0.34 nm per basepair for 15 bp. With this, we estimate AuNP distances of 27 nm and 31 nm for the vertical (AC) and diagonal (BC) dimer, respectively. Note that these distances are well beyond the standard range of FRET experiments. After we fabricate all three dimers (AB, AC, BC) and the trimer conformation (ABC) we employ TEM imaging (Figure 4.5b) confirming assembly of all four structures (Table 4.1). For distance measurements the TEM images are prescreened for top views and side views of the lateral AB and vertical AC and BC configurations, respectively. The average center-to-center distance for the lateral (AB) configuration is 21 with a standard deviation of 4 nm, which is in good agreement with the designed value of 21.4 nm. For the vertical and diagonal configuration AC and BC we

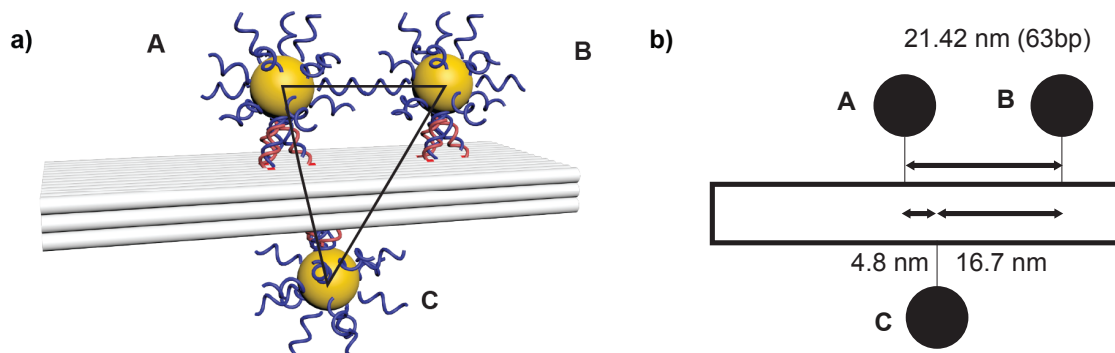


Figure 4.4: Sketch of the trimer ABC with nanoparticles at different attachment sites A, B and C of the origami block.

find values of  $25 \pm 1$  nm and  $27 \pm 2$  nm which are slightly off the design-estimated values of 27 nm and 31 nm. The TEM analysis confirms the successful assembly and gives first estimates on the distances of the AuNPs, but the orientation of the objects when landing and drying effects can have a large influence on the particle configuration on the grids. These drawbacks can be overcome by SAXS measurements in solution. We will see below that center-to-center distances obtained by TEM are systematically smaller than the SAXS values for full hydration conditions.

#### 4.5.2 Direct modeling and PDDF

We first analyze the SAXS data of the dimers as they exhibit the simplest geometry. First we used direct modeling to reproduce the scattering data (Supplementary Information S2 in B). The most basic fit model (solid line in Figure 4.3c (iv)) considered only the superposition of the scattering amplitudes of two gold spheres, displaced by distance  $d$ , which was already sufficient to extract dimer distance values which lie in the expected range (Table 4.1), however some fits did not converge. In order to refine the model, the origami block and the DNA shell of the functionalized AuNPs were included in the explicit modeling (dashed line). Now, AuNP distances could be extracted for all dimers. In the cases where both models converged, the agreement was better than 1 nm, while the full model yielded systematically slightly lower distances (Table 4.1).

Before we turn to the quantitative discussion of the distance values, we use the indirect Fourier transform of the scattering data obtained in a model-free way through the software package GIFT [101]. This software calculates the pair density distribution func-

	AB T <sub>19</sub>	T <sub>8</sub>	3'T <sub>19</sub>	AC T <sub>19</sub>	T <sub>8</sub>	3'T <sub>19</sub>	BC T <sub>19</sub>
Simple model	22.92 ± 0.09	x	x	26.98 ± 0.09	21.29 ± 0.05	22.75 ± 0.08	31 ± 0.2
Extended model	21.93 ± 0.08	19.80 ± 0.05	20.67 ± 0.06	26.22 ± 0.08	20.84 ± 0.05	22.20 ± 0.06	30.8 ± 0.1
GIFT	23.1	21.0	21.6	26.9	21.8	23.1	30.2
GNOM	23.0	20.9	21.6	26.8	21.6	23.2	30.4
TEM	21 ± 4 (69)	20 ± 3 (85)	18 ± 3 (108)	25 ± 1 (31)	20 ± 1 (71)	21 ± 1 (38)	27 ± 2 (10)

Table 4.1: Comparison of the values of the center-to-center distances in nm of the dimeric structures obtained by fitting with the simple model only considering an AuNP dimer, with the extended model additionally considering DNA shells and the DNA block, by reading off the position of the second maximum of the PDDF obtained with GIFT and GNOM, and by TEM image analysis. The number N of structures measured via TEM image analysis is given in brackets. Obtained distances from SAXS data vary no more than 1.2 nm from each other. x indicates datasets where the simple dimer model did not produce sufficient agreement with the data.

tion (PDDF)  $p(r)$ . The PDDF is a histogram of distances  $r$  which can be found inside the scattering object and  $p(r) = r^2\gamma(r)$  with the averaged self-convolution of the density distribution  $\gamma(r) = \langle \rho(\vec{r}) * \rho(-\vec{r}) \rangle$  [83, 77, 84]. The PDDF distribution for a pair of spheres is supposed to show two maxima [98]. The first maximum is determined by the AuNP-sphere radius, the second maximum is determined by the center-to-center distance (Supplementary Note S2).

### 4.5.3 Influence of attachment sites and connector types

We find that all PDDFs of dimers show a second maximum at a different characteristic position for lateral, vertical and diagonal configuration (Figure 4.5, solid line, dashed line, dash-dot line, respectively). For the lateral, vertical, and diagonal configurations, the maxima indicate distances of 23.1 nm, 26.9 nm and 30.2 nm, respectively. These values are in good agreement with the design values. Furthermore, we find that distances obtained from the second maximum position of the PDDF agree within 1.2 nm with the analysis of SAXS intensities by simple geometric shape models and trends are the same. Thus, particle distances can be read off directly from the experimental PDDF (Supplementary Note S2).

With the goal of investigating the influence of DNA design details, we collected SAXS

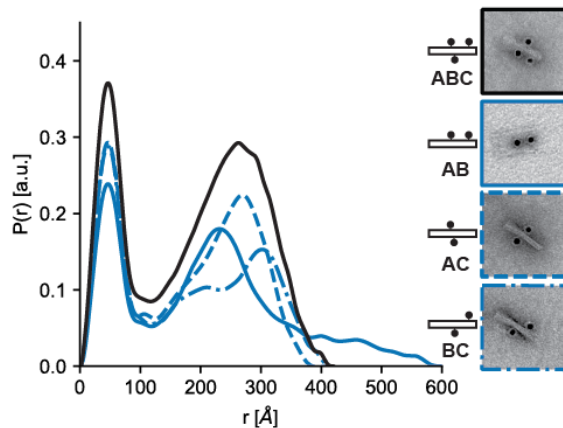


Figure 4.5: PDDF obtained from the scattering of the dimers AB, AC and BC and trimer ABC (blue solid line, dashed line, dash-dot line and black solid line respectively) with nanoparticles at different attachment sites. TEM images of all 3 dimers and the trimer are shown. Positions of the second peak indicate the center-to-center distances of the gold nanoparticles.

intensities of the lateral and vertical dimers (AB & AC) using different connectors (Figure 4.6a). Particle attachment was performed in three different ways. The AuNP were conjugated to (i)  $T_{19}$  with thiol with a 6 carbon spacer at the 5'-end, (ii)  $T_8$  with thiol with a 6 carbon spacer at the 5'-end, and (iii) to  $T_{19}$  with thiol with a 3 carbon spacer at the 3-end (Figure 4.6a)). The origami structures were prepared with protrusions of either  $A_{15}$  or  $A_9$  extending from 3'-ends of 3 designated staple strands to capture the nanoparticles covered with  $T_{19}$  or  $T_8$  strands, respectively. We expect that attachment thus occurs via hybridization and the formation of 3 double strands of 15 and 8 bp in (i) and (ii). The third configuration (iii) is designed to form a 15 bp double strand in a so-called "zipper" configuration [129]. Assembly of the different constructs was first confirmed using TEM (Figure 4.6b & c) followed by detailed SAXS studies.

For the vertical dimers (AC) we find that the second maximum positions indicate the dimer distances, 26.9 nm, 21.8 nm and 23.1 nm for configuration i, ii, and iii, respectively (Figure 4.6b). This can be rationalized by the following geometrical arguments: The observation that the distance in configuration (i) is 5 nm larger than (ii) can be explained by the length difference of the connecting oligonucleotides. The zipper configuration (iii) might be expected to yield the smallest dimer distance by zipping the nanoparticles tightly to the DNA origami surface. One should consider, however, the effect of sterical hindrance by the single-stranded DNA shell, which is 11 nt larger for the zipper configuration (iii)

than for configuration (ii). The sterical hindrance of long oligonucleotides and the T4 single stranded spacer may cause the larger binding distance of the zipper configuration (iii) compared to the  $T_8$  configuration (ii).

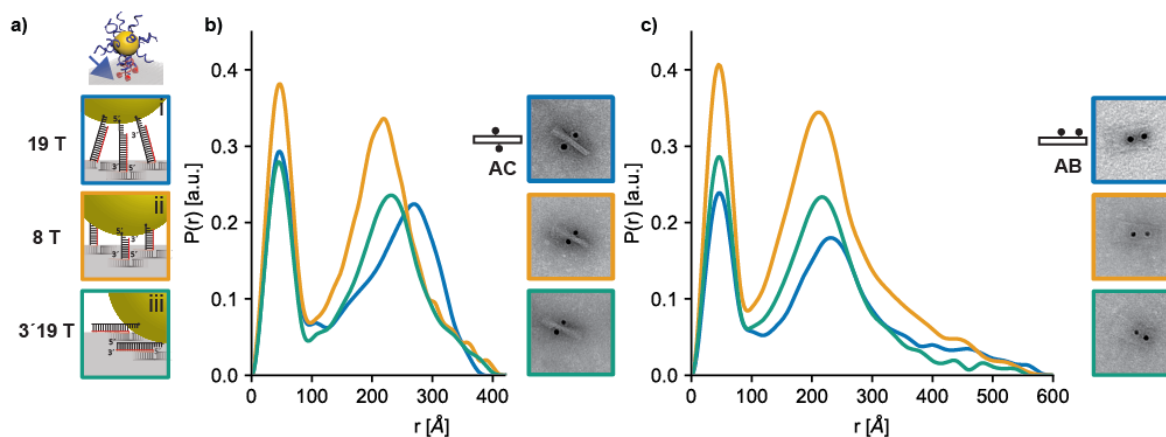


Figure 4.6: a) Scheme of the tested connector types: (i)  $A_{15}$  to  $T_{19}$  (blue), (ii)  $A_9$  to  $T_8$  (orange) and (iii)  $A_{15}$  to  $3'T_{19}$  (green, zipper configuration). b) & c) PDDF for each of the three different connector types for dimers AC (b) and AB (c) are shown together with corresponding TEM images.

For the lateral dimer (AB), we find that the second maximum positions indicating the distances vary slightly for the three connector types: 23.1 nm, 21.0 nm, 21.6 nm for configuration i, ii, and iii, respectively (Figure 4.6c). The measured distances of the lateral AB dimer with the shorter connectors (ii and iii) are close to the calculated attachment point distance of 21.4 nm. The long linker configuration (i) yields a 2 nm larger value for the center-to-center distance. We here want to estimate if at this distance an influence of repulsion due to the DNA-shell on the AuNPs can be expected: Analysis of SAXS measurements of the AuNP functionalized with (i), (ii), and (iii) using a core-shell model as approximation indicate an equal Au core size of 4.2 nm and the largest shell for  $T_{19}$  with the six carbon spacer and the smallest for  $T_8$  as expected (Supplementary Note S2). If the single stranded oligonucleotides covering the surface of the AuNP behaved as ideal polymer random coils, the DNA shells would be of the order of the Flory radius [148] of 4 and 2 nm for  $T_{19}$  and  $T_8$ , respectively. However, as the configuration of oligonucleotides attached with thiol via a carbon spacer on a curved and densely covered surface deviates from this picture, we expect a different behavior. In order to verify for dense particle functionalization with DNA, we performed UV/vis spectroscopy control measurements for selected samples. We find that the number of DNA oligonucleotides, e.g. of 10 nm AuNPs

functionalized with  $T_{19}$ , is on the order of  $\sim 80$  strands per particle, yielding surface densities of  $\sim 0.2$  strands per  $\text{nm}^2$  which is consistent with previously reported values [144]. At high surface densities, DNA is expected to adopt a "brush" configuration with oligonucleotides being stretched away from the surface [149, 150]. Due to the rigid core of the AuNP, the remaining space in between two AuNP sitting next to each other in the AB configuration is only 13 nm. This length corresponds to about 26 nt in a stretched configuration [149]. This implies that the 19 nt -long DNA strands covering the AuNPs would overlap and hence induce steric repulsion, while for AuNPs covered with 8 nt-long DNA no repulsion would be expected. Indeed, we find an enlarged distance for the longest  $T_{19}$  connectors. For the shorter connectors (ii) and (iii) the particle separations are close to the nominal value. We assume that the shorter connector (iii) allows for less movement of the particles away from the attachment point. This explains a lower deviation of the AuNP distance from the attachment point distance due to repulsion in configuration (iii). The trend of larger AuNP distances for  $T_{19}$  (i) compared to  $T_8$  (ii) obtained here in full hydration is also observed for dried samples on TEM grids for the lateral AB as well as for the vertical AC configuration of the dimer.

#### 4.5.4 Helical nanoparticle arrangement

Finally, we turn to the question whether also assemblies with more than two AuNP yield meaningful PDDFs. This question is highly relevant in order to confirm that analysis of AuNP-DNA assemblies with the model-free PDDF is possible by standard data processing based on the indirect Fourier transform. We find that the PDDF of the trimer arrangement is indeed a superposition of the three PDDFs obtained separately for the dimers (see Figure 4.5). A disentanglement of the respective dimer distances is, however, difficult, since all dimer distances (AB, AC, BC) agree within a few nm, i.e. the trimer is similar to an equilateral triangle. We therefore turn to a construct that has more characteristic pair distances; a helical arrangement of nine AuNP attached to a cylinder-like 24 helix bundle origami [110]. The measured PDDF of the helical AuNP arrangement is shown in Figure 4.7a (black solid line). The experimental PDDF shows side maxima at various pair distances in a discrete helix (Figure 4.7b). The first and second side peak at 21.2 nm and 36.4 nm agree with the nearest and next nearest neighbor distances of AuNPs in the discrete helix design, shown in the schematic (Figure 4.7b) as purple and blue lines. With these neighbor distances, it is possible to estimate the radius of the helix to approximately  $R=18.4$  nm assuming a pitch of 57 nm. This value is in good agreement with the design

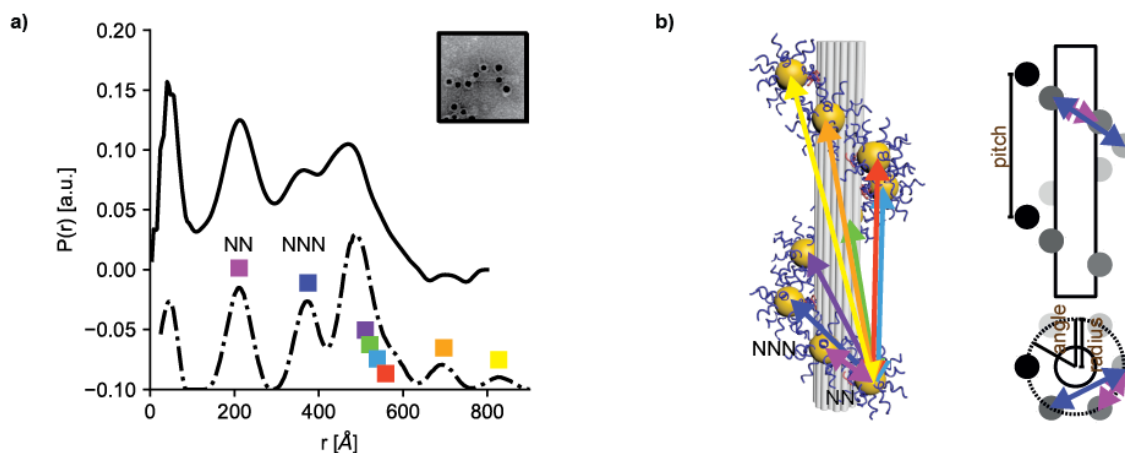


Figure 4.7: a) PDDF of the helical arrangement (solid line) and by Monte Carlo simulation (dash-dot line) (see also Supplementary Note S2). b) The distances (colored arrows in the scheme) occurring in the PDDF (colored squares) confirm a helical arrangement with an overall helical radius of approximately 18.4 nm.

(Supplementary Note S3). At larger distances multiple peaks overlap in the PDDF. Here it is only possible to analyze the PDDF via comparison of the whole function with a simulated PDDF based on our structure model using a Monte Carlo approach (Figure 4.7a, dash-dot line, details can be found in Supplementary Information S2) [146, 145, 151]. The agreement of the experimental PDDF with the simulation is remarkably good considering the complexity of this assembly.

#### 4.5.5 DNA origami assemblies mediating small AuNPs

Within the context of the second project the PDDF of a dimer consisting of gold nanoparticles of a smaller diameter was examined. Gold nanoparticles with a nominal diameter of 5 nm were covered with thiolated oligonucleotides of 19 thymine bases. Those nanoparticles were attached to binding sites on one side of a DNA origami block corresponding to configuration AB, see Figure 4.8a. The binding sites consist of three single stranded protrusions of 15 adenine from the block. SAXS data was recorded for this dimer of 5 nm diameter nanoparticles in the AB configuration.

The program DATGNOM [152] was used to indirectly Fourier transform the data. The obtained PDDF is shown in Figure 4.8b. Two maxima are visible in the PDDF as would be expected for a dimer of nanoparticles in this configuration. The first maximum is expected to be in proximity to the radius of the nanoparticle and the second maximum is

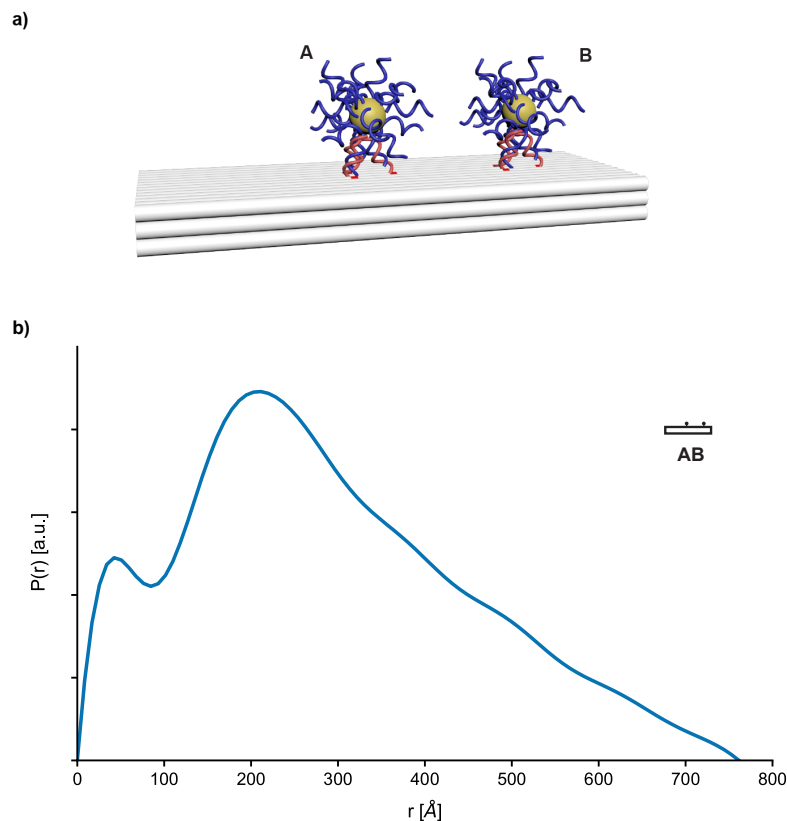


Figure 4.8: (a) Scheme of the DNA origami block carrying gold nanoparticles of nominal diameter of 5 nm. Attachment sites A and B consist of three protrusions of 15 adenine bases each on one side of the DNA origami block. The DNA nanoparticles are covered by DNA strands of 19 thymine bases. (b) PDDF of the shown assembly: Two maxima are observed. The position of the second maximum is found at 21.2 nm. For comparison the distance of the attachment site is 21.4 nm when accounting for 0.34 nm per basepair.

expected to be in close proximity to the center-to-center distance. It is to be noted, that for nanoparticles of 5 nm diameter a shift of the second maximum of the PDDF with respect to the center-to-center distance is expected to be even smaller than for particles of 10 nm diameter. Here the maximum is found at 21.2 nm. The designed value for the center-to-center distance of the gold nanoparticles is 21.4 nm. It is estimated via the distance from the center of one attachment site to the center of the other attachment site accounting for 0.34 nm per base pair. The values are in very good agreement. For dimers of nominally 10 nm the value of 23.1 nm for the peak position of the second maximum was found. This value was larger compared to dimers with gold nanoparticles covered with smaller thiolated oligonucleotides of 8 thymine bases in the AB configuration that gave a maximum position

of 21.0 nm. It was assumed that this difference can stem from repulsion due to a large DNA shell around the particles. Therefore, for the configuration of smaller particles a shorter distance is expected, as is the case for smaller shells. The value of 21.2 nm found for smaller nanoparticles fits in this picture. As scattering intensity scales with scattering length density and volume, for large nanoparticles the contribution of the DNA block and the DNA shell around the particle to the scattering can in some cases be neglected while for small nanoparticles scattering of the DNA might play a larger role. In this experiment, however the position of the second maximum agrees very well with the designed center-to-center distance. Due to a difference in curvature the DNA shell of a particle of 5 nm diameter and with this its connection properties might differ from a nanoparticle of 10 nm diameter [144]. This might be accessed in further SAXS experiments.

#### 4.5.6 Conclusion

Our data shows how SAXS can be used to investigate the placement precision capabilities of DNA origami. While DNA origami itself has fairly predictable spacing properties along the axis of DNA, the attachment of relatively large structures such as the AuNPs of 10 nm diameter used in this study requires multiple attachment strands, which adds further complexity. Here, SAXS measurements can provide distance information within an uncertainty range of 1.2 nm for fine tuning of object positioning by choosing, measuring and adjusting the connectors of the AuNPs to tailor the structures to fit the needs of the experiments. The presented measurements have been performed at a synchrotron facility but initial experiments performed on an in-house setup yielded consistent results. The PDDF analysis is applicable to simple particle systems, which is confirmed by comparison to direct modeling. For many component AuNP-origami objects such as AuNP helices it is possible to extract key design parameters such as the helix radius from characteristic next neighbor distances.



# Chapter 5

## Three dimensional crystalline DNA origami lattices<sup>1</sup>

### 5.1 Programmable materials

The goal of producing novel materials with tailored, programmable properties and responsiveness is a driving force in basic research. Increasing control over the manufacturing of building blocks opens new opportunities and challenges. A generalized approach for crystallization of arbitrary nanoparticles or macromolecules into lattices of predefined symmetries and with predefined lattice constants can pave the way for straightforward production of tailored materials of any type and for a broad range of functions. A scaffolded crystallization system promises to provide a unified solution to differing challenges in crystallization of a wide variety of building blocks such as nanoparticles and proteins of varying interaction properties due to differences in e.g. shape, size and charge. The scaffolding system can be tailored independently and determine lattice properties decoupled from the proper-

---

<sup>1</sup>This chapter is partly based on the publication "*3D DNA Origami Crystals*", Tao Zhang, Caroline Hartl, Kilian Frank, Amelie Heuer-Jungemann, Stefan Fischer, Philipp C. Nickels, Bert Nickel, and Tim Liedl, *Advanced Materials*, 2018, 1800273. doi: 10.1002/adma.201800273. Adapted with permission from [153]. Copyright (2018), WILEY-VCH Verlag GmbH & Co. KGaA, Weinheim.

(Sections: 5.2.1 -5.2.4, 5.2.8 and corresponding Supplementary Information. Adaptions: starting at the second paragraph, Figure 1 replaced by Supplementary Figure S5 and references to Supporting Information removed)

Author Contributions:

T.Z., B.N. and T.L. designed the research. T.Z., P.N., and T.L. designed the DNA structure. T.Z., C.H., A.H.-J. prepared the assemblies. C.H., S.F., K.F., and B.N. performed the SAXS measurements. S.F., K.F., C.H. and B.N. analyzed the SAXS data. T.Z., S.F, K.F., and C.H. prepared the figures. C.H., T.Z., B.N. and T.L. wrote the manuscript. All authors discussed the results and edited the manuscript.

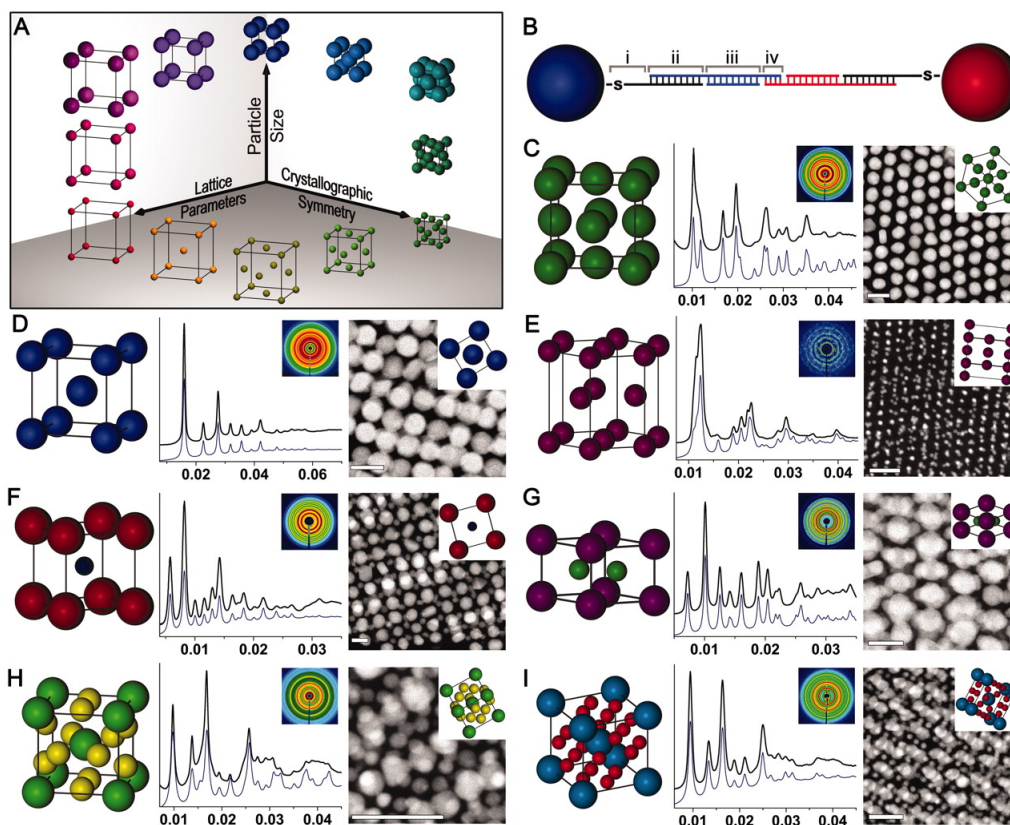


Figure 5.1: Three dimensional lattices based on DNA and AuNPs as building blocks. Tunable design parameters of the lattice, connections of building blocks, assembly schemes, SAXS pattern and structure factors and TEM images with scalebars of 50 nm are shown. From ref. [154]. Reprinted with permission from AAAS.

ties of its components. A promising material for the assembly of a crystallization scaffold system is DNA. The development of DNA nanotechnology was driven by Seeman's idea to overcome challenges in protein crystallization for structure determination using DNA [14]. The method of DNA origami allows to scale the building block unit of a material and with it the lattice constant without compromising the rigidity that is necessary for correct assembly. Furthermore, the properties of DNA origami allow for rational design of building blocks into almost any desired shape. The versatility of this building block's design transfers to the lattice design. In addition, the DNA self-assembly method bears the potential to create materials with tailored properties using guest particles. A robust large open DNA origami crystal holds promises as a framework to host a variety of types of guest particles simultaneously. Many milestones have been reached on the road towards new programmable three dimensional crystalline materials and various materials relying on

DNA for mediation of the interactions of the building blocks have been created promising a wide range of functionalities [155, 156].

For example tailorable strong light-plasmon interactions in 3D crystals have been reported [157] and multicomponent enzyme crystals [158] have been built. When aiming to construct lattices to arrange nano objects two approaches are the use of particles connected to DNA as building blocks [141] and the construction of DNA based systems with the possibility to co-assemble various types of nanoparticles [43, 159, 155]. The first approach for the fabrication of such lattices relies on nanoparticle atom equivalents functionalized with DNA for the mediation of inter particle interactions [141, 140]. Tunable symmetries and lattice parameters of nanoparticles of different sizes based on DNA with long range order have been obtained [154, 160] (Figure 5.1). Making use of the DNA origami technique, more advanced lattices can be fabricated with designed unit cells as for example lattice systems based on polyhedral DNA origami frames connected to AuNPs, even in three dimensions [161, 162, 163].

Another level of intricacy has been added by the creation of lattices that can be switched between phases in response to selected DNA strands [165]. In these crystals both DNA and nanoparticles are lattice defining elements. The second approach relies on stiff DNA motifs [43]. First two dimensional arrangements were based on a double crossover DNA tile that

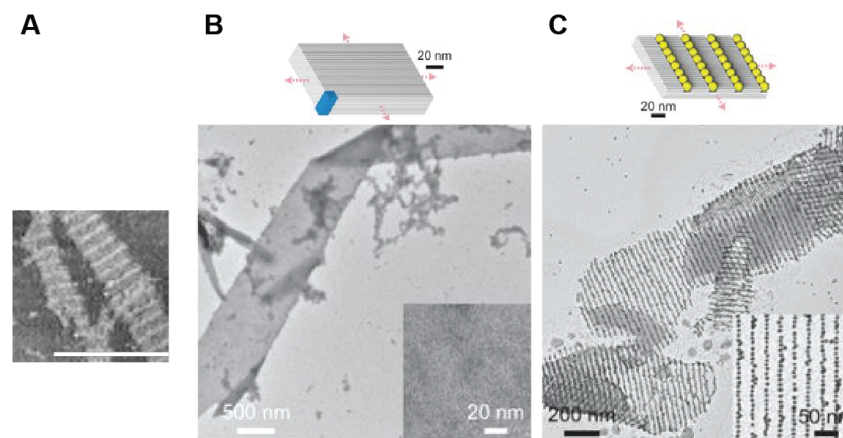


Figure 5.2: Various DNA building block based lattice assemblies. (A) AFM image of 2D-DNA lattices assembled from DNA tiles from ref. [44]. (B) Schematic representation (top) and TEM images (bottom) for crystals of a prescribed depth of 20 layers from ref. [164]. (C) Schematic representation (top) and TEM images (bottom) of parallel lines of 10 nm gold nanoparticles on a crystal from ref. [164]. Reprinted by permission from Springer Nature Customer Service Centre GmbH: Springer Nature, (A) Nature, from ref. [44], copyright (1998); (B,C) Nature chemistry, from ref. [164], copyright (2014).

consists of two antiparallel double helices interconnected twice [44] (Figure 5.2A). Two dimensional lattices have been constructed with the ability to host AuNP of differing sizes [159]. Lattice building blocks exploiting the versatility of DNA origami have been created, for example two dimensional arrays based on DNA origami tiles [166]. A reconfigurable two dimensional lattice built from DNA origami blocks has been constructed which is able to switch between an open and a closed state [49]. Furthermore, membrane assisted growth of DNA origami tile lattices was demonstrated using cholesterol moieties as membrane anchors [167]. Here, the confinement of the building blocks to two dimensions and their orientation on the membrane play an important role for the assembly process. These findings show that DNA building blocks are promising candidates for the mimicking of the operation of specific proteins in the cellular membrane. Moreover, a robot arm rotary device was placed within a two dimensional lattice [168]. The shown operability of the rotatory nano devices in a well defined reference frame is a promising step in nanorobotics. Extending assembly to the third dimension, DNA bricks with the ability to assemble into lattices with a prescribed depth that are able to host guest particles have been obtained [164] (Figure 5.2B,C).

The group of Ned Seeman constructed the first self-assembled three dimensional crystal made purely from DNA [46]. The impressiveness of this example of a bridge of the molecule level with the macroscopic world can be grasped by admiration of the optical image of this self-assembled DNA crystal seen in Figure 5.3A [46]. A close look reveals that its rhombohedral shape is visible. To allow for the incorporation of large guest particles such as proteins into the lattice, crystals of larger cavity sizes are required. For the construction of lattices of large cavity sizes an important factor to be considered is the rigidity of the building blocks. Altogether, DNA nanotechnology offers a promising path towards further applications.

## 5.2 Three dimensional crystalline DNA origami lattices

The goal of the work presented in this chapter is to build a crystal that is made purely from DNA and has a large cavity and thus can serve as a scaffolding construct for large guest molecules [153]. My colleague Tao Zhang designed a triangular building block inspired by the Seeman-crystal [46] shown in Figure 5.3A, B. The building block is about one order of magnitude larger and can thus serve as a building block for a lattice system able to host

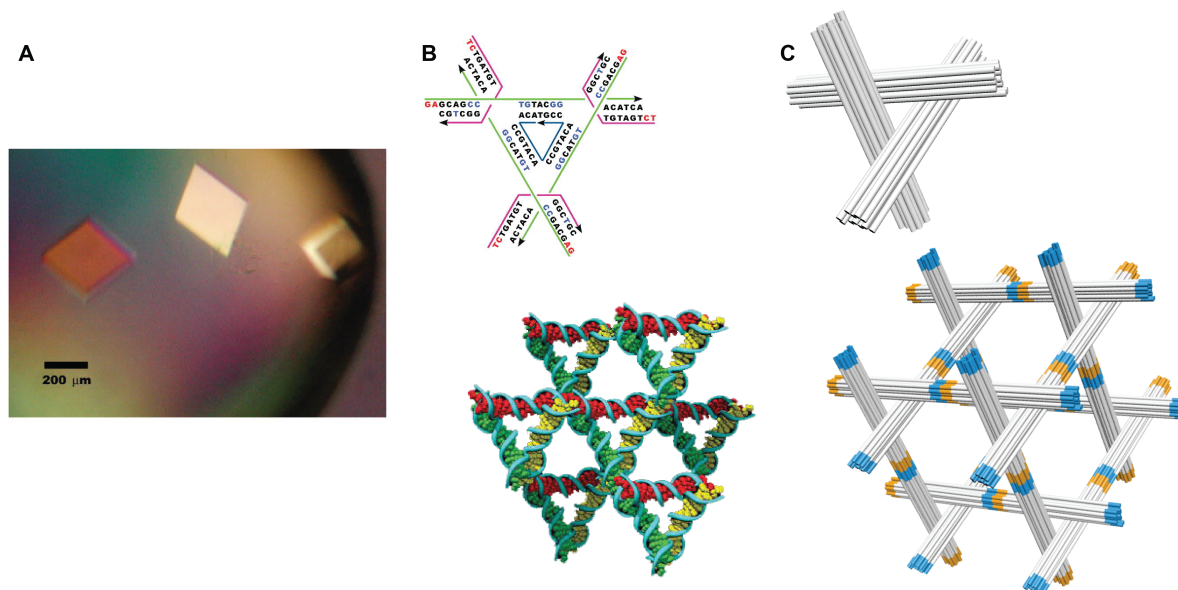


Figure 5.3: (A) optical image of DNA crystals built from a triangular DNA motif [46]. The rhombohedral shape of the crystals is visible. (B) Schematic of the triangular DNA building block and its surroundings [46]. (C) DNA origami building block triangular motif inspired by the Seeman-crystal and its surroundings. (A, B) Reprinted by permission from Springer Nature Customer Service Centre GmbH: Springer Nature, Nature, from ref. [46], copyright (2009); (C) Reprinted with permission from [153]. Copyright (2018), WILEY-VCH Verlag GmbH & Co. KGaA, Weinheim.

large guest particles (Figure 5.3C). It is based on the DNA origami technique. A careful optimization ensured the monomers rigidity, improved symmetry and a correct assembly. The polymerization of the monomer into a three dimensional lattice is induced by the addition of polymerization oligonucleotides that cause the formation of so called "blunt ends" in the monomer structure. These "blunt ends" in turn lead to stacking interactions that lead to lattice formation. We showed that this three dimensional lattice purely made from DNA can host gold nanoparticles of 10 nm and 20 nm diameter. We performed SAXS measurements of all three lattice assemblies. The SAXS measurements determined the dimensions of the lattice in solution to be in agreement with the design. The optimal annealing temperature was found to be just below the temperature up to which the lattice is stable.

### 5.2.1 Triangular DNA origami building block

For our purposes, the DNA origami building block must bear the following features: 1) high structural rigidity, 2) polymerizability along three axes in space, and 3) long edges to provide a large unit cell volume to host guest particles. Thus, inspired by earlier work by Seeman, Mao, and co-workers [46, 45, 169], we built a large "tensegrity triangle" motif with DNA origami (Figure 5.4) [66]. This motif gains uniform rigidity from the intrinsic triangulation and its equally shaped three struts that are arranged in an over-under, over-under, over-under fashion. All of the three struts are 14-helix bundles (14 HB) with a designed length of 67 nm and a diameter of  $\approx 12.5$  nm. The three struts are folded from a single-stranded phage-derived scaffolding DNA (8634 nt) together with 235 synthetic

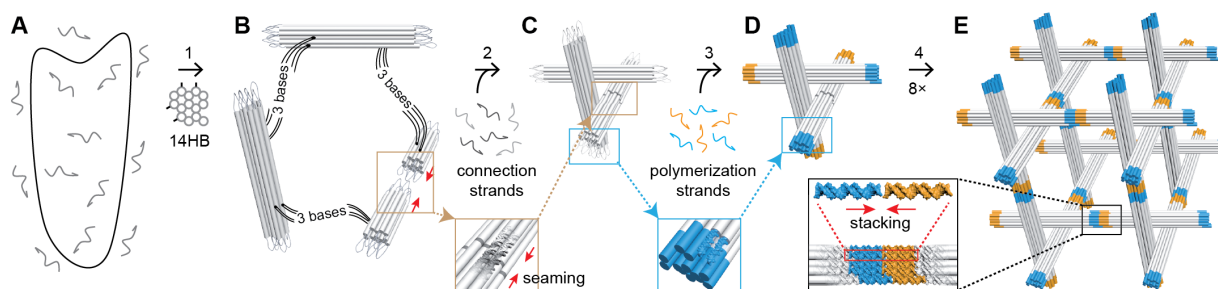


Figure 5.4: Structural details of the triangular DNA origami design and the sequential workflow towards DNA origami lattices. A) The circular scaffold strand and the core staple strands (without connection oligonucleotides and polymerization oligonucleotides) are annealed in step 1 to form the three 14-helix bundles (14HBs) of the triangular DNA structure. The resulting honeycomb design of the 14HBs and the positions where the scaffold crosses over between the struts (black lines) are shown in the cross section image. B) Schematic of the 3 nucleotide-long scaffold spacers connecting the three 14HBs. The selected connection positions and the shortness of the scaffold loops results in a structurally self-restricting origami triangle structure. The inset depicts the scaffold seam in one of the 14HBs. This seam is closed in step 2 by the addition of connection strands during the folding cycle. This two-step process favors correct geometries (over-under, over-under arrangement) over misconnected triangles. C) Correctly folded DNA origami monomer. The addition of polymerization strand in step 3 result in the completion of the struts ends and the formation of dsDNA blunt ends (inset). D) As the DNA origami monomer displays a three-fold symmetry, any blue end can interact with any orange end (inset). Thus the blunt end stacking of the shape complementary ends leads to polymerization of the monomers in three out-of-plane directions and to the growth of a rhombohedral lattice (step 4). E) The resulting unit cell shares eight triangular DNA origami monomers. Reprinted with permission from [153]. Copyright (2018), WILEY-VCH Verlag GmbH & Co. KGaA, Weinheim.

oligonucleotides in a temperature annealing ramp from 65 to 4 °C. Scaffold crossovers interconnect all struts in an over-under fashion predetermining the orientation of each bundle toward one another. One of the 14 HBs contains a "seam" where the scaffold strand does not continue through the entire bundle but is closed by oligonucleotides only (inset in Figure 5.4). By choosing identical cross section, axial orientation, and staggering of the three struts, the origami monomer can polymerize via blunt-end stacking into a rhombohedral lattice with the unit cell parameters  $a = b = c = 67$  nm and  $\alpha = \beta = \gamma = 106^\circ \pm 4^\circ$  ( $\neq 90^\circ$ , the three nucleotide long spacer between each of the 14 HB struts gives rise to flexibility at the joints and results in the uncertainty for the angles  $\alpha$ ,  $\beta$ , and  $\gamma$ ) (Figure 5.4). Note that all three upper ends (blue) match all lower ends (orange) with similar interaction strength which enables the monomers to be incorporated into the crystal in three different orientations due to their three-fold rotational symmetry (Figure 5.4).

First, the monomeric DNA origami structures were thermally annealed starting at 65 °C (for experimental details see appendix C). To avoid kinetic trapping of the struts in an undesired conformation, the oligonucleotides connecting the seam (Figure 5.4) were injected only midway through the folding process at 52 °C to improve the folding efficiency of monomers. The folded triangles were purified from excess oligonucleotides by polyethylene glycol (PEG) precipitation before analysis by transmission electron microscopy (TEM) imaging and polymerization (Figure 5.5A). Note that due to their structural similarity, misfolded structures (Figure 5.5A asterisk) could not be removed from correctly folded structures during the purification step and thus remained in solution during crystal growth.

### 5.2.2 Lattice assembly

To initiate the growth of the 3D lattices, "polymerization strands" were added in a tenfold molar excess over the purified monomers. These oligonucleotides completed the formation of each of the ends of the struts and thus established shape complementary blunt ends. The sample mix was incubated at a constant temperature of 47 °C for 90 h and then deposited and dried on TEM grids. TEM and SEM (scanning electron microscopy) images of origami lattices show the surface-morphology of a regular, hexagonal pattern with a center-to-center spacing between the monomers of 64 nm, which deviates slightly from the designed strut length of 67 nm and reflects the fact that helices in a DNA origami structure are not perfectly straight but undulate in a chicken-wire geometry effectively shortening the struts (Figure 5.5B-F). Close-up views display multiple layers of the lattice (Figure 5.5E). Due

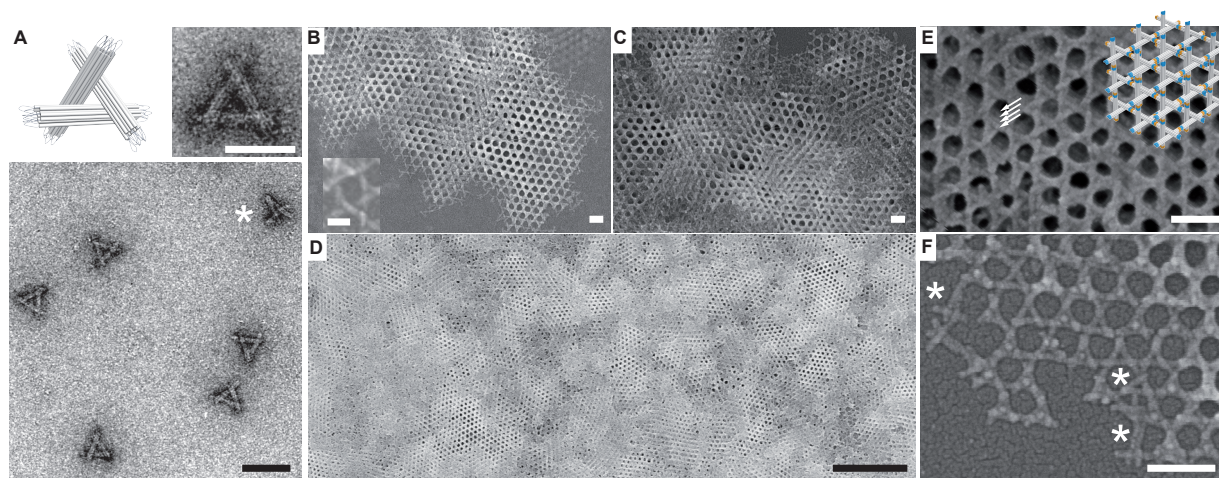


Figure 5.5: DNA origami lattices. A) TEM images of purified triangular DNA origami structures after purification and before addition of polymerization oligonucleotides that would initiate lattice growth. The asterisk points out a defective monomer. B-F) SEM images of DNA origami lattices. The inset in panel (B) exemplifies the left-handed over-under design. Panel (C) reveals the 3D of the assemblies and their polycrystallinity becomes apparent in the wide-field view shown in panel (D). Although the lattices collapse on the imaging substrates during drying, the multiple layers and the original geometry can be inferred in a magnified view (white arrows, panel (E)). F) SEM image showing the border of a lattice with asterisks indicating defective monomers that were expelled from the lattice during the growth process and can only bind later at lower temperatures to the periphery. Scale bars in (A-F): 100 nm, (D): 1  $\mu\text{m}$ , insets in (A) and (B): 50 nm. Reprinted with permission from [153]. Copyright (2018), WILEY-VCH Verlag GmbH & Co. KGaA, Weinheim.

to the obtuse interaxial angle of the building blocks, the lateral extensions along the [111] plane exceed those of all other planes. Consequently we predominantly observe hexagonal patterns corresponding to a top view perspective of the [111] plane. The magnified inset of the building blocks shown in Figure 5.5B confirms the correct chiral over-under orientation of the struts. Low magnification SEM images reveal the polycrystalline nature of lattice patches that are tens of micrometers in size with single domains spanning up to about 2.5  $\mu\text{m}^2$  (Figure 5.5D). Of particular interest is the observation that although defective triangles are present during the growth process, they seem to not incorporate themselves into the lattice patches but only appear in the periphery of the crystals (Figure 5.5F). We rationalize that, as the defective monomers lack the designed symmetry, their overall binding energy does not suffice to stabilize their integration into the lattice at the elevated temperatures during lattice growth. Correctly folded monomers, instead, can replace the

defective ones, which permits the self-healing growth of the origami lattices. After growth and at ambient temperatures, however, defective monomers can bind to any border of the lattice with just one or two connecting sites. Given the limited yield of correctly folded monomers, the observed assembly of macroscopic origami lattices indicates the effectiveness of the self-correcting processes and an overall robust lattice growth.

### 5.2.3 DNA origami lattices hosting guest particles

To demonstrate the precise placement of guest molecules in our origami lattices, we attached gold nanoparticles (AuNPs) of different sizes at the center of each triangular origami monomer (Figure 5.6A). This choice of position preserves the symmetry upon incorporation in the lattice and therefore maintains the rhombohedral lattice type. The particle-bearing building blocks were prepared and purified as described elsewhere [170]. Consecutive lattice growth occurred under equal conditions as for the pure DNA origami lattices. Figure 5.6B shows again the hexagonal pattern formed by origami triangles but this time with 10 nm or 20 nm AuNP groupings at the positions expected in this lattice orienta-

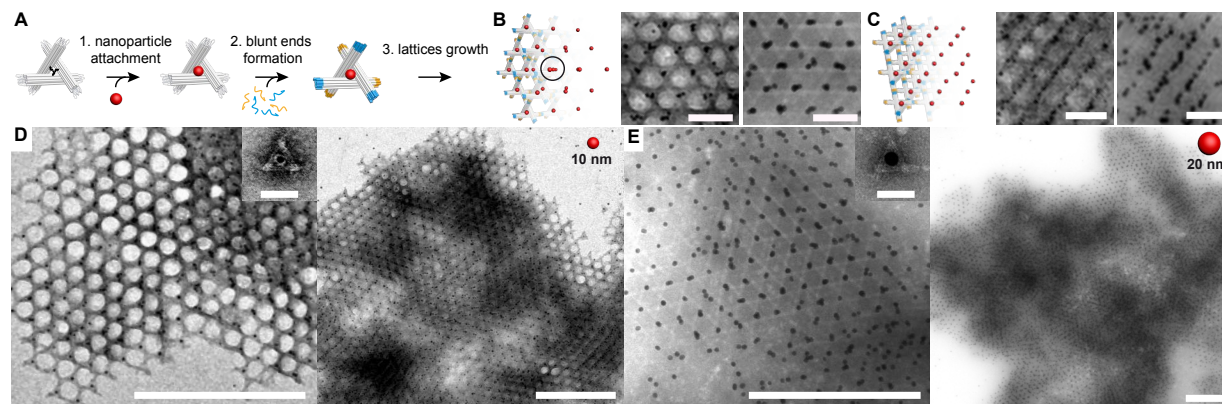


Figure 5.6: Hosting of gold nanoparticles in DNA origami lattices. A) Workflow to prepare gold nanoparticle lattices: 1) Folded and purified DNA origami triangles are incubated with gold particles overnight and then purified from excess particles. 2) Addition of the polymerization oligonucleotides to initiate the lattice growth process. 3) Incubation at 47 °C for 3-4 d yields assembled host-guest lattices. B, C) Model views and TEM images of DNA origami lattice hosting 10 (left) or 20 nm (right) gold nanoparticles. The number of particles per grouping indicates the number of lattice layers overlapping at the respective points (black circle in (B)). D,E) Wide-field TEM images of origami lattices hosting 10 nm (D) and 20 nm (E) gold nanoparticles. Scale bars in (B) and (C): 100 nm; (D) and (E) 500 nm, insets: 50 nm. Reprinted with permission from [153]. Copyright (2018), WILEY-VCH Verlag GmbH & Co. KGaA, Weinheim.

tion. As AuNPs are nearly vertically overlaid when looking down on the [111] plane, the number of nanoparticles per group actually indicates the number of origami layers in the lattice. Due to the strong electron scattering properties of the AuNPs, only a limited penetration depth into the dense samples can be achieved and perfect hexagonal patterns can be observed for not more than a few lattice layers (Figure 5.6E). A different type of nanoparticle pattern - rows of particles - emerged from adsorption of the same lattice in an orientation different from the [111] plane (Figure 5.6C), resulting in a different viewpoint. Low magnification TEM images illustrate the high quality of the particle-hosting lattices (Figure 5.6D). Note that in solution there is no plasmonic coupling between AuNPs as the distance between the particles is too large.

#### 5.2.4 Small angle X-ray scattering pattern of DNA origami lattices

In order to access the full 3D crystal structure of our constructs in solution, we performed small-angle X-ray scattering (SAXS) measurements on the triangular origami monomers, the pure origami lattices, and origami lattices hosting AuNPs. The X-ray intensities for all samples, extracted structure factors, and different model fits are shown in Figure 5.7.

From the scattering data of the monomeric DNA origami building block (dataset i in Figure 5.7A), we obtain a strut length of  $l = 64$  nm, strut radius of  $r = 6.3$  nm, and an angle of  $\alpha = 109^\circ$  in very good agreement with the monomer design [105]. In the absence of "polymerization strands", the monomers are freely dispersed and we see no indication of assembly into any structure of higher order (dataset i in Figure 5.7B). This is very different for the origami crystals (dataset ii in Figure 5.7A) where pronounced Bragg peaks can be observed. The intensity distribution of DNA origami lattices can be modeled by the product of the monomer form factor  $P(q)$ , and  $S(q)$ , the lattice structure factor [90]. In the fitting procedure, we allowed for variation of the interaxial angle, i.e., deformation of the monomer in the assembly process. The best fit confirmed that the geometry was not distorted ( $a = l = 65$  nm,  $r = 6.3$  nm,  $\alpha = 110^\circ$ ) and the resulting lattice is rhombohedral. The measured unit cell of our pure DNA lattice was found to have a volume of  $\approx 1.83 \cdot 10^5$  nm<sup>3</sup>, which is about 100 times larger than that of previously reported pure DNA crystals [46].

SAXS temperature studies revealed a sigmoidal curve, which is characteristic for cooperative effects and indicates the disintegration of the lattice at  $\approx 50$  °C, just above the temperature that we found to yield best crystal growth (Figure 5.7). Interestingly, no

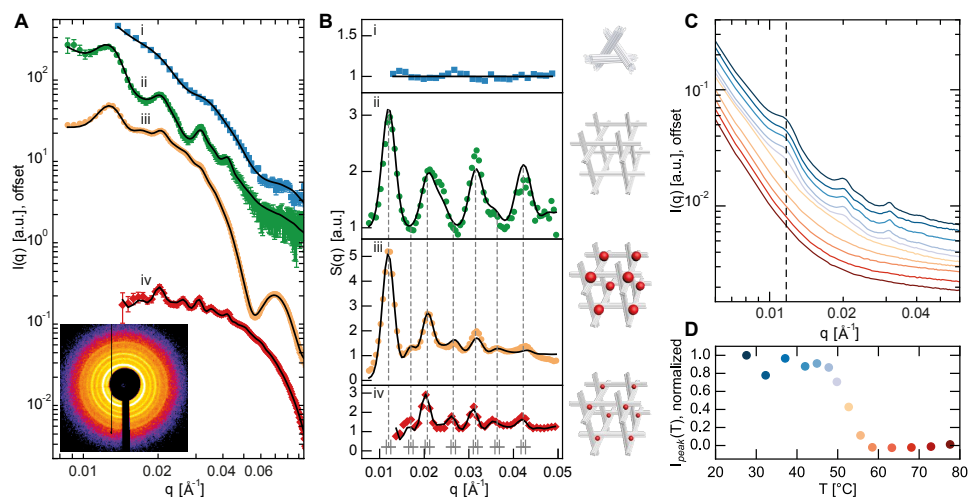


Figure 5.7: Small-angle X-ray scattering (SAXS) measurements on the triangular origami monomers, pure origami lattices, lattices hosting gold nanoparticles, and the in situ SAXS monitoring of lattice melting. A) SAXS intensities of triangular DNA origami monomers (i, blue), origami lattices (ii, green), and origami lattices hosting 20 nm (iii, orange), and 10 nm (iv, red) gold nanoparticles as a function of scattering vector  $q$ . Solid black lines: model fits of total intensity. Inset: SAXS pattern of 10 nm gold-decorated sample. B) The monomer SAXS intensity (i, blue) divided by the fit yields a constant, indicating the absence of a lattice. Lattice structure factors from SAXS data (ii, green, iii, orange, iv red) Squared datapoints: in-house setup, dots: Elettra SAXS beamline, diamonds: DESY P08. Black lines: model fits assuming a rhombohedral unit cell (parameters in the text). Vertical dashed lines label selected Bragg peaks found at the same position in all structure factors. The error range of the instrumental  $q$  resolution of each peak is  $1 \times 10^{-3} \text{ \AA}^{-1}$ . The differences in peak width and  $q$  range stem from the use of different beamlines (DESY P08 and Elettra SAXS). Data in (A) scaled for clarity. Reprinted with permission from [153]. Copyright (2018), WILEY-VCH Verlag GmbH & Co. KGaA, Weinheim.

expansion of the lattice appears prior to melting, i.e., the Bragg peak positions remain fixed until the peaks finally disappear, which is in accordance with our previous findings that DNA origami structures do not exhibit thermal expansion [105].

For DNA origami lattices hosting AuNPs, the crystal structures of the generated AuNP lattices are determined by the DNA origami lattice templates and the nanoparticle placement as described above. For both 10 and 20 nm AuNP lattices, the Bragg peaks resemble each other (vertical dashed lines in Figure 5.7B datasets iii and iv) indicating the same 3D lattice. SAXS intensities of Au-DNA lattices are dominated by the form factor of the AuNPs and contain their coherent diffraction (Figure 5.7A datasets iii and iv). Importantly, we observed a precise correspondence between the unit cell parameters of pure

origami and AuNP lattices, validating the experimental design of templated assembly in 3D by DNA frameworks.

### 5.2.5 Melting of lattices at high temperatures

Within the context of this project we recorded additional data about stability and assembly properties of the lattices, see also [153, 147]. Scattering data of the pure lattices and lattices with gold nanoparticle guest particles of 10 nm and 20 nm diameter during exposure to increasing temperatures was recorded in order to access possible differences in stability. Furthermore, scattering data during the polymerization process in different temperature conditions to test possibilities for monitoring and optimization of lattice growth was collected.

Pure DNA origami lattices, lattices hosting 10 nm and 20 nm gold nanoparticles were monitored during the exposure to increasing temperatures during the course of about 1 hour. The temperature was increased from 28 ° C to 68 ° C. Scattering data was recorded at temperature steps of 2-5 ° C.

Figure 5.8A shows intensity plots of all three lattices during this procedure. The data is shifted for clarity and shown without background subtraction. For all lattices peaks are clearly visible at 28 ° C. The Presence of peaks is maintained up to a certain temperature. Peaks decrease at higher temperatures. At elevated temperatures features have disappeared. For the pure lattices peaks became less pronounced but have not completely vanished at 50 ° C and have disappeared at 53 ° C [153]. The position of the first peak is indicated by a line. The normalized intensity at the position of the first peak is shown in 5.8B. For pure lattices, it stays approximately constant up to 45 ° C and then starts to lower at 48 ° C. At the temperature of 56 ° C the normalized intensity has dropped to zero. The midpoint of the melting curve is at about 53 ° C. For comparison the melting temperatures for a block shaped and a cylindrical DNA origami structure have been determined to be 53 ° C [105]. If the triangular DNA origami structure has a similar melting curve, this means that disintegration of the lattice occurs with the disintegration of the building blocks. The optimized polymerization temperature of pure DNA origami lattices was determined to be at 47 ° C, i.e. it lies slightly below the melting temperature. For 10 nm AuNP lattices a first look at intensity profiles reveals a disappearance of the peak features at 50 ° C. The normalized intensity at the position of the first peak is reduced at the temperature steps between 37 ° C and 48 ° C before it abruptly drops to zero at temperatures of 50 ° C and higher. For 20 nm gold nanoparticle lattices an overall decrease

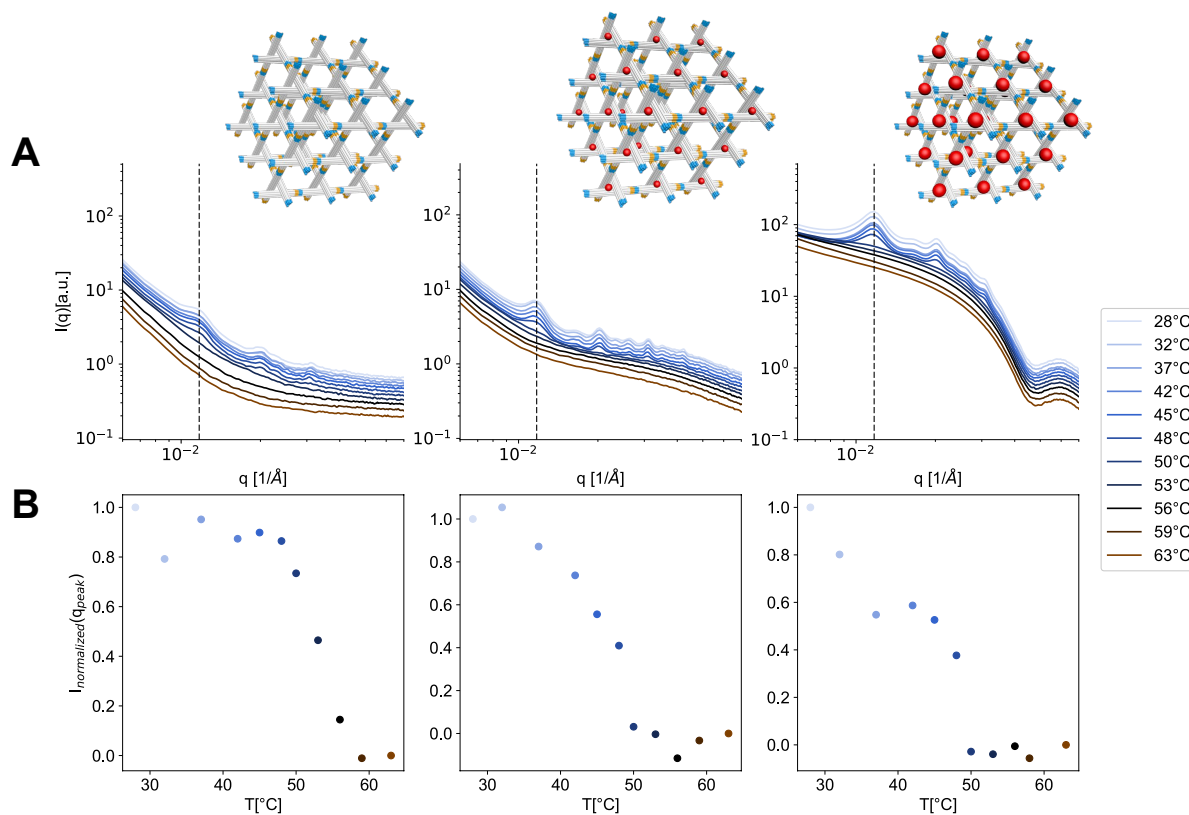


Figure 5.8: Disintegration of DNA origami lattices upon exposure to increasing temperatures, see also [153, 147]: Scattering data of pure DNA origami lattices, lattices hosting 10 nm and 20 nm gold nanoparticles during the exposure to increasing temperatures from 28 ° C to 68 ° in the course of about 1 hour. The data is shifted for clarity and shown without background subtraction.

of the normalized intensity at the position of the first peak during the temperature steps between 37 °C and 48 °C before the abrupt drop to zero at 50 °C is observed as well. In summary, the disappearance of peak features carrying gold nanoparticles occurs at slightly lower temperatures compared to pure DNA origami lattices and a decrease in the normalized intensity is observed before disappearance of the peak features. While polymerization of building blocks is done at an optimized temperature of 47 °C, building blocks carrying gold nanoparticles are polymerized at a temperature of 45 °C. Melting temperatures for both pure DNA origami lattices and lattices carrying guest nanoparticles were determined to be slightly above the polymerization temperatures of the corresponding lattices. It is assumed that this choice of polymerization temperature facilitated lattice growth. A decrease

of peak intensity of gold nanoparticle DNA origami lattices during exposure to increasing temperatures can in principle stem from disassembly of the building blocks of the lattice or from a detachment of the gold nanoparticles from the lattices. Furthermore, a decrease of peak intensity would be expected if lattice patches sediment and therefore disappear from the illuminated sample volume. It is assumed that sedimentation is possibly stronger for lattices hosting guest particles and especially for larger nanoparticles.

### 5.2.6 Polymerization process of DNA origami building blocks

In addition to monitoring the disassembly of the lattices upon exposure to high temperatures, the polymerization process of pre-assembled monomers by intermittent SAXS measurements was investigated. Two samples were measured with one sample being incubated at room temperature and one at the optimized polymerization temperature of 47 °C. Assembled monomers were mixed with polymerization strands and left at room temperature. After 1 day the first measurement was taken. One sample was heated to 47 °C and in the following kept at this temperature, while the other sample was kept at room temperature. Multiple SAXS measurements were taken of both samples within the course of 15 hours. In Figure 5.9 scattering data before start of the incubation of the first sample and after incubation start over several hours for both the sample incubated at the optimized polymerization temperature of 47 °C (Figure 5.9A) and the sample incubated at room temperature (Figure 5.9B) are shown.

For comparison pre-assembled lattices of DNA origami building blocks are shown (black line). Considering the possibility of sedimentation of assembled lattice patches, capillaries were shaken after 4 hours before each measurement to resuspend possibly sedimented structures to move them back into the beam path. For shaken samples peaks are visible. It is assumed that polymerization might have taken place already during the pre-incubation but was not observed due to sedimentation. A comparison of the agitated samples for the incubation at 47 °C and room temperatures shows that peaks are less pronounced for samples that are subjected to room temperature compared to samples subjected to 47 °C. However, no clear trend of peak intensity with time is visible. A reason might be that only a short time interval, compared to the usual polymerization process of 90 hours, was monitored and that changes in beam intensity occurred during the measurement time. In these experiments sample volumes were as low as 30  $\mu\text{l}$ . It is assumed that the total amount of building blocks can play a role considering a possible accumulation of building blocks in the sedimentation area. The issues that the assembly process usually takes 90

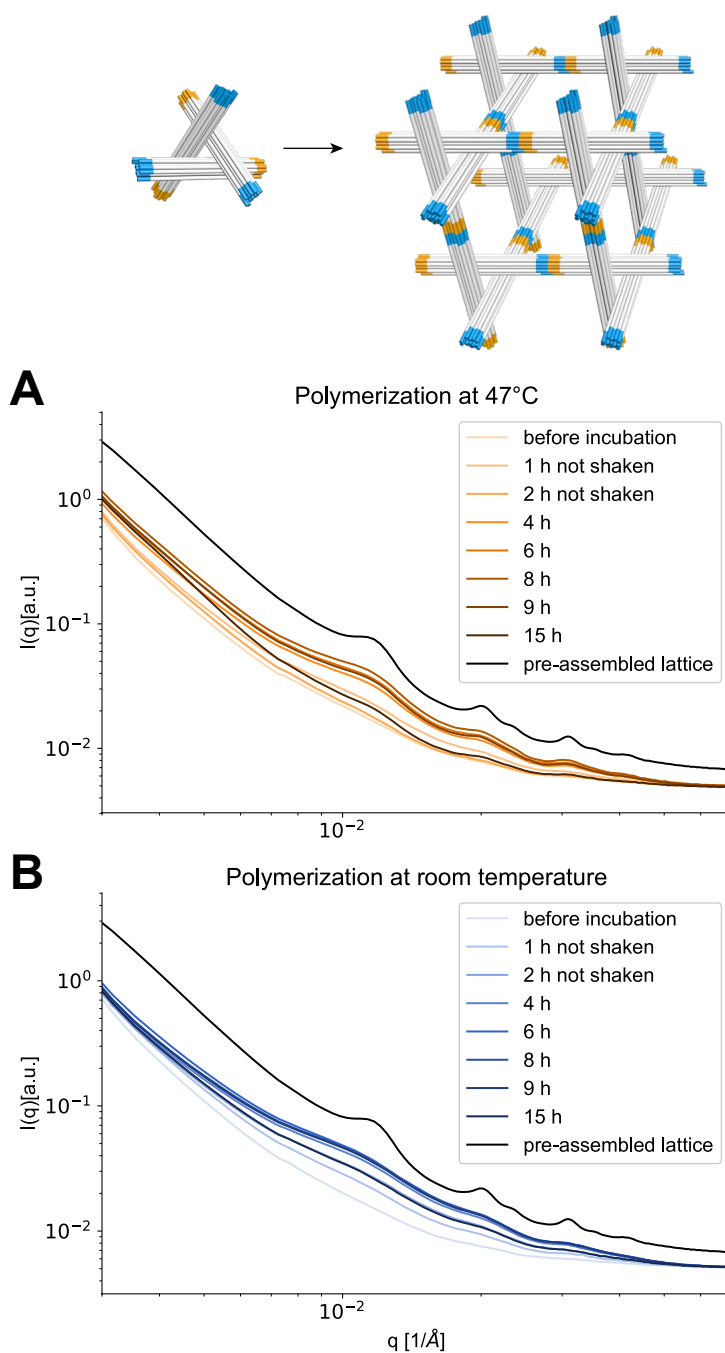


Figure 5.9: Polymerization of DNA origami lattices, see also [147]: Scattering data before start of the incubation of the first sample and after incubation start over several hours for both the sample incubated at the optimized polymerization temperature of 47 °C (A) and the sample incubated at room temperature (B) are shown. For comparison scattering data of pre-assembled lattices is plotted.

hours, a possible occurrence of sedimentation of lattices and with this a possible influence of sample volume, recording the beam intensity should be considered for future measurements to access the possibility of monitoring and optimization of the polymerization process.

### 5.2.7 Building blocks with multiple guest particles

To explore the versatility of the DNA origami lattice, building blocks with multiple gold nanoparticles were designed and assembled.

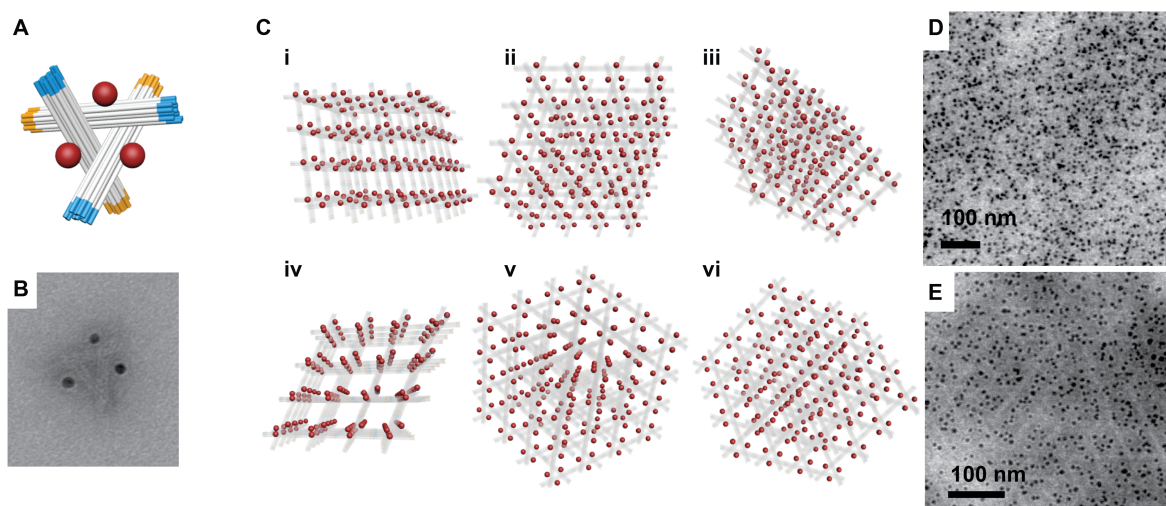


Figure 5.10: Building block units with multiple guest particles. Scheme (A) and the TEM image (B) of the building block with three gold nanoparticles. Views onto the 3D model of a lattice patch made from building blocks with three guest particles.(C) TEM images of the solution with monomers and polymerization strands after incubation at 45 °C. (D,E)

In Figure 5.10A the design of the triangular building block structure with three nanoparticles at the midpoints of the edges is shown. TEM imaging verified correct assembly of the building block and attachment of gold nanoparticles (Figure 5.10B). Different views on the lattice model are shown in Figure 5.10C. Polymerization of building blocks followed the described procedure for guest particle building blocks i.e. addition of polymerization oligonucleotides to assembled monomeric building blocks to induce shape complementarity [153]. The shape complementarity is intended to induce lattice formation during incubation at 45 °C. After 90 hours of incubation the solution of building blocks carrying three gold nanoparticles with polymerization strands was investigated with TEM. The corresponding TEM images are shown in Figure 5.10D and E. It can be seen that in the first TEM image in Figure 5.10D a rather irregular distribution of gold nanoparticles is found.

In certain parts of the TEM images the underlying assembled DNA origami lattice pattern becomes visible (Figure 5.10E). Along rows of DNA origami struts an accumulation of gold nanoparticles is observed. Figure 5.10C shows six different views on the lattice model. In view (i-iii) lattice views are shown that correspond to lines of gold nanoparticles in building block units carrying only one building block. View (i) shows rows of accumulated gold nanoparticles. In view (ii) and (iii) a rather irregular appearing distribution of gold nanoparticles is found. In view (iv) and (v) "stacks" of gold nanoparticles are visible as lines. View (vi) corresponds to the hexagonal patterning found in pure DNA origami lattices dried on TEM grids. A comparison to the TEM image at the bottom reveals similarities. DNA origami struts are visible and lines of gold nanoparticles are accumulated next to the struts. The orientation of the lattice patches on the grid or slight positional deviations from the ideal positions can hinder the accessibility of these patterns in projection images. Drying of the lattices on a surface for imaging can induce such deviations in TEM images. It remains to be determined if the structures found in TEM images reflect a correct assembly of building blocks carrying multiple guest particles. For verification of correct assembly of gold nanoparticle lattices with multiple guest particles additional methods might be helpful. SEM images so far have not revealed information about the success of assembly. A successful assembly of lattices with building block units of multiple guest particles remains to be confirmed.

### 5.2.8 Conclusion

Here we have presented a route to building 3D lattices using designable DNA origami building blocks. Computationally identifying [109] and releasing strain in the structures could result in further improved monomer quality, which together with large-scale screening of crystallization conditions. e.g., with seeded growth or hanging/sitting droplet crystallization, will potentially lead to the formation of DNA origami single-crystals that can host a wide variety of components. Importantly, the use of rigid DNA origami building blocks permits the variable positioning of guest molecules, which would allow for different "guest lattices" within the same framework and even dynamically reconfigurable lattices. The size of our origami monomer and therefore of the lattice unit cell is primarily limited by the available length of scaffold strands, an obstacle that can be circumvented by employing, e.g.,  $\lambda$ -phage scaffolds [171, 172], hollow struts, monomers built up from hierarchical assembly [62] or by DNA brick-based assembly [173].



# Appendix A

## Supplementary information - SAXS on DNA origami

In the following we explain the assembly of DNA origami structures, concentration and purification by PEG precipitation, as well as characterization with transmission electron microscopy (TEM) and atomic force microscopy (AFM). We depict the SAXS setup and explain data analysis, models and fit parameters in detail.

### **DNA origami assembly**

For each of the three structures, folding mixtures containing 100 nM of each DNA staple oligonucleotide (purchased from MWG Eurofins) and DNA scaffold strands (10 nM of p7308 scaffold for the 1-layer sheet; 30 nM of the p8064 scaffold for the brick; 30 nM of the p7560 scaffold for 24HB), 10 mM Tris, 1 mM EDTA and 14, 20, 12 mM  $\text{MgCl}_2$  for 24 helix bundle, three layer block and one layer sheet respectively were subjected to annealing ramps: For the assembly of Origami structures inside the SAXS-setup the folding solution described above was directly transferred to the sample chambers without any prior annealing. The annealing ramps for the assembly inside the setup are described below.

### **Concentration**

The folded structures were concentrated and purified from excess staples via PEG precipitation [174]. To the solution containing the folded Origami structures we added an equal volume of PEG precipitation buffer (15% PEG 1xTE 500 mM NaCl) and the  $\text{MgCl}_2$  concentration of the resulting solution was adjusted to 10 mM  $\text{MgCl}_2$  (independent of the  $\text{MgCl}_2$  concentrations during folding). This was followed by a step of centrifugation for

25 min at 20 degree and 16000 rcf. Then the supernatant containing excess staples was immediately removed and 500  $\mu$ l of 0.5 TBE 11 mM MgCl<sub>2</sub> (pH 8.5, 44.5 mM TRIS-Base, 1 mM EDTA, 44.5 mM boric acid) was added. This solution was incubated for 30 min shaking at roomtemperature and then the precipitation step was repeated. After the removal of the supernatant the purified origami structures were resuspended in 80-100  $\mu$ l of the final buffer. The final buffer was 0.5 TBE 11 mM MgCl<sub>2</sub> (pH 8.5(0)) except for the second set of experiments where buffers with MgCl<sub>2</sub> concentration of 0, 1, 2, 3, 5, and 11 mM were used. This solution was incubated for at least 24 h shaking at room temperature. The concentration of the Origami solution was confirmed using absorption measurements (Thermo Scientific NanoDrop<sup>TM</sup> 1000 Spectrophotometer) at wavelength 260 nm. The measurements suggest a yield close to 100% which corresponds to concentrations up to 270 nM of Origami.

### TEM Imaging

The cylinder-like and brick structure were imaged with a JEM-1011 transmission electron microscope (JEOL) at 80 or 100kV. The samples were diluted 10 times with the respective buffer (0.5xTBE and respective Mg concentration) and incubated on Argon plasma treated formvar/carbon coated (copper mesh) grids (Ted Pella, Inc; prod no. 01753-f) and washed and stained with 2% aqueous Uranyl Formate solution.

### AFM Imaging

The sheet structure was diluted to about 2 nM with 0.5xTBE 11 mM Mg buffer and placed on freshly cleaved mica. It was imaged with a MultiMode<sup>TM</sup> SPM 3 (Digital Instruments Veeco Metrology Group) in tapping mode (fluid) with SNL-10 silicon nitride cantilever (bruker.afmprobes.com) using a frequency of around 9kHz of the 0.24 N/m force constant cantilever. We used the Flatten-function of the WSxM program for the AFM image.

### Agarose Gel Analysis

Intermediate states of the 24HB during annealing were monitored using agarose gel analysis. Samples of the 24HB folding solution cooled down from 65 °C to 60 °C, 55 °C, 50 °C, 45 °C, 40 °C, 37 °C, 20 °C, shock-frozen after cooling to the target temperature and subsequently transferred to a 1% agarose gel of 1xTAE 11 mM MgCl<sub>2</sub> buffer. The gel was run at 120 V for 75 min.

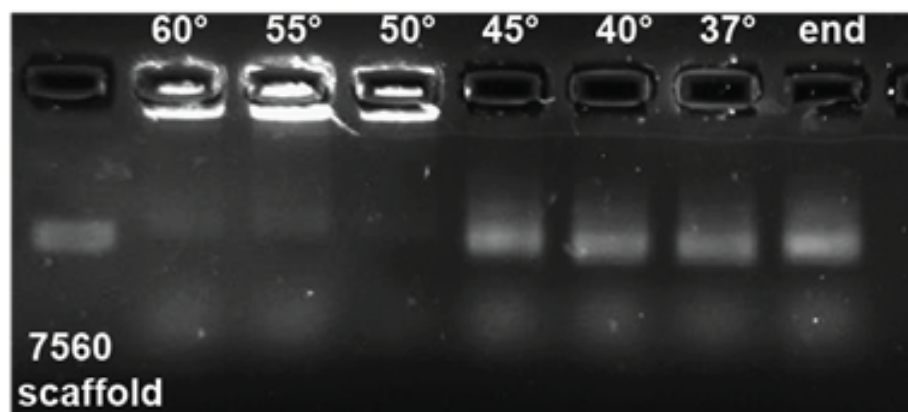


Figure A.1: Samples of the 24HB folding solution cooled down from 65 °C to 60 °C, 55 °C, 50 °C, 45 °C, 40 °C, 37 °C and 20 °C respectively as indicated. For reference in the first lane scaffold p7560. A band running faster than the scaffold can be seen for samples cooled down to 45 °C and lower. This band corresponds to folded DNA origami.

### SAXS setups

All SAXS measurements except of the DNA sheet and the melting and folding were performed at P08 beamline at DESY in Hamburg. The energy was set to 20 keV. The detector was a Perkin Elmer flat panel XRD 1621. The sample detector distance was set to 2309 mm and calibrated with silver behenate. The data of melting at low  $q$  values and folding of structure were measured with an in-house Mo Anode based X-ray setup [92]. It has Genix3D micro focus source and a Pilatus 100k detector. The sample to detector distance was set to 1110 mm. The data of the DNA sheet up to  $0.06 \text{ \AA}^{-1}$  was also measured with the in-house setup and a sample to detector distance of 2522 mm. Higher  $q$ -values for the sheet and melting curves were collected at ID01 at ESRF in Grenoble at a energy of 20 keV. A 2D Maxipix served as detector. For all measurements we used custom made sample chambers with a thickness of 10 mm and as window material served a  $25 \mu\text{m}$  Kapton foil.

### Melting and folding for in-situ measurements

For the determination of the intensity of  $I(0)$  (Figure 3.5(A,C)) of the melting of DNA origami three images with an integration time of 15 min were taken for each temperature step. In between we waited for 2 min in order to reach the desired temperature in the sample chamber. For the determination of the intensity and position of the peak (Figure 3.5(B,C)) one image for buffer and sample with integration time of 1 second were taken for each temperature step. Between each measurement we waited for 5 min in order to

equilibrate the temperature in the sample. For the folding the sample were heated to 65 °C and cooled down to 60 °C at 5 minutes per degree. The scattering intensity was always integrated over the time of the cooling per degree. From 60 °C down to 37 °C the sample was cooled for 30 minutes per degree. From 37 °C to 22 °C the integration time was again 5 minutes per degree.

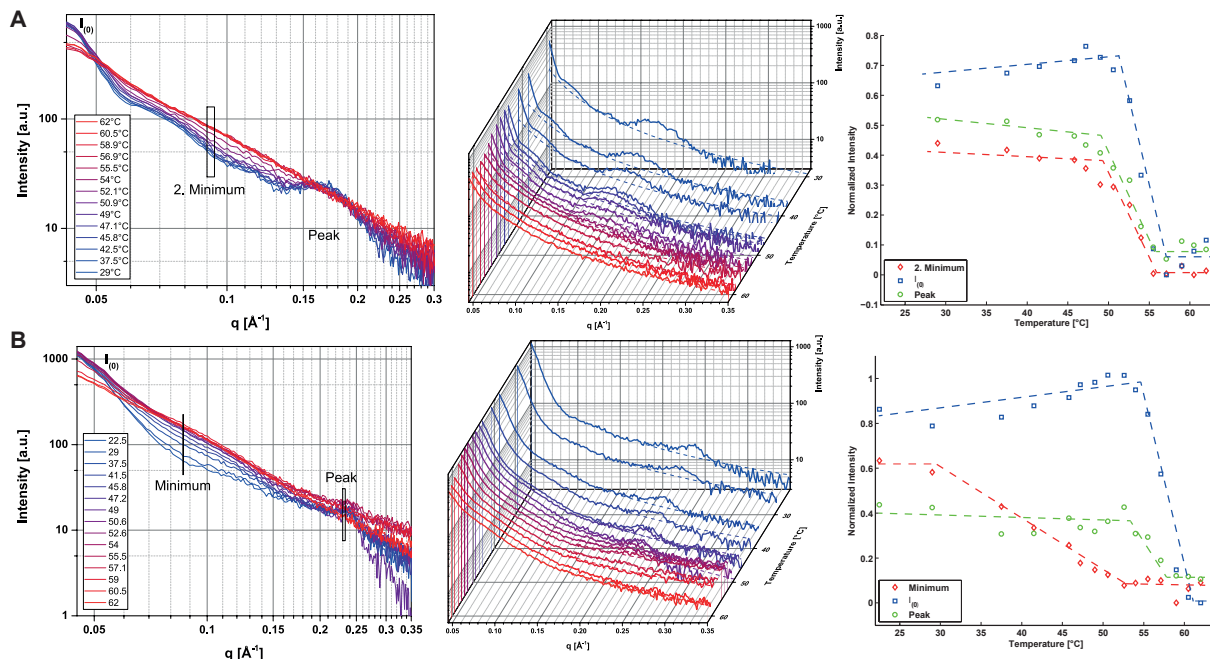


Figure A.2: Temperature dependent scattering intensity of DNA origami: (A) 24HB and (B) block left: scattering intensity with three positions of interest:  $I(0)$ , 1. or 2. Minimum and Bragg peak, center: Peak with used background (dashed lines) and right: normalized intensity of the three parameters (dashed lines serve as guide to the eye)

### Data treatment

For all data reduction the Plugin Nika [96] for Igor Pro was used. All in house data images are stacked and the median is taken for each pixel with ImageJ; all synchrotron data consists of only one image. If not stated differently, an image of the buffer with the same measurement time is subtracted accounting for the background. All data shown with the unit  $\text{cm}^{-1}$  are in absolute scale and are calibrated with glassy carbon.

## Data analysis

$$I(q) = \frac{S_{c1}}{V} \int_0^{\pi/2} F_{Cylinder}^2(q) \sin \alpha d\alpha + S_{c2} F_{peak}^2(q) + S_{c3} F_{Debye}(q) \quad (A.1)$$

$$I(q) = S_{c1} \int_0^{2\pi} \int_0^{\pi/2} |F_{SmallCylinder}(q) S_{lattice(q)}|^2 \sin \alpha d\alpha d\phi + S_{c2} F_{Debye}(q) \quad (A.2)$$

The simple model and the semi empirical approach with an additional peak use formula (A.1). For the simple model the scale factor  $S_{c2}$  is zero. Formula (A.2) is used for the fit with small cylinders in the lattice of the different DNA origami.

$$F_{(Small)Cylinder}(q) = 2\Delta\rho V \frac{\sin(qL \cos \alpha/2)}{qL \cos \alpha/2} \frac{J_1(qr \sin \alpha)}{qr \sin \alpha} \quad (A.3)$$

$J_1$  first order Bessel function,  $\alpha$  angle between the axis of the cylinder and q-vector,  $L$  length of cylinder,  $r$  radius of cylinder,  $\Delta\rho$  scattering length density difference (contrast) between scatterer and solvent.

$$S_{lattice} = \sum_i \exp(iq(x_i \sin \alpha \cos \phi + y_i \sin \alpha \sin \phi)) \quad (A.4)$$

$x_i$  and  $y_i$  are the coordinates of each lattice point,  $\alpha$  is the angle between the axis of the cylinder and qvector and  $\phi$  is the angle around the axis of the cylinder.

$$F_{Debye}(q) = \frac{2(e^{-q^2 R_g^2} - 1 + q^2 R_g^2)}{(q^2 R_g^2)^2} \quad (A.5)$$

$R_g$  is the radius of gyration. Debye background takes free oligonucleotides into account. Lorentzian shaped peak:

$$F_{peak} = \frac{1}{1 + \frac{1}{(q-q_0)^2}} \quad (A.6)$$

$q_0$  is the peak center and  $B$  is the HWHM (half-width half-maximum). The peak position  $q_0$  is related to the spacing  $d$  in the lattice:

$$d = \frac{2\pi}{q_0} \quad (A.7)$$

For the brick and the sheet (square lattice) the spacing  $d$  is the same as the inter-helical

distance  $a$ :

$$a_{\text{SquareLattice}} = \frac{2\pi}{q_0} = d \quad (\text{A.8})$$

For the hexagonal lattice of the 24 helix-bundle we have the relation:

$$\frac{1}{d^2} = \frac{4}{3} \frac{h^2 + hk + k^2}{a^2} \quad (\text{A.9})$$

with  $h$  and  $k$  as Miller indices of the 2D lattice. The first peak, which can be observed, has Miller indices  $h=1$  and  $k=0$  or  $h=0$  and  $k=1$ , which is at the same position. This results in the inter-helical distance of

$$a_{\text{HexagonalLattice}} = \sqrt{\frac{4}{9}} d = \sqrt{\frac{4}{9}} \frac{2\pi}{q_0} \quad (\text{A.10})$$

Instrumental smearing due to finite beam size and finite pixel size of the detector is included in the fits. The fitting routine uses a DREAM algorithm which uses a Markov chain Monte Carlo method.

### Simulation with CanDo, caDNAno and Crysol

Different approaches were taken to simulate SAXS scattering intensity from atomistic models. First a pdb file was generated and the scattering was simulated with Crysol [104]. The caDNAno file of the 24HB always served as starting point. We used CanDo [67] and varied the DNA diameter parameter to account for different inter-helical distances. 2.45 nm was found to fit the data best. All other parameters were kept at the standard values stated below. CaDNAno to PDB file converter was used as second approach in order to get a pdb file of the DNA origami. Additionally a minimization with NAMD [113] of the structure was used. For all results a Debye background was added. The result is shown in Figure A.3.

CanDo standard parameters:

Axial rise per base-pair [nm]	0.34
Crossover spacing [bp]	10.5
Axial stiffness [pN]	1100
Bending stiffness [pN nm <sup>2</sup> ]	230
Torsional stiffness [pN nm <sup>2</sup> ]	460
Nick stiffness factor	0.01

Table A.1: CanDo parameter

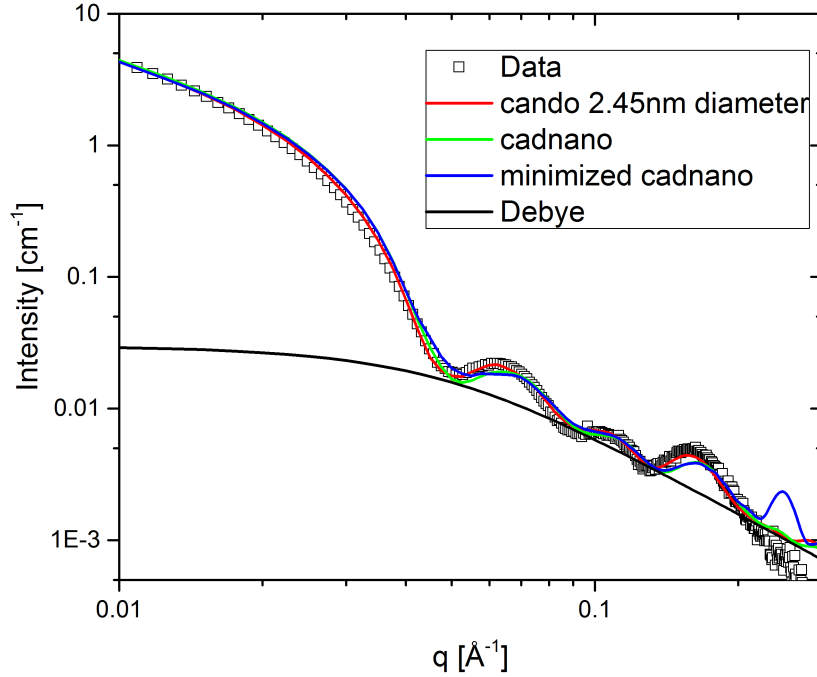


Figure A.3: Data of 24HB with different simulation based on caDNANO files with Crysol [104] of an atomistic model, all added with Debye background (black line): (red) CanDo with standard parameters (table below) and assuming a DNA diameter of 2.45 nm, (green) caDNANO to PDB file converter [113], (blue) caDNANO to PDB file converter with minimization [113]

### Detailed Fitparameter

Scattering length density of DNA:  $1.5e-5 \text{ \AA}^{-2}$

Scattering length density of buffer (water):  $9.43e-6 \text{ \AA}^{-2}$

Length of cylinder: 1000  $\text{\AA}$ (fixed)

Sample	A [ $\text{\AA}$ ]	B [ $\text{\AA}$ ]	C [ $\text{\AA}$ ]	R [ $\text{\AA}$ ]	L [ $\text{\AA}$ ]	$R_g$ [ $\text{\AA}$ ]
Cylinder	-	-	-	$78.66 \pm 0.13$	1000 (fixed)	30.4
Brick	$76.60 \pm 0.19$	$378.9 \pm 0.19$	$626.6 \pm 4.7$	-	-	8.7
Sheet	$21.49 \pm 0.31$	$610 \pm 60$	960 (fixed)	-	-	25

Table A.2: Fit parameter of geometric model

$MgCl_2$ Concentration	Scale $S_{c1}$	Radius r [ $\text{\AA}$ ]	Scale Peak $S_{c2}$	Peak Width B [ $\text{\AA}^{-1}$ ]	Peak Po- sition $q_0$ [ $\text{\AA}^{-1}$ ]	Scale Debye Back- ground $S_{c3}$	Radius of Gyration $R_g$ [ $\text{\AA}$ ]
11 mM	2.5e-4	78.66 $\pm 0.19$	3.0e-3	0.01954 $\pm 3.9e-4$	0.16519 $\pm 2.2e-4$	0.0266	30.4
5 mM	1.4e-4	79.77 $\pm 0.27$	2.1e-3	0.02758 $\pm 6.2e-4$	0.16171 $\pm 3.5e-4$	0.0293	34.4
3 mM	1.7e-4	81.46 $\pm 0.27$	2.4e-3	0.01502 $\pm 5.4e-4$	0.15826 $\pm 3.1e-4$	0.1002	47.9
2 mM	1.2e-4	83.31 $\pm 0.78$	2.0e-3	0.01979 $\pm 8.0e-4$	0.15256 $\pm 10.3e-4$	0.1876	61.2

Table A.3: Fit parameter of geometric model and Lorentzian peak for 24HB

$MgCl_2$ Concentration	Scale Debye Back- ground 1	Radius of Gyration 1 [ $\text{\AA}$ ]	Scale Debye Back- ground 2	Radius of Gyration 2 [ $\text{\AA}$ ]
1 mM	1.12	245	0.04	28.9
0 mM	0.27	144	0.03	22.3

Table A.4: Fit parameter of two Debye model for 24HB at low  $MgCl_2$  concentration

Scale	$a_{mean}$ [ $\text{\AA}$ ]	$w_a$ [ $\text{\AA}$ ]	Radius cylinder [ $\text{\AA}$ ]	Scale De- bye Back- ground	Radius of Gyration [ $\text{\AA}$ ]
1.85e-6	25.1	1.7	11	0.04	45

Table A.5: Parameter of small rigid cylinder model for 24HB

Sample	Scale	A [Å]	B [Å]	C [Å]	Scale Peak	Width Peak [Å <sup>-1</sup> ]	Position Peak [Å <sup>-1</sup> ]	Scale Debye Background	Radius of Gyration [Å]
Brick	3.0e-4	76.60 ± 0.19	378.9 ± 1.9	626.6 ± 4.7	2.0e-3	0.01005 ± 2.4e-4	0.23003 ± 1.4e-4	5e-3	8.7
Sheet	3.6e-4	21.49 ± 0.31	610 ± 60	960 (fixed)	4.6e-4	0.0354 ± 3.8e-3	0.23343 ± 1.7e-3	7.9e-3	25

Table A.6: Fit parameter of geometric model and Lorentzian peak for brick and sheet

Sample	Scale	$a_{mean}$ [Å]	$w_a$ [Å]	Radius cylinder [Å]	Scale Debye Background	Radius of Gyration [Å]	Constant Back-ground
Brick	2e-6	27.27	0.8	11	2.3e-2	45	5e-4
Sheet	1.8e-6	27.41	2.5	11	3.3e-3	25	2.2e-4

Table A.7: Parameter of small rigid cylinder model for brick and sheet

### Sizes calculated from inter-helical spacing and comparison with designed values

Diamonds in Figure A.4(A) show the calculated values of the inter-helical distance for the radius of the whole structure Figure A.4(B). The radius is calculated with  $R = \sqrt{7}a + r_{DNA} + shell$ . The fit values for the 24HB and the brick show that it is useful to add a shell of 0.14 nm, if we use a radius  $r_{DNA}=1$  nm for the DNA. The fit values for the honeycomb lattice of the 24HB fit well to the design values in Table A.8. For the square lattice structure the fitted values are higher than the designed values, because the interhelical distance is higher than 2 nm of the DNA plus 0.6 nm of the gap. The values of the inter-helical distance agree for all structures with the size of the whole DNA origami structure.

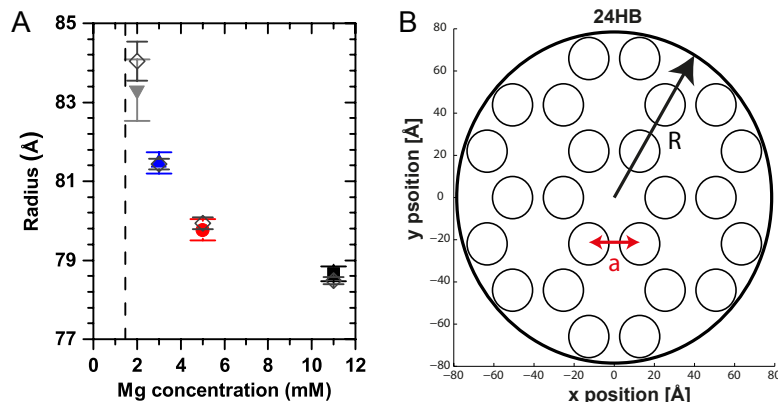


Figure A.4: Correlation of lattice constant and radius (A) Fit values for radius of simple model (colors) and calculated radius with lattice constant  $a$  (diamond, dark grey) (B) Model of a 24HB with Radius  $R$  and inter helical distance  $a$ , diameter of DNA double strand is 2 nm and an shell of 0.14 nm for the radius is added.

	A [number of helices]	B [number of helices]	C [number of bp]	R [number of helices]	L [number of bp]
Cylinder	-	-	-	$\sqrt{7}(2r_{DNA} + gap) + r_{DNA}$	284-298
Brick	3	14	168	-	-
Sheet	1	24	224	-	-

Table A.8: Designed Origami dimensions in number of basepairs or helices respectively.

	A [Å]	B [Å]	C [Å]	R [Å]	L [Å]
Cylinder	-	-	-	78.79	965.6-1013.2
Brick	72	358	571.2	-	-
Sheet	20	618	761.6	-	-

Table A.9: Designed origami dimensions in Å calculated for a rise per basepair of 3.4 Å (also counting deleted ones), a DNA-radius ( $r_{DNA}$ ) of 1 nm and interhelical distances (gap) of 0.6 nm. We accounted for double stranded parts of the DNA origami only.

	a [Å]	A [Å]	B [Å]	R [Å]
Cylinder	25.36	-	-	78.50
Brick	27.32	77.44	377.96	-
Sheet	26.92	22.80	668.88	-

Table A.10: Inter-helical distance from peak fit and corresponding size of DNA origami structures. DNA-radius of 1 nm is used and an additional shell of 0.14 nm is added.

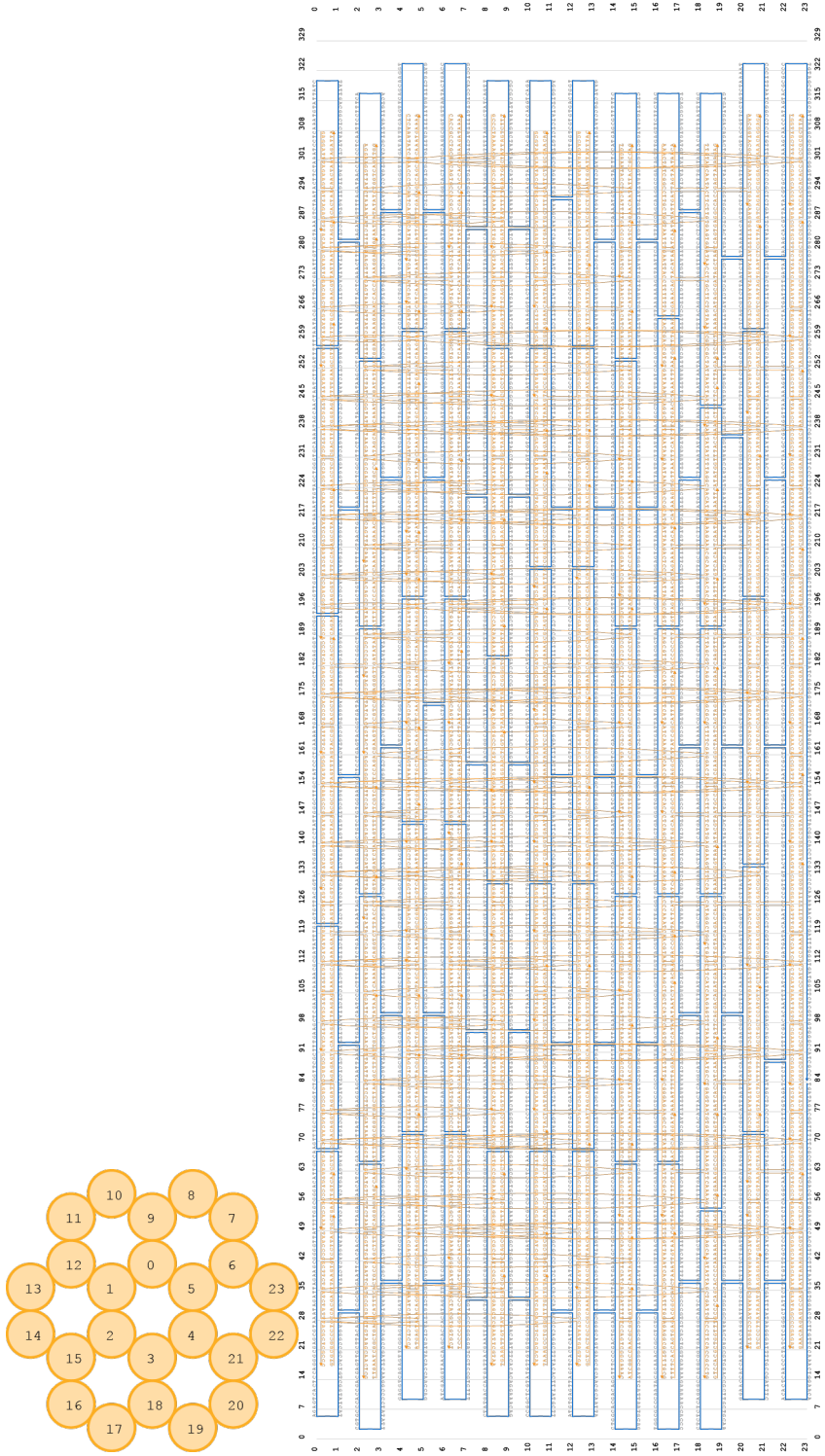


Figure A.5: caDNAno [66] design of the 24HB [110] (Scaffold blue and staple strands yellow).

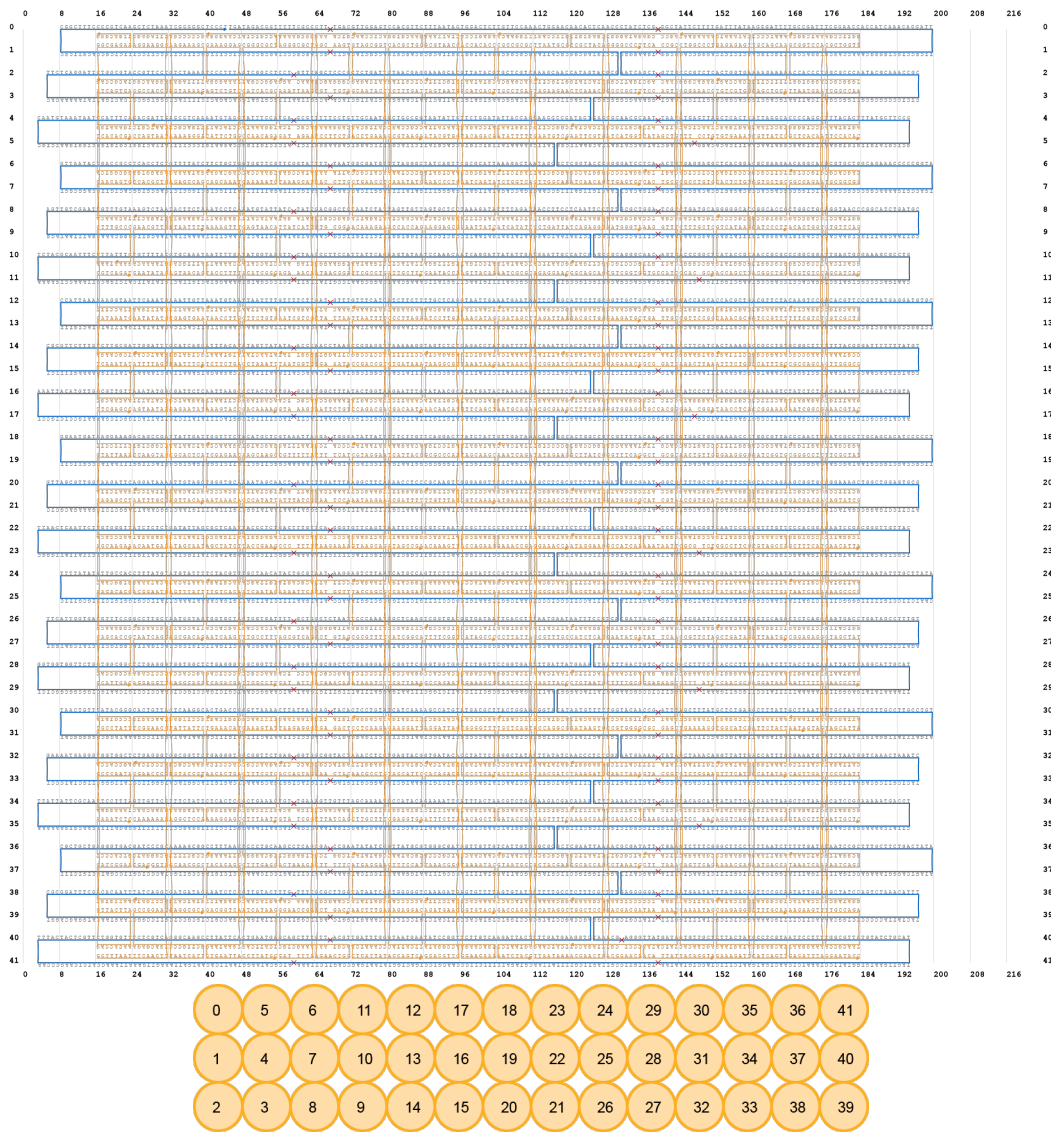


Figure A.6: caDNAno [66] design of the brick structure [52] (Scaffold blue and staple strands yellow).

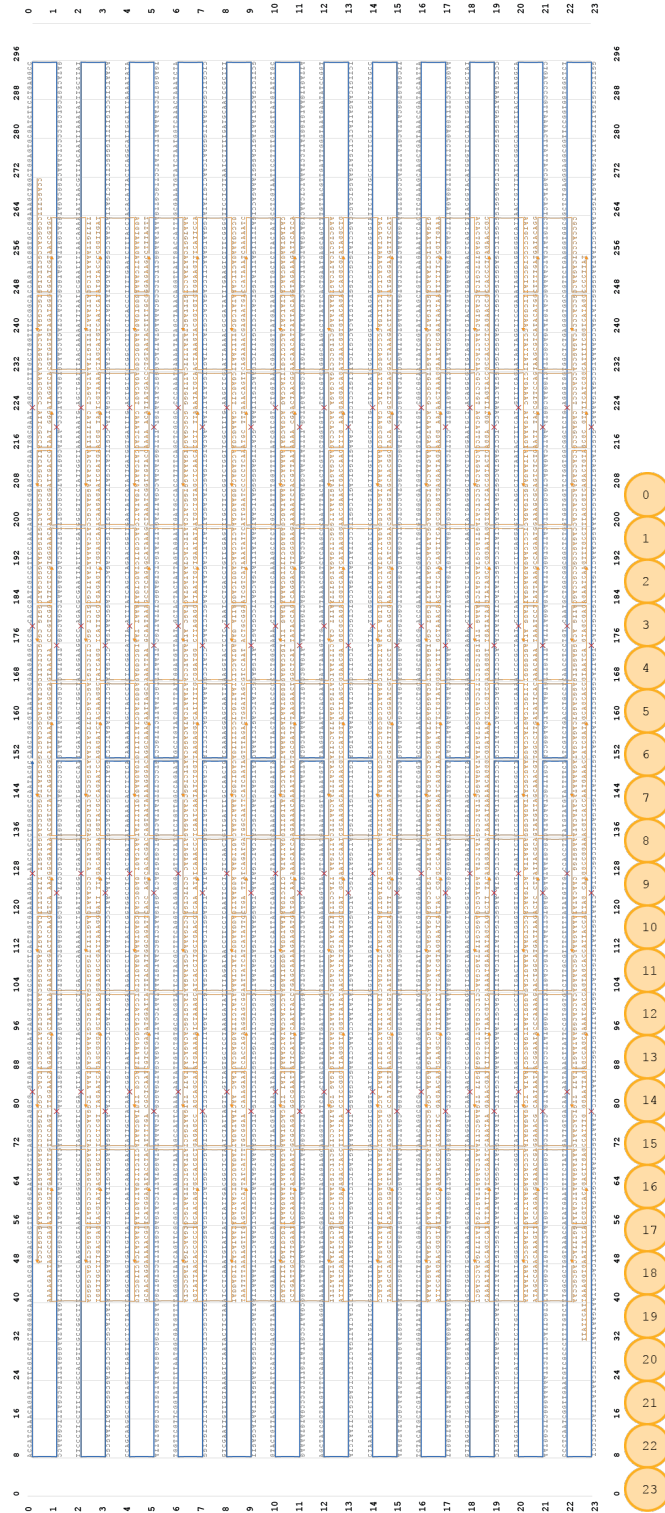


Figure A.7: caDNAno [66] design of the one-layer-sheet [32] (Scaffold blue and staple strands yellow).



# Appendix B

## Supplementary information - SAXS on AuNP DNA origami

### Supplementary Note S1: Assembly of gold nanoparticle DNA nanostructures Assembly of DNA Origami

A mix with 100 nM of each DNA staple oligonucleotide (purchased from MWG Eurofins) and DNA scaffold strands (10 nM of the p8064 scaffold for the block and of the p7560 scaffold for the bundle), 10 mM Tris, 1 mM EDTA and 20 or 14 mM MgCl<sub>2</sub> for the block and the bundle respectively was subjected to annealing ramps. CaDNAo designs [66] of the block origami structures are given in Supplementary Note SIII3 [52] and the design of the helix is as in [110]. To prevent AuNPs from getting caught in scaffold loops at the edges of the block structure, additional oligonucleotides with 4 base overhangs (CCCC) were used compared to the previously published design. Protrusions of DNA single strands from the structures are designed as explained in more detail below.

### PEG precipitation

For purification of the folded origami structures from excess staples after folding, origami solutions were mixed 1:1 with polyethylene glycol (PEG) precipitation buffer (15% PEG 1xTE 500 mM NaCl) and the mixture was centrifuged for 25 min at 20 °C and 16000 rcf [174]. Directly afterwards the supernatant containing excess staples was removed and the origami were resuspended in 1xTAE 11 mM MgCl<sub>2</sub> buffer (pH 8.5, 44.5 mM TRIS-Base, 1 mM EDTA, 40 mM acetic acid) and incubated for 30 min shaking at room temperature. A second precipitation step was performed and the origami were resuspended in the same buffer and incubated for 24 hours at room temperature.

### Functionalization and attachment of AuNPs

AuNPs of diameters of approximately 10 nm (BBI International) were covered with thiolated DNA oligonucleotides. 5'-thiolated DNA oligonucleotides of 19 bases of T ( $T_{19}$ ) (5'-HS-C6- TTT TTT TTT TTT TTT TTT T -3') or eight bases of T ( $T_8$ ) (5'-HS-C6- TTT TTT TT-3') or 3'-thiolated DNA oligonucleotides of 19 bases of either T ( $3'T_{19}$ ) (5'-HS-C6- TTT TTT TTT TTT TTT TTT T -3') or bases 5'-ATT ATT ATT ATT ATT TTTT C3-SH-3' (Biomers) - after treatment with TCEP (tris(2-carboxyethyl)phosphine) - were added in 200 times molar excess to the AuNP solution and the salt concentration was increased stepwise to 600 mM NaCl [143]. The AuNPs were then purified from excess DNA oligonucleotides with centrifugation filters (Amicon, 100000 MW cut-off). Purified DNA covered AuNPs were then added to the origami structure with a 5 times excess of AuNPs to binding sites on the origami and the  $MgCl_2$  concentration was adjusted to 11 mM. The mixture is incubated overnight for hybridization of the DNA-coated AuNPs to the complementary single-stranded DNA oligonucleotide protrusions from the origami [170], i.e. AAA AAA AAA AAA AAA-3' ( $A_{15}$ ) to  $T_{19}$  or  $3'T_{19}$ , AAA AAA AAA3' ( $A_9$ ) to  $T_8$ , and in the helix additionally 5'- ATT ATT ATT ATT ATT TTTT C3-SH-3' to protrusions 5'-AAT AAT AAT AAT AAT on the DNA origami bundle.

### Determination of the number of DNA oligonucleotides on AuNPs

For the determination of the number of DNA oligonucleotides on the AuNPs a known amount of DNA-coated AuNPs was dissolved and the DNA concentration in the resulting solution was measured to calculate back for the DNA-AuNP ratio [175]. Iodine ( $I_2$ , Fisher Scientific) and potassium iodide (KI, Fisher Scientific) (molar ratio 6:1) were added to deionized water where KI served to increase solubility of  $I_2$  in water. The  $I_2$ /KI solution with a final concentration of 0.34 mM of  $I_2$  was added dropwise to the functionalized AuNPs of determined concentration and volume until the initial red color of the AuNP solution disappeared. Purified water was added to a volume of 500  $\mu$ l and the resulting solution was loaded into NAP<sup>TM</sup>-5 columns (GE Healthcare) that had been washed three times with purified water. The sample was eluted with 1 ml of purified water and collected. The DNA concentration of the resulting solution was measured to calculate the number of DNA oligonucleotides on the AuNPs. Accounting for a surface area of a particle of 10nm diameter, the measured number of DNA oligonucleotides of around 77 per AuNP corresponds to a DNA-footprint of about 4 nm<sup>2</sup> per DNA-strand and is in agreement with

the values found in the literature [144].

### Electrophoresis

For purification we used 1% agarose-gel-electrophoresis with 1xTAE 11 mM MgCl<sub>2</sub> running buffer in a cooled ice bath to purify assemblies from excess AuNPs. The desired structures were recovered by excision from the gel of the second band counted from below and the corresponding coated AuNPs by excision of the lowest band.

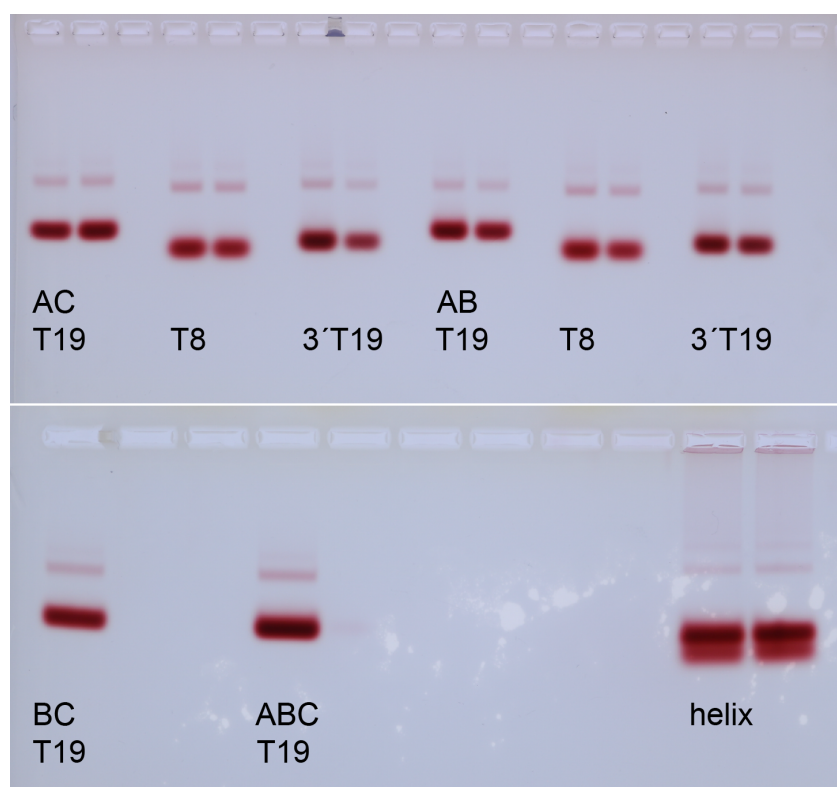


Figure B.1: Agarose gel for purification of the DNA mediated AuNP assemblies from excess AuNPs.

### UV/vis spectroscopy

The concentration of the origami solutions without AuNPs was measured using UV/vis absorption measurements (Thermo Scientific NanoDrop<sup>TM</sup> 1000 Spectrophotometer) at a wavelength of 260 nm. The concentration of origami with AuNPs was calculated from measured AuNP concentrations using absorption measurements at 520 nm and accounting for one AuNP per binding site. Dimer concentrations ranged from 0.5 to 1.2 nM. The concentration of the trimer was 2.4 nM and of the helix 0.25 nM.

### Transmission electron microscopy

Nanostructures were imaged using a EM-1011 transmission electron microscope (JEOL) at 80 kV. The samples were incubated on Argon plasma treated formvar/carbon-coated copper mesh grids (Ted Pella, Inc; prod no. 01753-f) and washed and stained with 2% aqueous uranyl formate solution. Dimer distances were obtained from the images with the software ImageJ [176]. To measure the center-to-center distance for the AB structure only top view TEM images and for the AC and BC structure only side view TEM images were considered in an attempt to exclude a bias towards lower distances due to projection of the geometry into two dimensions. Verification of the magnification was achieved by measuring AuNP diameters, which were found to be in agreement with the SAXS results. The TEM images used for measurements were taken at a magnification of 30000. The image size was 1024 x 1024 pixels. The center of the AuNP was determined by eye and the center-to-center distance was measured with the built in ImageJ measurement tool.

### Supplementary Note S2: Small angle X-ray scattering

#### SAXS measurements

SAXS data were recorded at the SAXS beamline at the ELETTRA synchrotron in Trieste [94]. We used a flow-through-cell with a quartz glass capillary of 1.5 nm diameter and measured at 8 keV X-ray energy (wavelength 0.154 nm). An evacuated flight tube was used to cover the sample-to-detector-distance of 1.328 m. A motorized beam stop was placed inside the flight tube. A Dectris Pilatus 3 1M CMOS Detector (981 x 1043 pixels with 172  $\mu\text{m}$  pixel size) served as a detector. Silver behenate was used for the calibration of sample detector distance and beam center. For each sample ten exposures of ten seconds were taken. The beam size was 0.5 x 1.6  $\text{mm}^2$  and a conical mask was used to restrict the azimuthal integration to the direction with higher resolution.

#### SAXS data analysis

Scattering intensities are shown as a function of  $q = \frac{4\pi}{\lambda} \sin \theta$  with the wavelength  $\lambda$  of the monochromatic X-rays and  $2\theta$  being the scattering angle. Measurements of 1xTAE 11 mM  $\text{MgCl}_2$  buffer served as background intensity. Background subtracted scattering data of the AuNP assemblies were fitted using the software SasView [88]. The built-in core-shell sphere model was used to fit the data of DNA-coated AuNPs. To determine

center-to-center distances of the dimers the following models were used:

### Simple dimer model

The simple dimer model neglects the DNA origami and considers the scattering of the AuNPs only. The scattering intensity was fitted with

$$I(q) = scale \cdot 10^8 \cdot (sld_{Au} - sld_{H_2O})^2 \cdot V^3 / (2 \cdot \langle V^2 \rangle) \cdot 2 \cdot F(q)^2 \left( 1 + \frac{\sin(qd)}{qd} \right) \quad (\text{B.1})$$

with the form factor  $F(q) = 3 \frac{\sin(qR) - qR \cos(qR)}{(qd)^3}$  of a spherical scatterer of radius  $R$  and the center-to-center distance of the two spherical particles of the dimer  $d$ . To account for particle polydispersity  $R$  is drawn from a Gaussian distribution around  $R_{mean}$  with standard deviation  $w_R$ .  $sld_{Au} - sld_{H_2O}$  is the scattering length density contrast in units of  $\text{\AA}^{-1}$  between gold and the aqueous solvent. The model intensity is normalized to two bodies.  $V = \frac{4}{3}\pi R^3$  is the gold particle volume and  $\langle V^2 \rangle$  the average of the squared particle volume using the Gaussian distribution of radii. A factor of  $10^8$  is included to obtain an intensity in  $\text{cm}^{-1}$ . In the  $q$  region below  $0.025 \text{ \AA}^{-1}$ , the scattering of the rectangular DNA origami block cannot be neglected. Therefore, the fitting range of the simple dimer model was set to 0.025 to  $0.095 \text{ \AA}^{-1}$ .  $R$ ,  $w_R$  and  $d$  were obtained from fitting.

### Full dimer and DNA model

In the extended dimer model considering scattering of DNA, i.e. the DNA linker shells on the gold nanoparticles and the rectangular DNA origami block, the scattering intensity was fitted with

$$I(q) = scale_{particles} I_{particles}(q) + scale_{DNAblock} I_{DNAblock}(q) \quad (\text{B.2})$$

where

$$I_{particles}(q) = I_{CoreShellSphere}(q) \left( 1 + \frac{\sin(qd)}{qd} \right) \quad (\text{B.3})$$

is the intensity of the gold particle dimer of distance  $d$  including the DNA shells and  $I_{DNAblock}(q) = I_{parallelepiped}(q)$  is the intensity from the rectangular DNA origami block. For  $I_{CoreShellSphere}(q)$  and  $I_{parallelepiped}(q)$ , the built-in models core-shell-sphere and parallelepiped of the software SasView were used. They account for unit conversion and volume normalization.

The form factor of a core-shell sphere of core radius  $R$ , shell thickness  $t$ , core density  $sld_{Au}$ ,

shell density  $sld_{DNA}$  and solvent density  $sld_{H_2O}$  is

$$F_{CoreShellSphere}(q) = \frac{3}{V_{total}} \left[ V(sld_{Au} - sld_{DNA}) \frac{\sin(qR) - qR \cos(qR)}{(qR)^3} + V(sld_{DNA} - sld_{H_2O}) \frac{\sin(q(R+t)) - qR \cos(q(R+t))}{(q(R+t))^3} \right]$$

$$V = \frac{4}{3}\pi R^3 \quad (B.4)$$

$$V_{total} = \frac{4}{3}\pi(R+t)^3 \quad (B.5)$$

To account for particle polydispersity,  $R$  is drawn from a Gaussian distribution around  $R_{mean}$  with relative standard deviation  $w_R/R_{mean}$ . The scattering intensity of a parallelepiped of side lengths  $A < B < C$  and scattering length density contrast  $sld_{DNA} - sld_{H_2O}$  is [88]

$$I(q) = \frac{scale}{V} ((sld_{DNA} - sld_{H_2O}) \cdot V)^2 \langle P(q, \alpha) \rangle \quad (B.6)$$

$$P(q, \alpha) = \int_0^1 \Phi_Q(\mu\sqrt{q - \sigma^2}, a) \left[ S\left(\frac{\mu c \sigma}{2}\right) \right]^2 d\sigma \quad (B.7)$$

$$\Phi_Q(q, \alpha) = \int_0^1 \left\{ S\left[\frac{\mu}{2} \cos\left(\frac{\pi}{2}u\right)\right] S\left[\frac{\mu a}{2} \sin\left(\frac{\pi}{2}u\right)\right] \right\}^2 du \quad (B.8)$$

$$S(x) = \frac{\sin(x)}{x} \quad (B.9)$$

$$\mu = qB \quad (B.10)$$

$$a = \frac{A}{B}, c = \frac{C}{B} \quad (B.11)$$

All core-shell sphere and parallelepiped parameters were obtained from fits to SAXS data of the individual components and kept constant in the fits to the dimer data. Dimensions of the block used for fitting in the extended model were  $a=76.7 \text{ \AA}$   $b=378.9 \text{ \AA}$   $c=626.6 \text{ \AA}$  [105]. Intensity data points in the range  $0.0076$  to  $0.15 \text{ \AA}^{-1}$  were used for fitting and  $scale_{particles}$ ,  $scale_{DNAblock}$  and the dimer distance  $d$  were allowed to vary. All models

were smeared with a pinhole function of  $0.001 \text{ \AA}^{-1}$  width and fitted to the data with the SasView-internal population-based DREAM algorithm until no further improvement of  $\chi^2/N_{pts} = 1/N_{pts} \sum_{pts} (I_{data} - I_{model})^2 / \Delta I_{data}^2$  could be obtained.  $N_{pts}$  is the number of datapoints in the fitted range and  $\Delta I_{data}$  the intensity error of the measured data from averaging over ten detector exposures and from azimuthal data integration.

### PDDF analysis with GIFT or GNOM

Buffer subtracted scattering data were transformed with the software GIFT [101] to a spatial domain. The results of the software GNOM [99, 152] from the ATSAS package were used for cross checking (data not shown).

The analytical function describing the PDDF of dimers of spheres of radius  $R$  and distance  $d$  can be derived from [98] for non-overlapping spheres of equal sizes and yields:

$$p(r) = 2\rho^2(p_0(r) + p_3(r, d)) \quad (\text{B.12})$$

With

$$p_0 = \frac{4\pi}{3}R^3r^2 - \pi R^2r^3 + \frac{\pi}{12}r^5 \quad (\text{B.13})$$

for  $r \leq 2R$  and  $p_0 = 0$  elsewhere and

$$p_3 = \frac{\pi r}{2d} \left\{ \frac{1}{3}2R^3[(2R)^2 - (d-r)^2] - \frac{1}{6}2R^2[(2R)^3 - |d-r|^3] + \frac{1}{60}[(2R)^5 - |d-r|^5] \right\} \quad (\text{B.14})$$

for  $d - 2R \leq r \leq d + 2R$  and  $p_3 = 0$  elsewhere. The location of the first maximum of the PDDF is determined by  $p_0(r)$ , i.e. the sphere size  $R$ . The second maximum of the PDDF results from the second term  $p_3(r)$ . The location of this maximum is dominated by the distance  $d$  but slightly shifted with respect to it [177]. In Supporting Figure B.2 we show an example for spheres of size  $R=4.23 \text{ nm}$ , similar to the gold core of the nanoparticles used here, assuming that the DNA shell can be neglected. For a center-to-center distance of  $d=20 \text{ nm}$ , the position of the maximum of the PDDF  $r_{2ndmax}$  (black triangle) coincides within  $0.5 \text{ nm}$  with the nominal distance of  $20 \text{ nm}$  (vertical line). The shift of the second maximum seen with respect to the actual center-to-center distance [177] here remains small. In simulations effects of a block sitting in between the particles appear in form of a side maximum in the BC configuration. Indeed, also in the experimental PDDF of configuration BC a side-maximum is observed (cf. Fig 4.5).

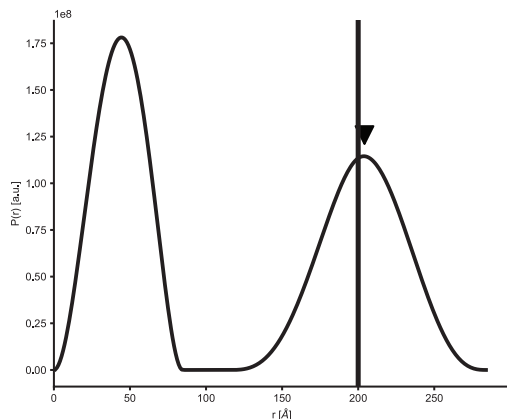


Figure B.2: Plot of PDDF of a dimer of spheres with Radius  $R=4.23$  nm and center-to-center distance  $d=20$  nm.

### Simulation of the PDDF of a particle helix

The PDDF of the particle helix was simulated using a Monte Carlo approach by Kilian Frank, [147]. A histogram of the pairwise distances was calculated from random coordinates inside the assembly [145, 146, 178]. To simulate the PDDF of a particle helix, the center position of the  $n$ -th particle is calculated as

$$\vec{r} = (R_{helix} \cos(n \cdot 60^\circ), R_{helix} \sin(n \cdot 60^\circ), n \cdot p) \quad (\text{B.15})$$

where  $R_{helix}$  is the radius of the particle helix and  $p$  is the helix pitch. The whole helix is composed of nine spherical particles,  $n=1$  to 9. 200 points of random position are drawn inside each sphere and the pair distances between all  $N=1800$  random points inside the spheres of the particle helix are calculated. The histogram of the found distances is used as the simulated PDDF.

## Supplementary Note S3: Design details of the AuNP-DNA nanostructure-assemblies

### Geometry calculation

#### Dimeric and trimeric configuration of AuNPs

The connector lengths, i.e. the distance of the surface of the AuNP to the surface of the DNA origami for structures AC and BC are calculated under assumption of the given ge-

	Core radius $R_{mean}$ [Å]	Distribution of core radius $w_R/R_{mean}$	Shell thickness $t$ [Å]	shell SLD $sld_{DNA}$ [10 <sup>-5</sup> Å <sup>-2</sup> ]
T <sub>19</sub>	42.4	0.094	57.1	1.06
T <sub>8</sub>	42.2	0.097	35.1	1.05
3'T <sub>19</sub>	42.3	0.094	46.9	1.01

Table B.1: Fit parameters of the functionalized AuNPs from a core-shell model fit. Radius, distribution of radius, shell thickness and shell SLD were then used in the fits with the extended dimer model. The pure AuNP has a radius of 42.1 Å and a distribution of the radius of 0.094 obtained from a fit with a sphere model.

ometry (Figure 4.4) and dimensions given by prior measurements (thickness of the origami block  $a=7.66$  nm [105], AuNP radius  $R=4.23$  nm), or by design (horizontal shift between attachment site A and attachment site C ( $s_{AC}$ ) of 4.8 nm, and horizontal shift between attachment site B and attachment site C of  $s_{BC}=16.7$  nm accounting for 0.34 nm per bp and assuming an interhelical distance of 2.7 nm for calculation of the circumcenters of the attachment sites. For the calculations of the connector length the position of the second peak of the PDDF obtained by GIFT is used as center-to-center distance  $d$  of the particles. The connector length  $c_{dimer}$  of the dimers therefore is:

$$c_{dimer} = \frac{1}{2} * \sqrt{d^2 - s^2} - R - \frac{a}{2} \quad (\text{B.16})$$

This yields the following values: For T<sub>19</sub> the connector length was obtained from dimer

	connector length $c_{dimer}$ [nm]
T <sub>19</sub>	4.9 ± 0.8
T <sub>8</sub>	2.6 ± 0.8
3' T <sub>19</sub>	3.2 ± 0.8

Table B.2: Calculated connector length in AuNP dimers.

AC (5.2 nm) as well as from dimer BC (4.6 nm). Both values are in reasonable agreement and were averaged. The calculated length of the connectors is compared to values corresponding to the length of double stranded DNA: For the T<sub>19</sub> connector 4.9 nm would correspond to a length of 14-15 bp, the T<sub>8</sub> connector length 2.6 nm would correspond to 7-8 bp and the 3' T<sub>19</sub> connector length 3.2 nm would correspond to 9-10 bp.

In addition, values of the connector length are compared to the design: For our estimate of a maximum connector length we account for 0.34 nm per base pair in double stranded DNA

and 0.65 nm per base for single stranded bases. Lengths between zero and this maximum value are assumed to be in agreement with the design without using any prior ideas about the connector: Therefore, all connector lengths found are in agreement with the design.

### Helical geometry of AuNPs

For the helix AuNP pair distances between the n-th and the first AuNP are given by

$$d_{helix-n} = \sqrt{2 \cdot R_{helix} \cdot \sin(30^\circ \cdot n)^2 + \left(\frac{p}{6} \cdot n\right)^2} \quad (\text{B.17})$$

and therefore the connector length  $c_{helix}$  is calculated using

$$c_{helix} = \sqrt{d_{helix-n}^2 - \left(\frac{p}{6} \cdot n\right)^2} / (2 \cdot \sin(30^\circ \cdot n)) - R_{DNAbundle} - R \quad (\text{B.18})$$

$R_{helix}$  is the radius of the helix,  $p$  the pitch and  $n$  the number of the AuNP neighbor in the helix. Assuming a pitch of 57 nm the read off distances of 21.2 nm and 36.4 nm for the maxima indicating the nearest and next nearest neighbor distances correspond to a radius of the helix of 18.9 nm or 17.9 nm, respectively. Their average is  $R=18.4$  nm. As the radius of the DNA origami bundle is  $R_{DNAbundle}=7.87$  nm [105] and assuming a gold nanoparticle radius of 4.23 nm the connector distance is calculated to be 6.3 nm, which is the length of about 18-19 double stranded base pairs. Deviations from the dimer result might be due to deviations of the radius in the nanoparticle batch using the ATT ATT ATT TTTT modification or details in the design. Differences to the connector length in the dimers could arise from the different protrusion distribution in the honeycomb lattice based rod structure and the square lattice based block structure (Supporting Figures B.3 and B.4). The value for the connector distance of the helix is therefore in agreement with the design.

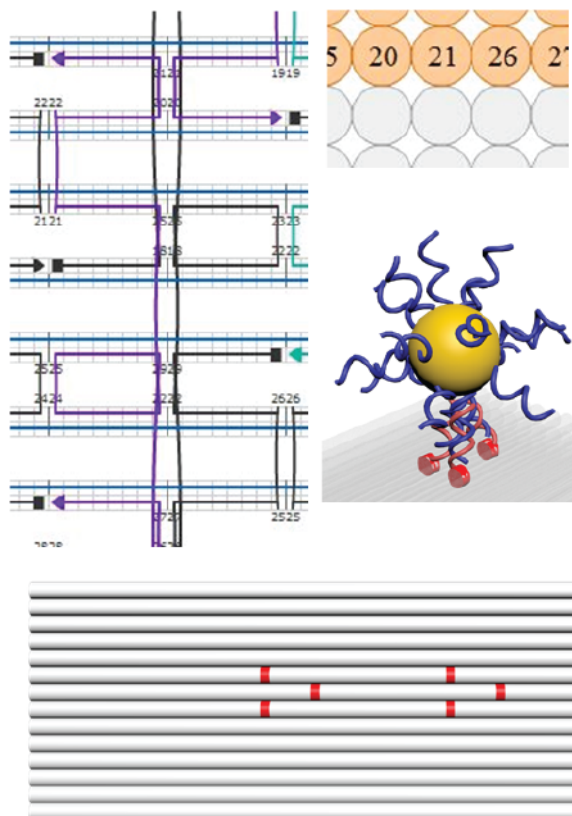


Figure B.3: Attachment sites of the DNA origami block as in attachment site A. Left: zoom in of the attachment site staples in the caDNAno [66] design, middle: helix arrangement at the surface where attachment site staples protrude. Right: attachment site protrusion positions marked in red on the block structure.

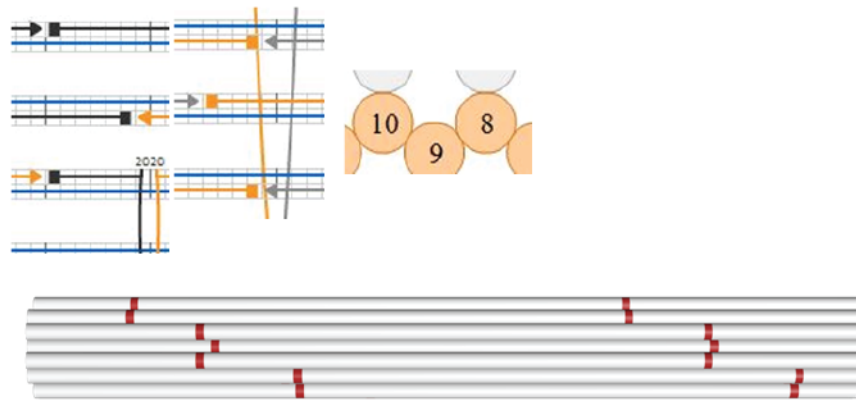


Figure B.4: Attachment sites of the helix. Left: zoom in of the attachment site staples in the caDNAno [66] design, middle: helix arrangement at the surface where attachment site staples protrude. Right: attachment site protrusion positions marked in red on the rod structure.

End-oligonucleotides marked in red additionally have an overhang of four bases (CCCC).

```

CCCCAATCCTGTTTGATGGTTGCCCCAGCAGGCGAACCCC
CCCCGCGAACGTATTATTACATTGCCCC
CCCCGTGTTTTTTATAATTGACAACCTCCCC
CCCCCGGAAGCATAACGCGCGGGGAGAGCCCC
CCCCGCAGATTCACCAGGTATTAACCCCC
CCCCTACCGGGGGTTTCTGCGCCGTTTTTCACGGTCACCCC
CCCCACCGCCTGGAAATTGCGTAGACCCC
CCCCCGTATTAAATCCAAAGAACGCGCCCC
CCCCCAGGCGCTTTCCAAATCGTTAACGCCCC
CCCCTTTTCAGGTTTAATTTAATGGCCCC
CCCCGCACATCCTCATAACGGCAGCCTCCGGCCAGACCCC
CCCCAAACAGTACAACATGTAATTTCCCC
CCCCAGAAAACCTTTTCCAACGCTAACCCCC
CCCCTACCAGTCCCGGTTGTGTACATCGCCCC
CCCCAGGCAGAGGCATTATCATTCCCCC
CCCCAGGGGGATGTGCTGCATACGCCAGCTGGCGAACCCC
CCCCAAGAACGGAGAATTGAGTTAACCCC
CCCCGAGCGTCTTTCTCACCAATGAACCCC

```

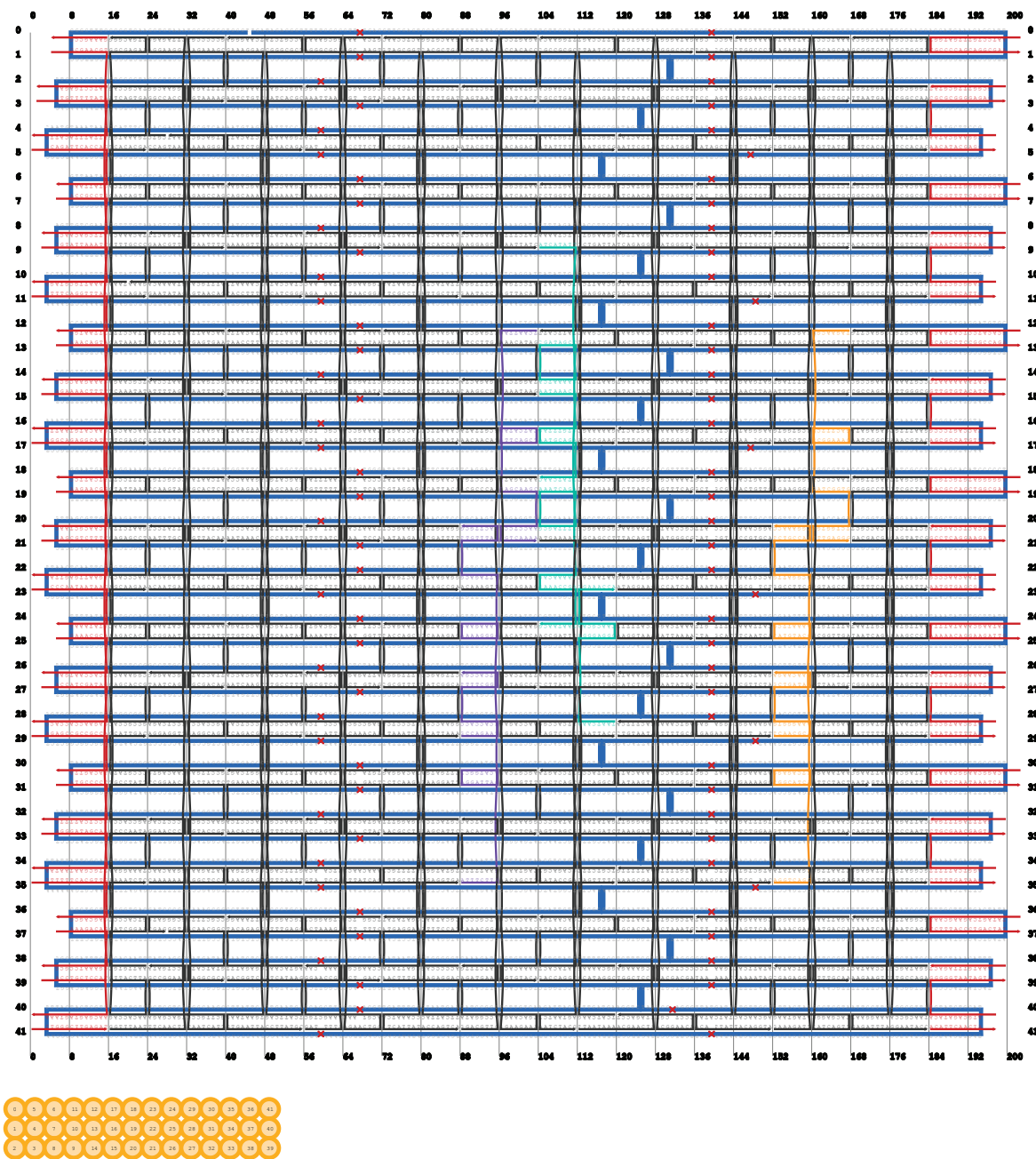


Figure B.5: CaDNAno [66] design of the block (adapted from [52, 170]).

CCCCGTAACAACCCGGCCTCAGGAAGATCCCC  
CCCCGCCCAATAATAAGATATAAAAACCCC  
CCCCTATAAGCAAATATTTAAAAAACAGGAAGATTGCCCC  
CCCCGAAACGCACAGAACCACCACCCCCC  
CCCCACCATCGATAGCCCTCATTTTCCCCC  
CCCCATGCAATGCCTTTTTTGAGAGATCTCCCC  
CCCCAGAGCCGCCGCAAACAGTTACCCC  
CCCCACAGGCAAGGCAAAGAACATCCAATAAATCATCCCC  
CCCCATGCCCCCTTGCGAATAATAACCCC  
CCCCAGGGATAGCAACGAAATCCGCGCCCC  
CCCCAGGTCATTTTTCTGCGAACGAGTACCCC  
CCCCTTTTTTCACGTTGCAGCAGCGCCCC  
CCCCTATAGTCAGAAGCAAATCTTTACCCTGACTATCCCC  
CCCCAAAGACAGAACGAGTAGTAAACCCC  
CCCCATGCAGATACAGGGGGTAATAGTACCCC  
GAAAGCCGCCCC  
AATCCTGAGAACCCC  
CCCCGCGGTTTGCGTAT  
AACATACGAGCCCCC  
CCCCGCATCAGATGCCG  
CGGGGTCATTGCCCC  
CCCCACATAAAAAAATC  
AGCGCCATGTTCCCC  
CCCCCGCACTCCAGCCA  
AATGTGAGCGACCCC  
CCCCACAAAGGCTATCA  
ATATATTTTAACCCC  
CCCCGATTTAGTTTGAC  
CTTTTGATAAGCCCC  
CCCCAAATGTTTAGACT  
CCCCACCTGCTCCAT  
CCCCTTGGGCTTGAGAT  
ACATTCAACTACCCC

## Protrusions for AuNP attachment

AACGACTTTCTGATCGGTGTCTGGTGCTTTGAGGGAAAAAAAAAAAAAAAAA  
TCGTATGTACCGCGGATTGTCTGCCAGCGGAAACCAAAAAAAAAAAAAAAAAA  
AGCTGGCATCAAAAGGGTGGCTGATAAAAACAAGAAAAAAAAAAAAAAAAA  
GCTTATCATATTAGCAAGCAACCTCCCCGTCAAAAAAAAAAAAAAAAAA  
AACAAAAGGGCATTAGACGTTGTTTAAGACTTGCGAAAAAAAAAAAAAAAAA  
GCTAGGATTAGCCACCACCTTTTCGGTGTCAACCGAAAAAAAAAAAAAAAAA  
TCACGATAGCTCTGTTTAGAATGCAGATTATCAACAAAAAAAAAAAAAAAAA  
GCGAAATCAGAAAAACAGGAAACCGATAATAACGAAAAAAAAAAAAAAAAA  
TAATCAAAAGGGAGGGTAACGCAAGGAAACCAAAAAAAAAAAAAAAAAA  
CGTTCAGCTTATCATATTAGCAAGCAACCTCCCCGTCAAAAAAAAAAAAAAAAAA  
TAAAAGAACAAAAGGGCATTAGACGTTGTTTAAGACTTGCGAAAAAAAAA  
AACATGGCTAGGATTAGCCACCACCTTTTCGGTGTCAACCGAAAAAAAAA  
TCAAATCACGATAGCTCTGTTTAGAATGCAGATTATCAACAAAAAAAAA  
ATTTTAGCGAAATCAGAAAAACAGGAAACCGATAATAACGAAAAAAAAA  
TAATCAAAAGGGAGGGTAACGCAAGGAAACCAAAAAAAAAA  
AACGACTTTCTGATCGGTGTCTGGTGCTTTGAGGGAAAAAAAAA  
TCGTATGTACCGCGGATTGTCTGCCAGCGGAAACCAAAAAAAAAA  
AGCTGGCATCAAAAGGGTGGCTGATAAAAACAAGAAAAAAAAA



# Appendix C

## Supplementary information - 3D-DNA origami lattices

### Design and formation of DNA origami:

#### Design:

The triangular origami designed using caDNAno [66] structure consists of three 14 HBs packed on a honeycomb lattice with a diameter of about 12.5 nm. These three 14 HBs were designed to be of the same length (199 bp) and display self-matching shape complementary blunt ends. The 14 HBs were interconnected at selected positions by forced crossovers with three bases of scaffold spacers. In order to avoid topological traps of the struts in undesired geometries, a "seam" was introduced into one of the 14 HBs. Here the scaffold does not run from one end of the strut to the other but loops back in the middle of the strut for each pair of helices. The seam is closed by staple oligonucleotides. Groups of staple strands were divided into "connection" oligonucleotides (closing the seam), "polymerization" oligonucleotides (completing the ends of all struts and thus enabling blunt end stacking), "handle" oligonucleotides (for capturing the gold nanoparticles) and "core" oligonucleotides (all other strands). It was observed that the presence of the seam oligonucleotides during the entire folding process leads to the formation of mainly deformed structures, possibly resulting from prematurely closed seams trapping the triangular struts in wrong geometries. Injection of the seam connectors at lower temperatures improved the yield of correctly folded triangles to  $\approx 60\%$ . While all misfolded objects featured three edges, they did not exhibit the designed three-fold symmetry (Figure 5.5 asterisk). Note that due to their structural similarity to the targeted design, these defective objects could not be removed during the purification steps but remained in solution during crystal growth.

**Folding and Purification:**

DNA origami structures were prepared by mixing core and handles staples ( $100 \times 10^{-9}$  M each, MWG Eurofins), and the circular DNA scaffold strand p8634 ( $12.5 \times 10^{-9}$  M, produced in house) in  $1 \times$  TE-Mg<sup>2+</sup> buffer ( $10 \times 10^{-3}$  M Tris,  $1 \times 10^{-3}$  M EDTA,  $18 \times 10^{-3}$  M MgCl<sub>2</sub>). The mixture was thermally annealed from 65 to 4 °C over 35 h (15 min at 65 °C, cooling to 58 °C with a cooling rate of -1 °C per 5 min, 58 °C to 35 °C with rate of -1 °C per 1 h, and from 35 to 4 °C with rate of -1 °C per 5 min). Connection staples were injected into the folding mixture during the annealing process at 52 °C. Subsequently the folded DNA nanostructures were purified from excess DNA staples by agarose gel electrophoresis stained with  $1 \times$  SybrSafe (1 % agarose in  $1 \times$  TAE  $11 \times 10^{-3}$  m MgCl<sub>2</sub> buffer; 6.5 V cm<sup>-1</sup> for 2 h) or by PEG precipitation.[179, 174] For agarose gel purification, samples were run in 1% agarose gels containing  $1 \times$  Tris acetate buffer ( $10 \times 10^{-3}$  M Tris,  $10 \times 10^{-3}$  M acetic acid),  $11 \times 10^{-3}$  M MgCl<sub>2</sub> and  $1 \times$  SybrSafe (Thermo Fisher Scientific). All gels were cooled in ice water baths. Samples were separated at 6.5 V cm<sup>-1</sup> for 2 h following excision of the bands and recovery of the products by squeezing the band between two glass slides and collecting the resulting liquid droplet with a pipet. For PEG precipitation, equal volumes of  $2 \times$  PEG buffer (15% (w/v) PEG-8000,  $2 \times$  TE,  $500 \times 10^{-3}$  m NaCl,  $20 \times 10^{-3}$  M Mg<sup>2+</sup>) and unpurified folding solution were mixed and centrifuged for 30 min at 16 000 rcf. The resulting pellet was re-suspended in  $1 \times$  TAE,  $11 \times 10^{-3}$  M MgCl<sub>2</sub> buffer and subsequently shaken at 650 rpm, 30 °C for 24 h in order to redisperse the origami structures.

**Formation of DNA origami-gold nanoparticle conjugates:****Functionalization of Gold Nanoparticles with DNA:**

Gold nanoparticles (AuNPs, BBI International) of 10, 20, and 30 nm were functionalized with 5'-thiolated 19T singlestranded DNA (Biomers) following published methods. [170] Briefly, TCEP (tris(2-carboxyethyl)phosphine) treated thiolated DNA was added in excess ( $200 \times$  molar excess for 10 nm AuNPs,  $800 \times$  for 20 nm AuNPs, and  $1800 \times$  for 30 nm AuNPs) to AuNPs. The mixture was incubated at room temperature for 24 h before slowly increasing the salt concentration to  $500 \times 10^{-3}$  M by addition of 1 M NaCl over a period of 6 h. DNA-modified gold nanoparticles were then purified using Amicon centrifugation filters (100K MW cut-off).

**Conjugation of gold nanoparticles to DNA origami:**

Six staple oligonucleotides at the center of the triangular origami structure were extended from the struts with 19A bases serving as handles for attachment of the gold nanoparticles (one nanoparticle per origami nanostructure). An  $8 \times$  molar excess of DNA-AuNPs was added to the DNA origami structures and incubated at room temperature overnight. The resulting DNA origami-gold nanoparticle conjugates were purified from excess gold nanoparticles in 1% agarose gels containing  $1 \times$  Tris-acetate,  $11 \times 10^{-3}$  M  $\text{MgCl}_2$  buffer, cooled in an ice-bath. Samples were separated at  $7 \text{ V cm}^{-1}$  for 1.5 h. Bands were excised from the gel and recovered as described previously.

**Polymerization of DNA origami into 3D Lattices:****Polymerization:**

Polymerization oligonucleotides were mixed at  $10 \times$  molar excess with purified bare triangular origami structures or with purified structures carrying gold nanoparticles. The buffer was then brought to  $1 \times$  TAE and  $15 \times 10^{-3}$  M  $\text{MgCl}_2$ . The polymerization mixture was incubated at a constant temperature of  $47^\circ\text{C}$  for 3-4 d in a thermocycler. Owing to the different purification procedures and varying purification yields, the starting concentration of origami monomer for pure DNA origami lattice growth was  $\approx 25 \times 10^{-9}$  M (PEG purified), while for lattices with gold particles the starting concentration of the gold-carrying monomers ranged between  $1 \times 10^{-9}$  and  $3 \times 10^{-9}$  M (gel purified). As defective monomers lack the designed symmetry, their overall binding energy does not suffice to stabilize their integration in the lattice at the elevated temperatures during lattice growth.

**Characterization Techniques:****TEM:**

TEM imaging of DNA origami lattices was carried out using a JEM-1011 transmission electron microscope (JEOL) operating at 80 or 100 kV. For sample preparation  $10 \mu\text{L}$  of polymerized DNA origami structures were deposited on glowdischarged TEM grids (formvar/carbon-coated, 300 mesh Cu; Ted Pella, Inc; prod no. 01753 - f) for 1 h. For pure origami lattices and origami lattices containing 10 or 20 nm gold nanoparticles, grids were furthermore quickly washed once with 0.1% uranyl acetate solution ( $5 \mu\text{L}$ ) and immediately afterward stained with 0.1% uranyl acetate solution ( $5 \mu\text{L}$ ) for 10 s. For origami lattices hosting 30 nm gold nanoparticles and the lattices for taking SEM images, grids were washed two times with water for 2 s.

**SEM:**

The TEM grids were directly used for SEM imaging after 10 s sputtering using an Edwards Sputtercoater S150B 1990. The sputter target contained 60% gold and 40% palladium. Process parameters used for sputtering were 7 mbar Ar, 1.1 kV, 35 mA. 10 s sputtering results in the deposition of layer of gold/palladium with a thickness of a few nm. The Au/Pd deposited TEM grids were directly fixed on the sample holder with carbon tape for SEM imaging with a Carl Zeiss LEO DSM 982 GEMINI (containing a source of thermal field emitting cathode (1997) and a detector of LEO High Efficiency In-Lense Secondary Electrons). Beam parameters for taking imaging were set as 5 kV acceleration voltage and 30  $\mu\text{m}$  aperture.

**SAXS:**

The SAXS data were measured at four different sources. All samples to detector distances and beam centers were calibrated with silver behenate. The scattering data of the monomer shown in Figure 5.7 and dataset i were measured at an in-house X-ray source, which is described in detail in the literature. [92] The data of the undecorated DNA origami lattice and the DNA origami lattice decorated with 20 nm gold nanoparticles, Figure 5.7, dataset ii and iii were measured at the SAXS beamline at ELETTRA in Trieste. The solutions of polymerized sample were loaded in a 1 mm flow-through quartz capillary and measured at 8 keV X-ray energy. A Dectris Pilatus 3S1M CMOS detector with  $981 \times 1043$  pixels with 172  $\mu\text{m}$  pixel size served as detector. The data of the DNA origami lattice decorated with 10 nm gold nanoparticles shown in Figure 5.7, dataset iv were measured at the beamline P08 at PETRA III (DESY) in Hamburg. A Perkin Elmer flat panel XRD 1621 with  $2048 \times 2048$  pixels with 200  $\mu\text{m}$  size served as detector. The solutions of polymerized sample were loaded in 2 mm quartz capillaries. The measurement was carried out at 20 keV in order to avoid radiation damage of the sample. The melting process shown in Figure 5.8 was recorded at the beamline ID02 of the European Synchrotron Research Facility (ESRF) in Grenoble at an X-ray energy of 12.46 keV. A Rayonix MX170-HS with  $960 \times 960$  pixels of 177  $\mu\text{m}$  size served as detector. The sample was loaded in a temperature-controlled flow-through cell with a 1.5 mm quartz glass capillary.

# Bibliography

- [1] Nano.gov. National Nanotechnology Initiative, “What is nanotechnology.” <https://www.nano.gov/nanotech-101/what/definition>. (last accessed 2018-10-12).
- [2] M. I. Stockman, “Nanoplasmonics: The physics behind the applications,” *Phys. Today*, vol. 64, no. 2, pp. 39–44, 2011.
- [3] I. Freestone, N. Meeks, M. Sax, and C. Higgitt, “The lycurgus cup - a roman nanotechnology,” *Gold bulletin*, vol. 40, no. 4, pp. 270–277, 2007.
- [4] M. Reibold, P. Paufler, A. Levin, W. Kochmann, N. Pätzke, and D. Meyer, “Materials: Carbon nanotubes in an ancient damascus sabre,” *Nature*, vol. 444, no. 7117, p. 286, 2006.
- [5] N. Taniguchi, C. Arakawa, and T. Kobayashi, “On the basic concept of ‘nanotechnology’,” in *Proceedings of the International Conference on Production Engineering, 1974-8*, vol. 2, pp. 18–23, , 1974.
- [6] K. E. Drexler, “Engines of creation: the coming era of nanotechnology,” *Anchor Book*, 1986.
- [7] R. P. Feynman, “Theres plenty of room at the bottom: An invitation to enter a new field of physics,” in *Handbook of Nanoscience, Engineering, and Technology, Third Edition*, pp. 26–35, CRC Press, 2012.
- [8] G. Binnig, H. Rohrer, C. Gerber, and E. Weibel, “Tunneling through a controllable vacuum gap,” *Applied Physics Letters*, vol. 40, no. 2, pp. 178–180, 1982.
- [9] G. Binnig, H. Rohrer, C. Gerber, and E. Weibel, “Surface studies by scanning tunneling microscopy,” *Physical Review Letters*, vol. 49, pp. 57–61, Jul 1982.

- [10] D. M. Eigler and E. K. Schweizer, “Positioning single atoms with a scanning tunnelling microscope,” *Nature*, vol. 344, no. 6266, p. 524, 1990.
- [11] Nobelprize.org. Nobel Media AB 2014, “The nobel prize in physics 1986..” [http://www.nobelprize.org/nobel\\_prizes/physics/laureates/1986/](http://www.nobelprize.org/nobel_prizes/physics/laureates/1986/). (last accessed 2018-10-12).
- [12] IBM, 2012, “A boy and his atom: The world’s smallest movie.” <http://www.research.ibm.com/articles/madewithatoms.shtml>. (last accessed 2018-10-12).
- [13] A. K. Yetisen, A. F. Coskun, G. England, S. Cho, H. Butt, J. Hurwitz, M. Kolle, A. Khademhosseini, A. J. Hart, A. Folch, *et al.*, “Art on the nanoscale and beyond,” *Advanced Materials*, vol. 28, no. 9, pp. 1724–1742, 2016.
- [14] N. C. Seeman, “Nucleic-acid junctions and lattices,” *Journal of Theoretical Biology*, vol. 99, no. 2, pp. 237–247, 1982.
- [15] V. Bloomfield, D. Crothers, and I. Tinoco, *Nucleic Acids: Structure, Properties, and Functions*. University Science Books, 2000.
- [16] M. Campbell, S. Farrell, and O. McDougal, *Biochemistry*. Cengage Learning, 2016.
- [17] R. Dahm, “Friedrich miescher and the discovery of dna,” *Developmental biology*, vol. 278, no. 2, pp. 274–288, 2005.
- [18] O. T. Avery, C. M. Macleod, and M. McCarty, “Studies on the chemical nature of the substance inducing transformation of pneumococcal types. inductions of transformation by a desoxyribonucleic acid fraction isolated from pneumococcus type iii.” *Journal of Experimental Medicine*, vol. 149, no. 2, pp. 297–326, 1979.
- [19] A. D. Hershey and M. Chase, “Independent functions of viral protein and nucleic acid in growth of bacteriophage,” *The Journal of general physiology*, vol. 36, no. 1, pp. 39–56, 1952.
- [20] R. E. Franklin and R. G. Gosling, “Molecular configuration in sodium thymonucleate,” *Nature*, vol. 171, no. 4356, pp. 740–741, 1953.
- [21] M. H. F. Wilkins, A. R. Stokes, and H. R. Wilson, “Molecular structure of nucleic acids: molecular structure of deoxypentose nucleic acids,” *Nature*, vol. 171, no. 4356, p. 738, 1953.

- [22] E. Chargaff, "Chemical specificity of nucleic acids and mechanism of their enzymatic degradation," *Experientia*, vol. 6, no. 6, pp. 201–209, 1950.
- [23] J. D. Watson and F. H. C. Crick, "Molecular structure of nucleic acids - a structure for deoxyribose nucleic acid," *Nature*, vol. 171, no. 4356, pp. 737–738, 1953.
- [24] Nobelprize.org. Nobel Media AB 2014, "The nobel prize in physiology or medicine 1962." [https://www.nobelprize.org/nobel\\_prizes/medicine/laureates/1962/](https://www.nobelprize.org/nobel_prizes/medicine/laureates/1962/). (last accessed 2018-10-12).
- [25] M. Meselson and F. W. Stahl, "The replication of dna in escherichia coli," *Proceedings of the National Academy of Sciences*, vol. 44, no. 7, pp. 671–682, 1958.
- [26] G. Milman, R. Langridge, and M. J. Chamberlin, "The structure of a dna-rna hybrid," *Proceedings of the National Academy of Sciences*, vol. 57, no. 6, pp. 1804–1810, 1967.
- [27] A. Rich, A. Nordheim, and A. H.-J. Wang, "The chemistry and biology of left-handed z-dna," *Annual Review of Biochemistry*, vol. 53, no. 1, pp. 791–846, 1984.
- [28] F. M. Pohl and T. M. Jovin, "Salt-induced co-operative conformational change of a synthetic dna: equilibrium and kinetic studies with poly (dg-dc)," *Journal of molecular biology*, vol. 67, no. 3, pp. 375–396, 1972.
- [29] C. Mao, W. Sun, Z. Shen, and N. C. Seeman, "A nanomechanical device based on the b-z transition of dna," *Nature*, vol. 397, no. 6715, p. 144, 1999.
- [30] P. Yakovchuk, E. Protozanova, and M. D. Frank-Kamenetskii, "Base-stacking and base-pairing contributions into thermal stability of the dna double helix," *Nucleic Acids Research*, vol. 34, no. 2, pp. 564–574, 2006.
- [31] J. Lipfert, S. Doniach, R. Das, and D. Herschlag, "Understanding nucleic acid-ion interactions," *Annual Review of Biochemistry*, vol. 83, pp. 813–841, 2014.
- [32] P. W. K. Rothmund, "Folding dna to create nanoscale shapes and patterns," *Nature*, vol. 440, no. 7082, pp. 297–302, 2006.
- [33] J. Marmur and P. Doty, "Determination of the base composition of deoxyribonucleic acid from its thermal denaturation temperature," *Journal of molecular biology*, vol. 5, no. 1, pp. 109–118, 1962.

- [34] K. J. Breslauer, R. Frank, H. Blöcker, and L. A. Marky, “Predicting dna duplex stability from the base sequence,” *Proceedings of the National Academy of Sciences*, vol. 83, no. 11, pp. 3746–3750, 1986.
- [35] Sigma Aldrich, “Oligonucleotide melting temperature.” <https://www.sigmaaldrich.com/technical-documents/articles/biology/oligos-melting-temp.html>. (last accessed 2018-10-12).
- [36] J. SantaLucia, “A unified view of polymer, dumbbell, and oligonucleotide dna nearest-neighbor thermodynamics,” *Proceedings of the National Academy of Sciences*, vol. 95, no. 4, pp. 1460–1465, 1998.
- [37] C. Schildkraut and S. Lifson, “Dependence of the melting temperature of dna on salt concentration,” *Biopolymers: Original Research on Biomolecules*, vol. 3, no. 2, pp. 195–208, 1965.
- [38] J. SantaLucia Jr and D. Hicks, “The thermodynamics of dna structural motifs,” *Annual Review of Biophysics and Biomolecular Structure*, vol. 33, pp. 415–440, 2004.
- [39] M. Rubinstein and R. H. Colby, *Polymer Physics*. Oxford: Oxford University Press, 2003.
- [40] R. Phillips, J. Kondev, J. Theriot, and H. Garcia, *Physical biology of the cell*. Garland Science, 2012.
- [41] N. C. Seeman, “Nanomaterials based on dna,” *Annual Review of Biochemistry*, vol. 79, pp. 65–87, 2010. (cit. on p. 66).
- [42] N. C. Seeman, “Dna in a material world,” *Nature*, vol. 421, no. 6921, pp. 427–431, 2003.
- [43] X. Li, X. Yang, J. Qi, and N. C. Seeman, “Antiparallel dna double crossover molecules as components for nanoconstruction,” *Journal of the American Chemical Society*, vol. 118, no. 26, pp. 6131–6140, 1996.
- [44] E. Winfree, F. Liu, L. A. Wenzler, and N. C. Seeman, “Design and self-assembly of two-dimensional dna crystals,” *Nature*, vol. 394, no. 6693, p. 539, 1998.

- [45] D. Liu, M. Wang, Z. Deng, R. Walulu, and C. Mao, "Tensegrity: construction of rigid dna triangles with flexible four-arm dna junctions," *Journal of the American Chemical Society*, vol. 126, no. 8, pp. 2324–2325, 2004.
- [46] J. P. Zheng, J. J. Birktoft, Y. Chen, T. Wang, R. J. Sha, P. E. Constantinou, S. L. Ginell, C. D. Mao, and N. C. Seeman, "From molecular to macroscopic via the rational design of a self-assembled 3d dna crystal," *Nature*, vol. 461, no. 7260, pp. 74–77, 2009.
- [47] J. Chen and N. C. Seeman, "Synthesis from dna of a molecule with the connectivity of a cube," *Nature*, vol. 350, no. 6319, p. 631, 1991.
- [48] B. Yurke, A. J. Turberfield, A. P. Mills Jr, F. C. Simmel, and J. L. Neumann, "A dna-fuelled molecular machine made of dna," *Nature*, vol. 406, no. 6796, p. 605, 2000.
- [49] T. Gerling, K. F. Wagenbauer, A. M. Neuner, and H. Dietz, "Dynamic dna devices and assemblies formed by shape-complementary, non-base pairing 3d components," *Science*, vol. 347, no. 6229, pp. 1446–1452, 2015.
- [50] J.-S. Shin and N. A. Pierce, "A synthetic dna walker for molecular transport," *Journal of the American Chemical Society*, vol. 126, no. 35, pp. 10834–10835, 2004.
- [51] E. Kopperger, J. List, S. Madhira, F. Rothfischer, D. C. Lamb, and F. C. Simmel, "A self-assembled nanoscale robotic arm controlled by electric fields," *Science*, vol. 359, no. 6373, pp. 296–301, 2018.
- [52] I. H. Stein, V. Schuller, P. Bohm, P. Tinnefeld, and T. Liedl, "Single-molecule fret ruler based on rigid dna origami blocks," *ChemPhysChem*, vol. 12, no. 3, pp. 689–695, 2011.
- [53] H. Yan, S. H. Park, G. Finkelstein, J. H. Reif, and T. H. LaBean, "Dna-templated self-assembly of protein arrays and highly conductive nanowires," *Science*, vol. 301, no. 5641, pp. 1882–1884, 2003.
- [54] H. Y. Li, S. H. Park, J. H. Reif, T. H. LaBean, and H. Yan, "Dna-templated self-assembly of protein and nanoparticle linear arrays," *Journal of the American Chemical Society*, vol. 126, no. 2, pp. 418–419, 2004.

- [55] B. Ding, Z. Deng, H. Yan, S. Cabrini, R. N. Zuckermann, and J. Bokor, “Gold nanoparticle self-similar chain structure organized by dna origami,” *Journal of the American Chemical Society*, vol. 132, no. 10, pp. 3248–3249, 2010.
- [56] S. Pal, Z. T. Deng, B. Q. Ding, H. Yan, and Y. Liu, “Dna-origami-directed self-assembly of discrete silver-nanoparticle architectures,” *Angewandte Chemie International Edition*, vol. 49, no. 15, pp. 2700–2704, 2010.
- [57] T. Zhang, A. Neumann, J. Lindlau, Y. Z. Wu, G. Prarnanik, B. Naydenov, F. Jelezko, F. Schuder, S. Huber, M. Huber, F. Stehr, A. Hogege, T. Weil, and T. Liedl, “Dna-based self-assembly of fluorescent nanodiamonds,” *Journal of the American Chemical Society*, vol. 137, no. 31, pp. 9776–9779, 2015.
- [58] F. Nicoli, A. Barth, W. Bae, F. Neukirchinger, A. H. Crevenna, D. C. Lamb, and T. Liedl, “Directional photonic wire mediated by homo-forster resonance energy transfer on a dna origami platform,” *ACS Nano*, vol. 11, no. 11, pp. 11264–11272, 2017.
- [59] M. Langecker, V. Arnaut, T. G. Martin, J. List, S. Renner, M. Mayer, H. Dietz, and F. C. Simmel, “Synthetic lipid membrane channels formed by designed dna nanostructures,” *Science*, vol. 338, no. 6109, pp. 932–936, 2012.
- [60] A. Kuzyk, R. Jungmann, G. P. Acuna, and N. Liu, “Dna origami route for nanophotonics,” *ACS Photonics*, vol. 5, no. 4, pp. 1151–1163, 2018.
- [61] F. Hong, F. Zhang, Y. Liu, and H. Yan, “Dna origami: scaffolds for creating higher order structures,” *Chemical reviews*, vol. 117, no. 20, pp. 12584–12640, 2017.
- [62] S. M. Douglas, H. Dietz, T. Liedl, B. Hogberg, F. Graf, and W. M. Shih, “Self-assembly of dna into nanoscale three-dimensional shapes,” *Nature*, vol. 459, no. 7245, pp. 414–418, 2009.
- [63] Y. G. Ke, S. M. Douglas, M. H. Liu, J. Sharma, A. C. Cheng, A. Leung, Y. Liu, W. M. Shih, and H. Yan, “Multilayer dna origami packed on a square lattice,” *Journal of the American Chemical Society*, vol. 131, no. 43, pp. 15903–15908, 2009.
- [64] D. Han, S. Pal, J. Nangreave, Z. Deng, Y. Liu, and H. Yan, “Dna origami with complex curvatures in three-dimensional space,” *Science*, vol. 332, no. 6027, pp. 342–346, 2011.

- [65] H. Dietz, S. M. Douglas, and W. M. Shih, “Folding dna into twisted and curved nanoscale shapes,” *Science*, vol. 325, no. 5941, pp. 725–730, 2009.
- [66] S. M. Douglas, A. H. Marblestone, S. Teerapittayanon, A. Vazquez, G. M. Church, and W. M. Shih, “Rapid prototyping of 3d dna-origami shapes with cadnano,” *Nucleic Acids Research*, vol. 37, no. 15, pp. 5001–5006, 2009.
- [67] D. N. Kim, F. Kilchherr, H. Dietz, and M. Bathe, “Quantitative prediction of 3d solution shape and flexibility of nucleic acid nanostructures,” *Nucleic Acids Research*, vol. 40, no. 7, pp. 2862–2868, 2012.
- [68] C. E. Castro, F. Kilchherr, D. N. Kim, E. L. Shiao, T. Wauer, P. Wortmann, M. Bathe, and H. Dietz, “A primer to scaffolded dna origami,” *Nature Methods*, vol. 8, no. 3, pp. 221–229, 2011.
- [69] R. Martin, *Gel Electrophoresis: Nucleic Acids*. Introduction to biotechniques series, BIOS Scientific, 1996.
- [70] D. Williams and C. Carter, *Transmission Electron Microscopy: A Textbook for Materials Science*. No. 2 in Cambridge library collection, Springer, 2009.
- [71] A. Baró and R. Reifengerger, *Atomic Force Microscopy in Liquid: Biological Applications*. Wiley, 2012.
- [72] G. Caldwell, S. Williams, and K. Caldwell, *Integrated Genomics: A Discovery-Based Laboratory Course*. Wiley, 2006.
- [73] H. Schnablegger and Y. Singh, *The SAXS Guide, Getting Acquainted with the Principles*. Anton Paar GmbH, Austria, 4 ed., 2017.
- [74] J. Als-Nielsen and D. McMorrow, *Elements of modern X-ray physics*. John Wiley & Sons, Ltd, 2 ed., 2011.
- [75] L. Feigin and D. Svergun, *Structure Analysis by Small-Angle X-Ray and Neutron Scattering*. Springer US, 2013.
- [76] D. I. Svergun and M. H. J. Koch, “Small-angle scattering studies of biological macromolecules in solution,” *Reports on Progress in Physics*, vol. 66, no. 10, pp. 1735–1782, 2003.

- [77] C. D. Putnam, M. Hammel, G. L. Hura, and J. A. Tainer, “X-ray solution scattering (saxs) combined with crystallography and computation: defining accurate macromolecular structures, conformations and assemblies in solution,” *Quarterly Reviews of Biophysics*, vol. 40, no. 3, pp. 191–285, 2007.
- [78] N. Allec, M. Choi, N. Yesupriya, B. Szychowski, M. R. White, M. G. Kann, E. D. Garcin, M.-C. Daniel, and A. Badano, “Small-angle x-ray scattering method to characterize molecular interactions: Proof of concept,” *Scientific reports*, vol. 5, no. 12085, 2015.
- [79] E. S. Andersen, M. Dong, M. M. Nielsen, K. Jahn, R. Subramani, W. Mamdouh, M. M. Golas, B. Sander, H. Stark, C. L. P. Oliveira, J. S. Pedersen, V. Birkedal, F. Besenbacher, K. V. Gothelf, and J. Kjems, “Self-assembly of a nanoscale dna box with a controllable lid,” *Nature*, vol. 459, no. 7243, pp. 73–76, 2009.
- [80] A. J. Mastroianni, D. A. Sivak, P. L. Geissler, and A. P. Alivisatos, “Probing the conformational distributions of subpersistence length dna,” *Biophysical Journal*, vol. 97, no. 5, pp. 1408–1417, 2009.
- [81] S. Y. Park, A. K. R. Lytton-Jean, B. Lee, S. Weigand, G. C. Schatz, and C. A. Mirkin, “Dna-programmable nanoparticle crystallization,” *Nature*, vol. 451, no. 7178, pp. 553–556, 2008.
- [82] D. Nykypanchuk, M. M. Maye, D. van der Lelie, and O. Gang, “Dna-guided crystallization of colloidal nanoparticles,” *Nature*, vol. 451, no. 7178, pp. 549–552, 2008.
- [83] O. Glatter and O. Kratky, *Small angle X-ray scattering*. London ; New York: Academic Press, 1982.
- [84] D. I. Svergun, L. A. Feigin, and G. W. Taylor, *Structure analysis by small-angle x-ray and neutron scattering*. New York: Plenum Press, 1987.
- [85] J. S. Pedersen, “Analysis of small-angle scattering data from colloids and polymer solutions: modeling and least-squares fitting,” *Advances in colloid and interface science*, vol. 70, pp. 171–210, 1997.
- [86] The SasView Project, “Sasview documentation.” <http://www.sasview.org/docs/user/user.html>. (last accessed 2018-07-19).

- [87] G. Fournet and A. Guinier, *Small angle scattering of X-rays*. John Wiley and Sons, New York, 1955.
- [88] P. Mittelbach and G. Porod, “Small-angle x-ray scattering by dilute colloid systems. the calculation of scattering-curves for parallelepipeds,” *Acta Physica Austriaca*, vol. 14, p. 185211, 1961.
- [89] R. Nayuk and K. Huber, “Formfactors of hollow and massive rectangular parallelepipeds at variable degree of anisometry,” *Zeitschrift für Physikalische Chemie*, vol. 226, no. 7-8, pp. 837–854, 2012.
- [90] K. G. Yager, Y. G. Zhang, F. Lu, and O. Gang, “Periodic lattices of arbitrary nano-objects: modeling and applications for self-assembled systems,” *Journal of Applied Crystallography*, vol. 47, pp. 118–129, 2014.
- [91] B. R. Pauw, “Everything saxs: small-angle scattering pattern collection and correction,” *Journal of Physics: Condensed Matter*, vol. 25, no. 38, p. 383201, 2013.
- [92] L. K. Bruetzel, S. Fischer, A. Salditt, S. M. Sedlak, B. Nickel, and J. Lipfert, “A mo-anode-based in-house source for small-angle x-ray scattering measurements of biological macromolecules,” *Review of Scientific Instruments*, vol. 87, no. 2, p. 025103, 2016.
- [93] S. Fischer, *Small-angle X-ray scattering of nanomaterials*. PhD thesis, Ludwig-Maximilians-Universität München, 2017.
- [94] H. Amenitsch, S. Bernstorff, and P. Laggner, “High-flux beamline for small-angle x-ray scattering at elettra,” *Review of Scientific Instruments*, vol. 66, no. 2, pp. 1624–1626, 1995.
- [95] P. Van Vaerenbergh, J. Lonardon, M. Sztucki, P. Boesecke, J. Gorini, L. Claustre, F. Sever, J. Morse, and T. Narayanan, “An upgrade beamline for combined wide, small and ultra small-angle x-ray scattering at the esrf,” *AIP Conference Proceedings*, vol. 1741, no. 1, p. 030034, 2016.
- [96] J. Ilavsky, “Nika - software for 2d data reduction,” *Journal of Applied Crystallography*, vol. 45, pp. 324–328, 2012.
- [97] O. Glatter, “A new method for the evaluation of small-angle scattering data,” *Journal of Applied Crystallography*, vol. 10, no. 5, pp. 415–421, 1977.

- [98] O. Glatter, “Computation of distance distribution-functions and scattering functions of models for small-angle scattering experiments,” *Acta Physica Austriaca*, vol. 52, no. 3-4, pp. 243–256, 1980.
- [99] A. Semenyuk and D. Svergun, “Gnom—a program package for small-angle scattering data processing,” *Journal of Applied Crystallography*, vol. 24, no. 5, pp. 537–540, 1991.
- [100] D. Svergun, “Determination of the regularization parameter in indirect-transform methods using perceptual criteria,” *Journal of applied crystallography*, vol. 25, no. 4, pp. 495–503, 1992.
- [101] A. Bergmann, G. Fritz, and O. Glatter, “Solving the generalized indirect fourier transformation (gift) by boltzmann simplex simulated annealing (bssa),” *Journal of Applied Crystallography*, vol. 33, pp. 1212–1216, 2000.
- [102] SasView, “Sasview for small angle scattering analysis - sas community project launched from the nsf danse effort.” <http://www.sasview.org>. (last accessed 2018-07-19).
- [103] D. Franke, M. Petoukhov, P. Konarev, A. Panjkovich, A. Tuukkanen, H. Mertens, A. Kikhney, N. Hajizadeh, J. Franklin, C. Jeffries, *et al.*, “Atsas 2.8: a comprehensive data analysis suite for small-angle scattering from macromolecular solutions,” *Journal of applied crystallography*, vol. 50, no. 4, pp. 1212–1225, 2017.
- [104] D. Svergun, C. Barberato, and M. H. J. Koch, “Crysol - a program to evaluate x-ray solution scattering of biological macromolecules from atomic coordinates,” *Journal of Applied Crystallography*, vol. 28, pp. 768–773, 1995.
- [105] S. Fischer, C. Hartl, K. Frank, J. O. Radler, T. Liedl, and B. Nickel, “Shape and interhelical spacing of dna origami nanostructures studied by small-angle x-ray scattering,” *Nano Letters*, vol. 16, no. 7, pp. 4282–4287, 2016. <https://doi.org/10.1021/acs.nanolett.6b01335>.
- [106] T. G. Martin and H. Dietz, “Magnesium-free self-assembly of multi-layer dna objects,” *Nature Communications*, vol. 3, no. 1103, 2012. doi: 10.1038/ncomms2095.
- [107] Y. Ke, G. Bellot, N. V. Voigt, E. Fradkov, and W. M. Shih, “Two design strategies for enhancement of multilayer–dna-origami folding: underwinding for specific

- intercalator rescue and staple-break positioning,” *Chemical science*, vol. 3, no. 8, pp. 2587–2597, 2012.
- [108] C. L. P. Oliveira, S. Juul, H. L. Jrgensen, B. Knudsen, D. Tordrup, F. Oteri, M. Falconi, J. Koch, A. Desideri, J. S. Pedersen, F. F. Andersen, and B. R. Knudsen, “Structure of nanoscale truncated octahedral dna cages: Variation of single-stranded linker regions and influence on assembly yields,” *ACS Nano*, vol. 4, no. 3, pp. 1367–1376, 2010.
- [109] J. Yoo and A. Aksimentiev, “In situ structure and dynamics of dna origami determined through molecular dynamics simulations,” *Proceedings of the National Academy of Sciences*, vol. 110, no. 50, pp. 20099–20104, 2013.
- [110] A. Kuzyk, R. Schreiber, Z. Y. Fan, G. Pardatscher, E. M. Roller, A. Hogele, F. C. Simmel, A. O. Govorov, and T. Liedl, “Dna-based self-assembly of chiral plasmonic nanostructures with tailored optical response,” *Nature*, vol. 483, no. 7389, pp. 311–314, 2012.
- [111] R.-J. Roe, *Methods of X-Ray and Neutron Scattering in Polymer Science*. New York: Oxford University Press, 2000.
- [112] P. Szekely, A. Ginsburg, T. Ben-Nun, and U. Raviv, “Solution x-ray scattering form factors of supramolecular self-assembled structures,” *Langmuir*, vol. 26, no. 16, pp. 13110–13129, 2010.
- [113] J. Yoo, A. N. Sobh, C.-Y. Li, and A. Aksimentiev, “cadnano to pdb file converter.” <https://nanohub.org/resources/cadnanocvrt>, 2015. (accessed April 2016).
- [114] X. C. Bai, T. G. Martin, S. H. W. Scheres, and H. Dietz, “Cryo-em structure of a 3d dna-origami object,” *Proceedings of the National Academy of Sciences*, vol. 109, no. 49, pp. 20012–20017, 2012.
- [115] J. M. Arbona, J.-P. Aimé, and J. Elezgaray, “Modeling the mechanical properties of dna nanostructures,” *Physical Review E*, vol. 86, no. 5, p. 051912, 2012.
- [116] P. J. Chung, M. C. Choi, H. P. Miller, H. E. Feinstein, U. Raviv, Y. Li, L. Wilson, S. C. Feinstein, and C. R. Safinya, “Direct force measurements reveal that protein tau confers short-range attractions and isoform-dependent steric stabilization to

- microtubules,” *Proceedings of the National Academy of Sciences*, vol. 112, no. 47, pp. E6416–E6425, 2015.
- [117] X. Qiu, K. Andresen, L. W. Kwok, J. S. Lamb, H. Y. Park, and L. Pollack, “Inter-dna attraction mediated by divalent counterions,” *Physical review letters*, vol. 99, no. 3, p. 038104, 2007.
- [118] B. Luan and A. Aksimentiev, “Dna attraction in monovalent and divalent electrolytes,” *Journal of the American Chemical Society*, vol. 130, no. 47, pp. 15754–15755, 2008.
- [119] T. L. Sobey, S. Renner, and F. C. Simmel, “Assembly and melting of dna nanotubes from single-sequence tiles,” *Journal of Physics: Condensed Matter*, vol. 21, no. 3, p. 034112, 2008.
- [120] J. P. J. Sobczak, T. G. Martin, T. Gerling, and H. Dietz, “Rapid folding of dna into nanoscale shapes at constant temperature,” *Science*, vol. 338, no. 6113, pp. 1458–1461, 2012.
- [121] L. K. Bruetzel, T. Gerling, S. M. Sedlak, P. U. Walker, W. Zheng, H. Dietz, and J. Lipfert, “Conformational changes and flexibility of dna devices observed by small-angle x-ray scattering,” *Nano Letters*, vol. 16, no. 8, pp. 4871–4879, 2016.
- [122] L. K. Bruetzel, P. U. Walker, T. Gerling, H. Dietz, and J. Lipfert, “Time-resolved small-angle x-ray scattering reveals millisecond transitions of a dna origami switch,” *Nano Letters*, vol. 18, no. 4, pp. 2672–2676, 2018.
- [123] M. A. B. Baker, A. J. Tuckwell, J. F. Berengut, J. Bath, F. Benn, A. P. Duff, A. E. Whitten, K. E. Dunn, R. M. Hynson, A. J. Turberfield, and L. K. Lee, “Dimensions and global twist of single-layer dna origami measured by small-angle x-ray scattering,” *ACS Nano*, vol. 12, no. 6, pp. 5791–5799, 2018. PMID: 29812934.
- [124] C. Hartl, K. Frank, H. Amenitsch, S. Fischer, T. Liedl, and B. Nickel, “Position accuracy of gold nanoparticles on dna origami structures studied with small-angle x-ray scattering,” *Nano Letters*, vol. 18, no. 4, pp. 2609–2615, 2018. <https://doi.org/10.1021/acs.nanolett.8b00412>.

- [125] X. Shi, S. Bonilla, D. Herschlag, and P. Harbury, “Quantifying nucleic acid ensembles with x-ray scattering interferometry,” in *Methods in enzymology*, vol. 558, pp. 75–97, Elsevier, 2015.
- [126] R. S. Mathew-Fenn, R. Das, J. A. Silverman, P. A. Walker, and P. A. Harbury, “A molecular ruler for measuring quantitative distance distributions,” *PLoS One*, vol. 3, no. 10, p. e3229, 2008.
- [127] R. S. Mathew-Fenn, R. Das, and P. A. B. Harbury, “Remeasuring the double helix,” *Science*, vol. 322, no. 5900, pp. 446–449, 2008.
- [128] G. P. Acuna, F. M. Moller, P. Holzmeister, S. Beater, B. Lalkens, and P. Tinnefeld, “Fluorescence enhancement at docking sites of dna-directed self-assembled nanoantennas,” *Science*, vol. 338, no. 6106, pp. 506–510, 2012.
- [129] C. Vietz, B. Lalkens, G. P. Acuna, and P. Tinnefeld, “Functionalizing large nanoparticles for small gaps in dimer nanoantennas,” *New Journal of Physics*, vol. 18, no. 4, p. 045012, 2016.
- [130] A. Puchkova, C. Vietz, E. Pibiri, B. Wünsch, M. Sanz Paz, G. P. Acuna, and P. Tinnefeld, “Dna origami nanoantennas with over 5000-fold fluorescence enhancement and single-molecule detection at 25  $\mu\text{m}$ ,” *Nano Letters*, vol. 15, no. 12, pp. 8354–8359, 2015.
- [131] R. Schreiber, N. Luong, Z. Y. Fan, A. Kuzyk, P. C. Nickels, T. Zhang, D. M. Smith, B. Yurke, W. Kuang, A. O. Govorov, and T. Liedl, “Chiral plasmonic dna nanostructures with switchable circular dichroism,” *Nature communications*, vol. 4, p. 2948, 2013.
- [132] X. Shen, C. Song, J. Wang, D. Shi, Z. Wang, N. Liu, and B. Ding, “Rolling up gold nanoparticle-dressed dna origami into three-dimensional plasmonic chiral nanostructures,” *Journal of the American Chemical Society*, vol. 134, no. 1, pp. 146–149, 2011.
- [133] E.-M. Roller, L. K. Khorashad, M. Fedoruk, R. Schreiber, A. O. Govorov, and T. Liedl, “Dna-assembled nanoparticle rings exhibit electric and magnetic resonances at visible frequencies,” *Nano Letters*, vol. 15, no. 2, pp. 1368–1373, 2015.

- [134] W. P. Klein, C. N. Schmidt, B. Rapp, S. Takabayashi, W. B. Knowlton, J. Lee, B. Yurke, W. L. Hughes, E. Graugnard, and W. Kuang, “Multiscaffold dna origami nanoparticle waveguides,” *Nano Letters*, vol. 13, no. 8, pp. 3850–3856, 2013.
- [135] K. Vogele, J. List, G. Pardatscher, N. B. Holland, F. C. Simmel, and T. Pirzer, “Self-assembled active plasmonic waveguide with a peptide-based thermomechanical switch,” *ACS Nano*, vol. 10, no. 12, pp. 11377–11384, 2016.
- [136] E.-M. Roller, L. V. Besteiro, C. Pupp, L. K. Khorashad, A. O. Govorov, and T. Liedl, “Hotspot-mediated non-dissipative and ultrafast plasmon passage,” *Nature Physics*, vol. 13, no. 8, p. 761, 2017.
- [137] X. Shi, D. Herschlag, and P. A. Harbury, “Structural ensemble and microscopic elasticity of freely diffusing dna by direct measurement of fluctuations,” *Proceedings of the National Academy of Sciences*, vol. 110, no. 16, pp. E1444–E1451, 2013.
- [138] G. L. Hura, C. L. Tsai, S. A. Claridge, M. L. Mendillo, J. M. Smith, G. J. Williams, A. J. Mastrianni, A. P. Alivisatos, C. D. Putnam, R. D. Kolodner, and J. A. Tainer, “Dna conformations in mismatch repair probed in solution by x-ray scattering from gold nanocrystals,” *Proceedings of the National Academy of Sciences*, vol. 110, no. 43, pp. 17308–17313, 2013.
- [139] C. Chi, F. Vargas-Lara, A. V. Tkachenko, F. W. Starr, and O. Gang, “Internal structure of nanoparticle dimers linked by dna,” *ACS Nano*, vol. 6, no. 8, pp. 6793–6802, 2012.
- [140] A. P. Alivisatos, K. P. Johnsson, X. G. Peng, T. E. Wilson, C. J. Loweth, M. P. Bruchez, and P. G. Schultz, “Organization of ‘nanocrystal molecules’ using dna,” *Nature*, vol. 382, no. 6592, pp. 609–611, 1996.
- [141] C. A. Mirkin, R. L. Letsinger, R. C. Mucic, and J. J. Storhoff, “A dna-based method for rationally assembling nanoparticles into macroscopic materials,” *Nature*, vol. 382, no. 6592, pp. 607–609, 1996.
- [142] J. Sharma, R. Chhabra, C. S. Andersen, K. V. Gothelf, H. Yan, and Y. Liu, “Toward reliable gold nanoparticle patterning on self-assembled dna nanoscaffold,” *Journal of the American Chemical Society*, vol. 130, no. 25, pp. 7820–7821, 2008.

- [143] S. J. Hurst, A. K. R. Lytton-Jean, and C. A. Mirkin, “Maximizing dna loading on a range of gold nanoparticle sizes,” *Analytical Chemistry*, vol. 78, no. 24, pp. 8313–8318, 2006.
- [144] H. D. Hill, J. E. Millstone, M. J. Banholzer, and C. A. Mirkin, “The role radius of curvature plays in thiolated oligonucleotide loading on gold nanoparticles,” *ACS Nano*, vol. 3, no. 2, pp. 418–424, 2009.
- [145] S. J. Henderson, “Monte carlo modeling of small-angle scattering data from non-interacting homogeneous and heterogeneous particles in solution,” *Biophysical Journal*, vol. 70, no. 4, pp. 1618–1627, 1996.
- [146] S. Hansen, “Calculation of small-angle scattering profiles using monte-carlo simulation,” *Journal of Applied Crystallography*, vol. 23, pp. 344–346, 1990.
- [147] K. Frank, “Small-angle x-ray scattering analysis of dna origami crystals and bulk lipid phases,” 2017. Masters thesis, Ludwig-Maximilians-Universität München, 2017.
- [148] P. J. Flory, *Principles of Polymer Chemistry*. Ithaca, New York: Cornell University Press, Ithaca, NY, 1953.
- [149] W. J. Parak, T. Pellegrino, C. M. Micheel, D. Gerion, S. C. Williams, and A. P. Alivisatos, “Conformation of oligonucleotides attached to gold nanocrystals probed by gel electrophoresis,” *Nano Letters*, vol. 3, no. 1, pp. 33–36, 2003.
- [150] J. B. Falabella, T. J. Cho, D. C. Ripple, V. A. Hackley, and M. J. Tarlov, “Characterization of gold nanoparticles modified with single-stranded dna using analytical ultracentrifugation and dynamic light scattering,” *Langmuir*, vol. 26, no. 15, pp. 12740–12747, 2010.
- [151] B. C. McAlister and B. P. Grady, “Simulation of small-angle x-ray scattering from single-particle systems,” *Journal of Applied Crystallography*, vol. 31, pp. 594–599, 1998.
- [152] M. V. Petoukhov, P. V. Konarev, A. G. Kikhney, and D. I. Svergun, “Atsas 2.1—towards automated and web-supported small-angle scattering data analysis,” *Journal of applied crystallography*, vol. 40, pp. s223–s228, 2007.

- [153] T. Zhang, C. Hartl, K. Frank, A. Heuer-Jungemann, S. Fischer, P. C. Nickels, B. Nickel, and T. Liedl, “3d dna origami crystals,” *Advanced Materials*, p. 1800273, 2017. <https://doi.org/10.1002/adma.201800273>.
- [154] R. J. Macfarlane, B. Lee, M. R. Jones, N. Harris, G. C. Schatz, and C. A. Mirkin, “Nanoparticle superlattice engineering with dna,” *Science*, vol. 334, no. 6053, pp. 204–208, 2011.
- [155] M. R. Jones, N. C. Seeman, and C. A. Mirkin, “Programmable materials and the nature of the dna bond,” *Science*, vol. 347, no. 6224, p. 1260901, 2015.
- [156] B. Nickel and T. Liedl, “Dna-linked superlattices get into shape,” *Nature Materials*, vol. 14, no. 8, p. 746, 2015.
- [157] D. J. Park, C. Zhang, J. C. Ku, Y. Zhou, G. C. Schatz, and C. A. Mirkin, “Plasmonic photonic crystals realized through dna-programmable assembly,” *Proceedings of the National Academy of Sciences*, vol. 112, no. 4, pp. 977–981, 2015.
- [158] J. D. Brodin, E. Auyeung, and C. A. Mirkin, “Dna-mediated engineering of multicomponent enzyme crystals,” *Proceedings of the National Academy of Sciences*, vol. 112, no. 15, pp. 4564–4569, 2015.
- [159] J. W. Zheng, P. E. Constantinou, C. Micheel, A. P. Alivisatos, R. A. Kiehl, and N. C. Seeman, “Two-dimensional nanoparticle arrays show the organizational power of robust dna motifs,” *Nano Letters*, vol. 6, no. 7, pp. 1502–1504, 2006.
- [160] E. Auyeung, T. I. N. G. Li, A. J. Senesi, A. L. Schmucker, B. C. Pals, M. O. de la Cruz, and C. A. Mirkin, “Dna-mediated nanoparticle crystallization into wulff polyhedra,” *Nature*, vol. 505, no. 7481, pp. 73–77, 2014.
- [161] Y. Tian, T. Wang, W. Y. Liu, H. L. Xin, H. L. Li, Y. G. Ke, W. M. Shih, and O. Gang, “Prescribed nanoparticle cluster architectures and low-dimensional arrays built using octahedral dna origami frames,” *Nature Nanotechnology*, vol. 10, no. 7, pp. 637–644, 2015.
- [162] Y. Tian, Y. G. Zhang, T. Wang, H. L. L. Xin, H. L. Li, and O. Gang, “Lattice engineering through nanoparticle-dna frameworks,” *Nature Materials*, vol. 15, no. 6, p. 654, 2016.

- [163] W. Y. Liu, M. Tagawa, H. L. L. Xin, T. Wang, H. Emamy, H. L. Li, K. G. Yager, F. W. Starr, A. V. Tkachenko, and O. Gang, “Diamond family of nanoparticle superlattices,” *Science*, vol. 351, no. 6273, pp. 582–586, 2016.
- [164] Y. Ke, L. L. Ong, W. Sun, J. Song, M. Dong, W. M. Shih, and P. Yin, “Dna brick crystals with prescribed depths,” *Nature chemistry*, vol. 6, no. 11, p. 994, 2014.
- [165] Y. Zhang, S. Pal, B. Srinivasan, T. Vo, S. Kumar, and O. Gang, “Selective transformations between nanoparticle superlattices via the reprogramming of dna-mediated interactions,” *Nature Materials*, vol. 14, no. 8, p. 840, 2015.
- [166] W. Liu, H. Zhong, R. Wang, and N. C. Seeman, “Crystalline two-dimensional dna-origami arrays,” *Angewandte Chemie International Edition*, vol. 50, no. 1, pp. 264–267, 2011.
- [167] S. Kocabey, S. Kempter, J. List, Y. Xing, W. Bae, D. Schiffels, W. M. Shih, F. C. Simmel, and T. Liedl, “Membrane-assisted growth of dna origami nanostructure arrays,” *ACS Nano*, vol. 9, no. 4, pp. 3530–3539, 2015.
- [168] B. Ding and N. C. Seeman, “Operation of a dna robot arm inserted into a 2d dna crystalline substrate,” *Science*, vol. 314, no. 5805, pp. 1583–1585, 2006.
- [169] Y. Hao, M. Kristiansen, R. Sha, J. J. Birktoft, C. Hernandez, C. Mao, and N. C. Seeman, “A device that operates within a self-assembled 3d dna crystal,” *Nature chemistry*, vol. 9, no. 8, p. 824, 2017.
- [170] R. Schreiber, J. Do, E. M. Roller, T. Zhang, V. J. Schuller, P. C. Nickels, J. Feldmann, and T. Liedl, “Hierarchical assembly of metal nanoparticles, quantum dots and organic dyes using dna origami scaffolds,” *Nature Nanotechnology*, vol. 9, no. 1, pp. 74–78, 2014.
- [171] P. C. Nickels, Y. Ke, R. Jungmann, D. M. Smith, M. Leichsenring, W. M. Shih, T. Liedl, and B. Högberg, “Dna origami structures directly assembled from intact bacteriophages,” *Small*, vol. 10, no. 9, pp. 1765–1769, 2014.
- [172] A. N. Marchi, I. Saaem, B. N. Vogen, S. Brown, and T. H. LaBean, “Toward larger dna origami,” *Nano Letters*, vol. 14, no. 10, pp. 5740–5747, 2014.

- [173] L. L. Ong, N. Hanikel, O. K. Yaghi, C. Grun, M. T. Strauss, P. Bron, J. Lai-Kee-Him, F. Schueder, B. Wang, P. Wang, *et al.*, “Programmable self-assembly of three-dimensional nanostructures from 10,000 unique components,” *Nature*, vol. 552, no. 7683, p. 72, 2017.
- [174] E. Stahl, T. G. Martin, F. Praetorius, and H. Dietz, “Facile and scalable preparation of pure and dense dna origami solutions,” *Angewandte Chemie International Edition*, vol. 53, no. 47, pp. 12735–12740, 2014.
- [175] E. C. Cho, J. W. Xie, P. A. Wurm, and Y. N. Xia, “Understanding the role of surface charges in cellular adsorption versus internalization by selectively removing gold nanoparticles on the cell surface with a i-2/ki etchant,” *Nano Letters*, vol. 9, no. 3, pp. 1080–1084, 2009.
- [176] C. A. Schneider, W. S. Rasband, and K. W. Eliceiri, “Nih image to imagej: 25 years of image analysis,” *Nature Methods*, vol. 9, no. 7, pp. 671–675, 2012.
- [177] G. Fritz-Popovski, A. Bergmann, and O. Glatter, “Real space functions from experimental small angle scattering data,” *Physical Chemistry Chemical Physics*, vol. 13, no. 13, pp. 5872–5880, 2011.
- [178] H. Kaya, “Scattering behaviour of janus particles,” *Applied Physics a-Materials Science & Processing*, vol. 74, pp. S507–S509, 2002.
- [179] S. M. Douglas, J. J. Chou, and W. M. Shih, “Dna-nanotube-induced alignment of membrane proteins for nmr structure determination,” *Proceedings of the National Academy of Sciences*, vol. 104, no. 16, pp. 6644–6648, 2007.

# List of publications

List of publications that are part of this thesis:

- Stefan Fischer\*, **Caroline Hartl**\*, Kilian Frank, Joachim O. Radler, Tim Liedl, and Bert Nickel. *Shape and Interhelical Spacing of DNA Origami Nanostructures Studied by Small-Angle X-ray Scattering*, Nano Letters, vol. 16, no. 7, pp. 42824287, 2016. doi: 10.1021/acs.nanolett.6b01335 (\*equal contribution)
- **Caroline Hartl**, Kilian Frank, Heinz Amenitsch, Stefan Fischer, Tim Liedl, Bert Nickel, "Position Accuracy of Gold Nanoparticles on DNA Origami Structures Studied with Small-angle X-ray Scattering", Nano Letters, vol. 18, no. 4, pp. 26092615, 2018. doi: 10.1021/acs.nanolett.8b00412
- Tao Zhang, **Caroline Hartl**, Kilian Frank, Amelie Heuer-Jungemann, Stefan Fischer, Philipp C. Nickels, Bert Nickel, and Tim Liedl, "3D DNA Origami Crystals", Advanced Materials, p. 1800273, 2017. doi: 10.1002/adma.201800273



# Acknowledgements

- I thank my supervisor Tim Liedl for giving me the opportunity to enjoy the great atmosphere of freedom and team spirit in his group as one of his PhD students. Thank you for your advice and trust. I really enjoyed working in your group!
- I thank Bert Nickel for his support and for valuable discussions.
- I thank my project partners Tao Zhang, Kilian Frank and Stefan Fischer for the fruitful collaboration.
- A big thank you to our TA Susanne Kempter and to Eva-Maria Roller for the introduction to DNA nanotechnology. A special thank you also to Francesca Nicoli and Nils Gustaffson for proofreading the thesis.
- Thank you to the past and present members of the Liedl Group: Alex Maier, Amelie H.-Jungemann, Andrea Cooke, Arthur Ermatov, Claudia Pupp, Eva-Maria Roller, Francesca Nicoli, Iain Mac Pherson, Kevin Martens, Luisa Kneer, Linh Nguyen, Luzia Kilwing, Mandy Häusler, Marina Polo, Mauricio Pilo-Pais, Nils Gustafsson, Omar Saleh, Philipp Nickels, Robert Schreiber, Samet Kocabey, Stephanie Simmel, Susanne Kempter, Tao Zhang, Timon Funck, Valeria Cotta, Wooli Bae, Yongzheng Xing. Thank you also to Prof. Dr. Joachim Rädler and all members of the Rädler chair!
- Ein besonderer Dank geht auch an meine liebe Familie und meine lieben Freunde!

Thank you all very much!